Athens Journal of Sciences

Quarterly Academic Periodical, Volume 8, Issue 4, December 2021
URL: https://www.athensjournals.gr/ajs
Email: journals@atiner.gr
e-ISSN: 2241-8466 DOI: 10.30958/ajs

Athens Journal of Sciences

Published by the Athens Institute for Education and Research (ATINER)

****

ATINER is an Athens-based World Association of Academics and Researchers based in Athens. ATINER is an independent and non-profit Association with a Mission to become a forum where Academics and Researchers from all over the world can meet in Athens, exchange ideas on their research and discuss future developments in their disciplines, as well as engage with professionals from other fields. Athens was chosen because of its long history of academic gatherings, which go back thousands of years to Plato's Academy and Aristotle's Lyceum. Both these historic places are within walking distance from ATINER's downtown offices. Since antiquity, Athens was an open city. In the words of Pericles, Athens"…is open to the world, we never expel a foreigner from learning or seeing". ("Pericles' Funeral Oration", in Thucydides, The History of the Peloponnesian War). It is ATINER's mission to revive the glory of Ancient Athens by inviting the World Academic Community to the city, to learn from each other in an environment of freedom and respect for other people's opinions and beliefs. After all, the free expression of one's opinion formed the basis for the development of democracy, and Athens was its cradle. As it turned out, the Golden Age of Athens was in fact, the Golden Age of the Western Civilization. Education and (Re)searching for the 'truth' are the pillars of any free (democratic) society. This is the reason why Education and Research are the two core words in ATINER's name.

****

The ***Athens Journal of Sciences (AJS)*** is an Open Access quarterly double-blind peer reviewed journal and considers papers from all areas of Natural & Formal Sciences, including papers on agriculture, computer science, environmental science, materials science, transportation science, chemistry, physics, mathematics and statistics, biology, geography, and earth science (geology, oceanography, astronomy, meteorology). Many of the papers published in this journal have been presented at the various conferences sponsored by the Natural & Formal Sciences Division of the Athens Institute for Education and Research (ATINER). All papers are subject to ATINER's Publication Ethical Policy and Statement.

The Athens Journal of Sciences
ISSN NUMBER: 2241-8466- DOI: 10.30958/ajs
Volume 8, Issue 4, December 2021

Athens Journal of Sciences
Editorial and Reviewers' Board

Editors

- **Dr. Christopher Janetopoulos**, Head, Biology Unit, ATINER & Associate Professor, University of the Sciences, USA.(Biology)
- **Dr. Ethel Petrou**, Academic Member, ATINER & Professor and Chair, Department of Physics, Erie Community College-South, State University of New York, USA.
- **Dr. Ellene Tratras Contis**, Head, Chemistry Unit, ATINER & Professor of Chemistry, Eastern Michigan University, USA.(Chemistry)

Editorial Board

- Dr. Colin Scanes, Academic Member, ATINER & Emeritus Professor, University of Wisconsin Milwaukee, USA.
- Dr. Dimitris Argyropoulos, Professor, North Carolina State University, USA.
- Dr. Cecil Stushnoff, Emeritus Professor, Colorado State University, USA.
- Dr. Hikmat Said Hasan Hilal, Academic Member, ATINER & Professor, Department of Chemistry, An-Najah N. University, Palestine.
- Dr. Jean Paris, Professor, Polytechnique Montreal, Canada.
- Dr. Shiro Kobayashi, Academic Member, ATINER & Distinguished Professor, Kyoto Institute of Technology, Kyoto University, Japan.
- Dr. Jose R. Peralta-Videa, Academic Member, ATINER & Research Specialist and Adjunct Professor, Department of Chemistry, The University of Texas at El Paso, USA.
- Dr. Jean-Pierre Bazureau, Academic Member, ATINER & Professor, Institute of Chemical Sciences of Rennes ICSR, University of Rennes 1, France.
- Dr. Mohammed Salah Aida, Professor, Taibah University, Saudi Arabia.
- Dr. Zagabathuni Venkata Panchakshari Murthy, Academic Member, ATINER & Professor/Head, Department of Chemical Engineering, Sardar Vallabhbhai National Institute of Technology, India.
- Dr. Alexander A. Kamnev, Professor, Institute of Biochemistry and Physiology of Plants and Microorganisms, Russian Academy of Sciences, Russia.
- Dr. Carlos Nunez, Professor, Physics Department, University of Wales Swansea, UK.
- Dr. Anastasios Koulaouzidis, Academic Member, ATINER & Associate Specialist and Honorary Clinical Fellow of the UoE, The Royal Infirmary of Edinburgh, The University of Edinburgh, UK.
- Dr. Francisco Lopez-Munoz, Professor, Camilo Jose Cela University, Spain.
- Dr. Panagiotis Petratos, Professor, California State University-Stanislaus, USA.
- Dr. Yiannis Papadopoulos, Professor of Computer Science, Leader of Dependable Systems Research Group, University of Hull, UK.
- Dr. Joseph M. Shostell, Professor and Department Head, Math, Sciences & Technology Department, University of Minnesota Crookston, USA.
- Dr. Ibrahim A. Hassan, Professor of Environmental Biology, Faculty of Science, Alexandria University, Egypt & Centre of Excellence in Environmental Studies, King Abdulaziz University, Saudi Arabia.
- Dr. Laurence G. Rahme, Associate Professor, Department of Surgery, Microbiology and Immunobiology, Harvard Medical School, Boston, Massachusetts & Director of Molecular Surgical Laboratory, Burns Unit, Department of Surgery, Massachusetts General Hospital, USA.
- Dr. Stefano Falcinelli, Academic Member, ATINER & Associate Professor, Department of Civil and Environmental Engineering, University of Perugia, Italy.
- Dr. Mitra Esfandiarei, Academic Member, ATINER & Assistant Professor, Midwestern University, USA.
- Dr. Athina Meli, Academic Member, Academic Member, ATINER, Visiting Scientist and Research Scholar, University of Gent & University of Liege, Belgium and Ronin Institute Montclair, USA.

- **Vice President of Publications:** Dr Zoe Boutsioli
- **General Managing Editor of all ATINER's Publications:** Ms. Afrodete Papanikou
- **ICT Managing Editor of all ATINER's Publications:** Mr. Kostas Spyropoulos
- **Managing Editor of this Journal:** Ms. Olga Gkounta (bio)

Reviewers' Board

Click Here

President's Message

All ATINER's publications including its e-journals are open access without any costs (submission, processing, publishing, open access paid by authors, open access paid by readers etc.) and is independent of presentations at any of the many small events (conferences, symposiums, forums, colloquiums, courses, roundtable discussions) organized by ATINER throughout the year and entail significant costs of participating. The intellectual property rights of the submitting papers remain with the author. Before you submit, please make sure your paper meets the basic academic standards, which includes proper English. Some articles will be selected from the numerous papers that have been presented at the various annual international academic conferences organized by the different divisions and units of the Athens Institute for Education and Research. The plethora of papers presented every year will enable the editorial board of each journal to select the best, and in so doing produce a top-quality academic journal. In addition to papers presented, ATINER will encourage the independent submission of papers to be evaluated for publication.

The current issue is the fourth of the eighth volume of the *Athens Journal of Sciences (AJS),* published by Natural & Formal Sciences Division of ATINER.

Gregory T. Papanikos, President, ATINER.

Athens Institute for Education and Research

A World Association of Academics and Researchers

10th Annual International Conference on Chemistry
18-21 July 2022, Athens, Greece

The Chemistry Unit of ATINER, will hold its **10th Annual International Conference on Chemistry, 18-21 July 2022, Athens, Greece** sponsored by the Athens Journal of Sciences. The aim of the conference is to bring together academics and researchers of all areas of chemistry and other related disciplines. You may participate as stream organizer, presenter of one paper, chair a session or observer. Please submit a proposal using the form available (https://www.atiner.gr/2022/FORM-CHE.doc).

Academic Members Responsible for the Conference

- **Dr. Ellene Tratras Contis**, Head, Chemistry Unit, ATINER & Professor of Chemistry, Eastern Michigan University, USA.

Important Dates

- Abstract Submission: **20 December 2021**
- Acceptance of Abstract: 4 Weeks after Submission
- Submission of Paper: **20 June 2022**

Social and Educational Program

The Social Program Emphasizes the Educational Aspect of the Academic Meetings of Atiner.

- Greek Night Entertainment (This is the official dinner of the conference)
- Athens Sightseeing: Old and New-An Educational Urban Walk
- Social Dinner
- Mycenae Visit
- Exploration of the Aegean Islands
- Delphi Visit
- Ancient Corinth and Cape Sounion

Conference Fees

Conference fees vary from 400€ to 2000€
Details can be found at: https://www.atiner.gr/fees

Athens Institute for Education and Research
A World Association of Academics and Researchers

10th Annual International Conference on Physics
18-21 July 2022, Athens, Greece

The Physics Unit of ATINER, will hold its **10th Annual International Conference on Physics, 18-21 July 2022, Athens, Greece** sponsored by the Athens Journal of Sciences. The aim of the conference is to bring together academics and researchers of all areas of physics and other related disciplines. Please submit a proposal using the form available (https://www.atiner.gr/2022/FORM-PHY.doc).

Important Dates

- Abstract Submission: **20 December 2021**
- Acceptance of Abstract: 4 Weeks after Submission
- Submission of Paper: **20 June 2022**

Academic Member Responsible for the Conference

- **Dr. Ethel Petrou**, Academic Member, ATINER & Professor and Chair, Department of Physics, Erie Community College-South, State University of New York, USA.
- **Dr. Bala Maheswaran**, Head, Electrical Engineering Unit, ATINER & Professor, Northeastern University, USA.

Social and Educational Program

The Social Program Emphasizes the Educational Aspect of the Academic Meetings of Atiner.

- Greek Night Entertainment (This is the official dinner of the conference)
- Athens Sightseeing: Old and New-An Educational Urban Walk
- Social Dinner
- Mycenae Visit
- Exploration of the Aegean Islands
- Delphi Visit
- Ancient Corinth and Cape Sounion

More information can be found here: https://www.atiner.gr/social-program

Conference Fees

Conference fees vary from 400€ to 2000€
Details can be found at: https://www.atiner.gr/fees

Athens Journal of Sciences- Volume 8, Issue 4, December 2021 – Pages 229-248

Waste Management and Control Problems in Sokoto Metropolis: Projected Mitigation on the Syndrome

By Yusuf Alapata Ahmed[*], *Nathaniel Bayode Eniolorunda*[+],
Yakubu Fakai Musa[±] *& Samuel Igra*[°]

This study assessed the nature of solid waste generation, its spatio-temporal pattern and existing management strategies in Sokoto metropolis. The greatest challenges facing cities in the developing world are; paucity of solid waste management and control. In the Nigeria context, solid waste management is characterized by inefficient collection, insufficient coverage of the collection system and improper disposal methods. In Sokoto metropolis, increase in population has resulted into accelerated of solid waste generation with pollution of all categories, and the consequent is dearth of modern management. The study used; selection of different wastes for observation, sampling-up four sub-soils at 0-30cm at random from each of the waste dump sites to determine not only for heavy metal concentrations but also for fertility supplement in comparison with the National Environmental Standard and Regulation Enforcement Agency (NESREA). Also, fifty scheduled questionnaires were administered each on selected residents around dumped sites and to the staff of Town Planning Board to solicit for relevant information on government and its agencies effectiveness in disposal and management of waste. Landsat data was also used to map out the waste sites for spatio-temporal analysis from 1999 to 2016. Results are expected to inform major decisions makers and urban planners in order to promote a sustainable urban development for Sokoto metropolis and its environs.

Keywords: *developing world, protection agencies, Metropolis, urban planners, Sokoto*

Introduction

The production and clearance of waste is an essential part of any developing society like Nigeria. Waste, both from domestic and commercial sources has grown significantly in Nigeria over the past decade. Every time a householder shops at the store, and open market he contributes to the mountain of waste (Iwegbue et al. 2006). It is possible to quote figures which show that the production of waste amounts to millions of tons. The percent of Nigeria's population living in cities and urban areas has more than doubled in the last 15 years (Jimoh 2005). The cities and

---

[*] Reader, Department of Geography and Environmental Management, Faculty of Social Sciences, University of Ilorin, Nigeria.

[+] PhD Student, Department of Geography, Faculty of Social Sciences, Usmanu Danfodiyo University, Nigeria.

[±] Lecturer 1, Department of Geography, Faculty of Social Sciences, Usmanu Danfodiyo University, Nigeria.

[°] Researcher, Department of Geography, Faculty of Social Sciences, Usmanu Danfodiyo University, Nigeria.

urban areas experience continuous growth which contributes to enormous in generation of solid and liquid waste. The management of waste is a matter of national and international concern. The volume of waste does not actually constitute the problem but the ability or inability of governments, individuals and waste disposal firms to keep up with the task of managing waste and the environment (Joseph et al. 2016). There is no doubt that a dirty environment affects the standard of living, aesthetic sensibilities, health of the people and thus the quality of their lives (Mowoe1990). Waste often generated by human beings since time immemorial has continued to be a threatening problem and a growing one that is of major concern to every nation of the world. In Nigeria today, among the pressing environmental and public health issues are the problems of solid waste generation, control and disposal. Although the problem of solid waste disposal is as old as man's existence that is inextricably linked to the generation of waste, the truth is that in many cities and urban centers, it has become so intractable that even the government is overwhelmed (Jimoh 2005, Momodu, et al. 2011).

Waste according to Douglas (2004) is any unwanted and discarded material that arises from the activities of humans and animals on earth. For Onwughara et al. (2010), urban solid waste (USW) covers a broad range of materials including garbage, refuse from factories, commercial refuse, construction and demolition debris, dead animals and abandoned vehicles, food particles, plastics, bottles, polythene material (nylon bag), metallic objects, furniture/wood material, paper and some other unclassified wastes. Rodgers (2011) submits that waste management is a systematic control of the generation, storage, collection, transportation, separation, processing, recovery and disposal of waste. Waste has been defined as something that is not or no longer useful and is to be thrown away or disposed of (Oxford Advanced Learner's Dictionary 1998). So also, waste has been defined as any material lacking direct value to the producer and so must be disposed of (Ita 2000). Among the European Community (EC), Waste Management Licensing Regulations 1999 came into force to implement the *Framework Directive on Waste* (Malcolm 1994, NESREA 2009). The Regulations also implement all of the remaining section of part II of the UK *Environmental Protection Act, 1990,* which defined waste as any substance which constitutes a scrap material or an effluent or other unwanted surplus substance from the application of any process (Atsegbua 2003). Generally waste poses a significantly different threat to human health in any environment, partly because of the manner in which it may be disposed or managed may not conform to proper standard. Waste therefore, is something which falls out of the normal commercial circle or utility. The European Commission (2020) suggests some broad category options which may be considered before or not an object is regarded as a waste: any worn out but still functioning substances or objects after repair is not a waste; objects which can be put to immediate use by a specialized waste recovery operation not to be considered as a waste; degenerated substances or objects which can be put to use only by establishments or undertaking specializing fall not to be regarded as wastes but any substance which the holder does not want and which he has to pay to be taken away are wastes, where the holder intends that the objects are to be discarded.

The above are only suggestive and would actually be meaningless except to rating authorities or waste disposal agencies who are interested in their fees for collection and disposal of waste.

In Nigeria, The Federal Environmental Protection Agency (FEPA) established an Act in 1988 No. 58; 1992 No. 59 and 1999 No. 14 with their functions and the powers for the effective implementation of such functions (FEPA 1989). But these acts did not define waste. Only some state statutes attempted to do so making some of them have different Edict as to control wastes (see list below). For example, section 32 of the Lagos State Environmental Sanitation Edict11 has a definition similar to the UK Environmental Protection Act 1990 (1st October 2017) 12, refers to waste as follows:

a. Waste of all descriptions.
b. Any substance which constitutes a scrap material, an effluent or other unwanted surplus substance arising from the application of any process.
c. The UK Act 1990 Integrated Pollution Control and Air Pollution Control by Local Authorities.

Institutions that Regulate Waste Control & Management in Nigeria

As part of proactive measures by Nigerian government to preserve the environment and protect its inhabitants from hazardous wastes and nuisance, as well to make it incumbent on all states of the federation to join in the crusade for hygienic standard in the country. Government and several states have established various governmental authorities and agencies that control and manage wastes in their respective areas. But it was discovered that only few States in the northern parts of the country are engaged in this practice. Therefore, the control and management of wastes is perilous and dwindle in Sokoto state in general. In Nigeria as a whole the following are the selected list of solid waste management stakeholders both at the Federal and States' levels (FEPA 1989).

- Federal Ministry of Environment (FMOE)
- Federal Environmental Protection Agency (FEPA)
- Lagos State Waste Disposal Board (LSWDB)
- Lagos State Environmental Protection Agency (LASEPA)
- Kano State Environmental Protection Agency
- Oyo State Environmental Protection Commission
- National Oil Spill Detection and Response Agency (NOSDRA)
- Federal Ministry of Environment, Housing and Urban Development (FMEHUD)
- Department of Petroleum Resources
- Kaduna State Environmental Protection Agency
- River State Environmental Protection Agency
- Anambra State Ministry of Environment, Mineral Resources, Science & Technology, Akwa

- Enugu State Environmental Protection Agency
- Abuja Environmental Protection Agency
- Adamawa State Ministry of Environment, Yola
- Away Ibom State Ministry of Environment & Mineral Resources, Uyo
- Bauchi State Environmental Protection Agency, Bauchi
- Baileys State Environmental Sanitation Authority, Yenagoa
- Benue State Environmental Sanitation Authority (BENSESA), Makurdi
- Borno State Ministry of Environment, Maiduguri
- Cross River Ministry of Environment, Calabar.
- Delta State Waste Management Board, Asaba
- Ebonyi State Ministry of Health & Environmental, Abakaliki,
- Edo State Environmental & Waste Management Board, Benin City
- Ekiti State Waste Management Board, Ado Ekiti
- Enugu State Waste Management Authority, Enugu
- Gombe State Environmental Sanitation & Protection Agency, Gombe
- Imo State Ministry of Petroleum & Environment, Owerri
- Jigawa State Rural Water Supply & Sanitation Agency, Dutse.
- Kaduna State Ministry of Environment & Natural Resources, Kaduna
- Kaduna State Waste & Sanitation Project, Kaduna
- Kano State Refuse Management & Sanitation Board (REMASAB), Kano
- Kano State Rural Water Supply & Sanitation Agency (RUWASA), Kano
- Katsina State Rural Water Supply & Sanitation Agency, Katsina
- Kebbi State Ministry of Environment, BirninKebbi
- Kogi State Ministry of Environment & Physical Planning Development, Lokoja
- Kwara State Environmental Protection Agency, Ilorin
- Niger State Environmental Protection Agency, Minna
- Ogun State Environmental Protection Agency, Abeokuta
- Ondo State Waste Management Authority, Akure
- Osun State Environmental Protection Agency, Osogbo
- Oyo State Ministry of Environment & Water Resources, Ibadan
- Plateau State Environmental Protection & Sanitation Agency, Jos
- River State Environmental Sanitation Authority, Port Harcourt
- Taraba State Environmental Protection Agency, Jalingo
- Yobe State Environmental Protection Agency, Damaturu
- Zamfara State Ministry of Environment & Solid Minerals Development, Zamfara
- Waste Management Society of Nigeria, Akwa Ibom

There are lots of reports being carried out on waste management and control especially in developed world and in the developing nations. Some of these reports are released by the International Solid Waste Association (ISWA) and the United Nations Environment Programme. ISWA has a total of more than 1,200 members in 93 countries. Its network expands to countries with more than 80% of the world's population. ISWA has three membership categories: national members, organization members and individual members. At present, there are 32 national members or incoming national members that represent their country on solid waste issues. ISWA's national members represent countries with 48% of the world population and 87% in terms of global GNP. ISWA's members represent all aspects of our field and most regions worldwide: from practitioners and industry to communities, from associations, research institutes and academics to regulatory authorities. The association is the global forum for waste management, with 12 technical working groups covering all relevant aspects of sustainable waste management and with special interest in developing countries issues:

- Working Group on Biological Treatment of Wastes.
- Working Group on Economic Analyses for Sustainable Development.
- Working Group on Hazardous Wastes.
- Working Group on Healthcare Waste.
- Working Group on Legal Issues.
- Working Group on Recycling and Waste Minimizations.
- Working Group on Sanitary Landfill.
- Working Group on Sewage and Waterworks Sludge.
- Working Group on Thermal Treatment.

The scope of this report is limited to the management of Municipal Solid Waste (MSW) (Hoornweg et al. 2012). Environmentally sound management of solid wastes environmentally sound waste management is recognized by most countries as an issue of major concern. For both developing and developed countries, waste management is an important factor in ensuring both human health and environmental protection. Article 21.4 of Agenda 21 states that 'Environmentally sound waste management must go beyond the mere safe disposal or recovery of wastes that are generated and seek to address the root cause of the problem by attempting to change unsustainable patterns of production and consumption.' Sustainable waste management is realized by using the technical, organizational and financial resources available in a particular locality.

Internationally, the management of solid waste is a huge challenge for municipalities in developing nations. Previous studies point out that increase in population with relating concomitant urbanization dynamics and growth of conurbations will further exacerbate this challenge (Bogner et al. 2005). Monni et al. (2006) reported on five global scenarios compiled from 1990 to 2050 on global post-consumer waste generation. They stated global emissions from landfills in 1990 to be 340 Tg CO_2 eq with an increase to 1,500 Tg CO_2 eq by 2030 and to 2,900 Tg CO_2 eq by 2050. Laurent et al. (2014) and Zhang et al. (2019) more recently reviewed greenhouse gas (GHG) emissions from landfills and listed a number of important mitigation methods as well as development and dissemination of updated knowledge-based frameworks. At present, the World Bank affirms 2.01 billion metric tons of municipal solid waste. MSW are produced annually worldwide, with estimates reaching 3.40 billion metric tons by 2050 (Sipra et al. 2018). Current worldwide estimates indicate that, 13.5% of waste is recycled and

5.5% is composted, with an estimated one-third and 40% of MSW as not managed properly and instead dumped or openly burned (Huang et al. 2006). This mismanagement is significantly split between developed and developing countries. For example, about 80% of solid waste in African countries is dumped indiscriminately in open spaces, streets, storm water drains, rivers, and streams (Afon and Okewole 2007), thereby, estimated to contribute to about 29% of the global GHG emissions and expected to increase to 64% by 2030. This is largely due to uncontrolled population growth and affluence, unsustainable development activities, and expansion of waste collection services without sufficient management strategies (i.e., changes from dumpsites to sanitary landfills with a lack of landfill gas collection). Dladla et al. (2016) identified factors associated with indiscriminate dumping of waste in eleven African countries (Nigeria inclusive) and found institutional weaknesses and lack of awareness as key starting points to the problem. Lack of public perception can be a limitation to what can be done and, ultimately, to what can be achieved (Yuan et al. 2019). African countries that are heavily inundated with indiscriminate MSW constitute health challenges to residents of the area as GHGs are released (Zhang et al. 2019). Institutional weaknesses may occur in the form of ambiguity of waste management policy and legislation since MSW activities effect the core infrastructural framework of a municipality and its residents. Hence, increasing awareness of inhabitants may have a positive impact on attitude as well as perception towards the environment.

Nigerian cities are largely characterized with having solid waste disposal problems. They are typified by overflowing dumpsters, mountains of open refuse dumps (i.e., on virtually every street), and makeshift landfills on the edge of larger suburbs and towns. Attendee problems are also evident, especially where burning occurs, since properly operated landfills are nonexistent and often rodent infested with surface and ground water pollution concerns (Cirella et al. 2019). As such, the collection and transport of MSW requires the largest demand on municipal budgets but has been seen to have the greatest impact on urban living (UN-HABITAT, 2010). Oseghale (2011) and Ezeudu and Ezeudu (2019) reported that in Nigeria 68% of MSW is indiscriminately dumped, 20.8% is disposed through inappropriate landfill sites, and 10.7% is burnt. According to the GHG emissions inventory from 2000 to 2018 the contribution from inappropriate waste was 3.0% (FME 2018), which is expected to double within the next five years, considering that waste generation rate is estimated between 0.5 and 1.0 kg/person/day Oseghale (2011); however, this is subject to change due to unplanned population growth and unsustainable urban waste management practices Nigeria. Moreover, Ossai (2020) illustrated the complexity of waste composition Nigeria, stating biodegradable waste accounts for about 50% of annual MSW with less than 10% of waste as manageable.

Federal Ministry of Environment (FME) (2018), says Benin City, the largest urban center in Edo State, in southern Nigeria houses much of the challenges, thus far, described. Many of its suburbs (residential areas and public places) are littered with domestic and sewage waste, garbage, and chemical waste. Industrial operation is characterized by the generation of large volume of MSW in the form of solid, liquid and gas—some toxic. As a result, the Edo State Waste Management Board

(EWMB), established by the local authorities, put in place a monitoring program to regulate environmental quality and implement steps towards a waste-free society. Despite its efforts, Benin City still falls short of achieving Board benchmark levels and ongoing waste management practices are needed. This paper examines an in-depth look at the level of awareness and attitude of its inhabitants towards MSW disposal and possible contribution to regional GHG emissions. The research is in accordance with the local government, with the intention of enhancing MSW management programs for other Nigerian cities and beyond which face similar problems.

Methods

The methods employed for this work are highlighted below: In the first place, reconnaissance visits were carried out by the researchers on different occasions at different locations within Sokoto metropolis for On-the-spot assessment and for Focus Group Discussion (FGD). This was done in as to discover the locations of dumpsites (Legal or Illegal sites) and to update information collected from the secondary data source. Mapping of major waste sites in the metropolitan areas were also put in place based on snowball sampling method. The outline coordinates of the waste sites were taken by walking around the boundaries of the waste dump sites with the aid of a hand-held Global Positioning System (GPS). Map of Nigeria states and capitals were displayed to show list of solid waste management /stakeholders in the Federal and States with their respective locations (see Figure 1). Sites were also observed and photographed to see some category of wastes composition and waste characteristics based on soil sampled from the waste sites respectively (see Figure 3). The results of the outcome were discussed in details within next paragraphs.

Figure 1. *Nigeria States & Capital Cities*

Source: ontheworldmap.com.

Figure 2. *Few Waste Sites in Sokoto Metropolis*

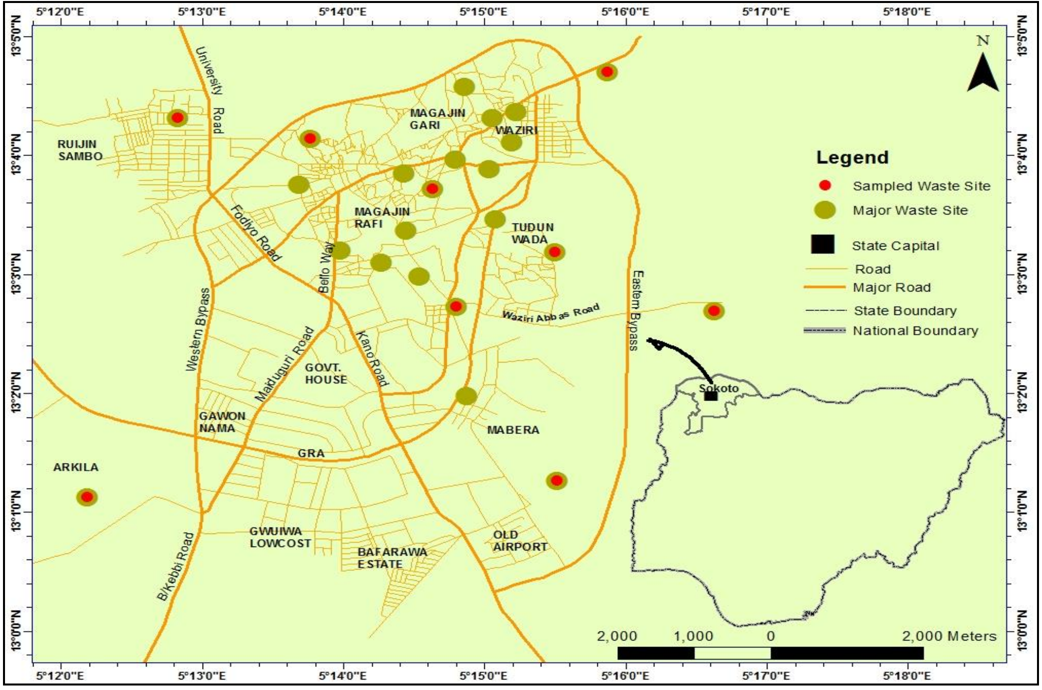

Source: Authors' Compilation.

Soil Sampling and Composition of Waste Materials in Sites

The material compositions of wastes in Sokoto metropolis were determined through soil samples that were collected from the sites by the use of Soil Auger from 0-15cm depth. Samples were collected from each site in four replicates which were bulked, out of which a portion was taken in a clean polythene bag for laboratory test. Samples were provided as thus:

Sample Digestion for Heavy Metals

The soil samples were air dried for 72 hours, grounded and sieved with 2mm mesh from which the representative sample was obtained. One gram of the air dried soil was taken from each sample and placed in a 100cm^{3}Kjeldahl digestion flask and treated with 2cm^3 of 60% chloric (V) acid ($HClO_4$), 10cm^3 of concentrated nitric acid (HNO_3) and 1.0cm^3 concentrated sulphuric acids (H_2SO_4). The mixtures were swirled gently and slowly at a moderate heat on the digester for 15 minutes and allowed to cool down, and later diluted with 50cm^3 of distilled water. The mixture was filtered through a filter paper into a 100cm^3 volumetric flask and used for test using the Atomic Absorption Spectrophotometer (AAS) (Akoto et al. 2016, Tijani et al. 2007). The results of the tests remitted the followings: It was discovered that soils of the waste dump sites were enriched with the heavy metals (Zn, Cu and Cd) more than the adjacent soils (control) but were still within critical levels.

Heavy Metal Analysis

The mean concentration for each heavy metal for all the sites was also tested with one-sample t-test against the NESREA standard to know whether it is safe for agricultural use or not.

Major Waste Sites Commonly Found in Sokoto Metropolis

Waste sites are usually found in the streets of the residential areas, behind walls of school buildings and places officially designated as dump sites provided with incinerators.

Material Composition of Waste Sites

Materials found are essentially household wastes such as polythene bag, paper, remnants of food, human and animal feces, metals and bottles, wood and plant remains.

Heavy Metals in Soils at the Waste Site

The heavy metals tested include zinc, lead, manganese, chromium and cadmium. The concentrations of the metals are presented in tables (see Tables 1 and 2). Also, Table 2 presents the critical values of the heavy metals by National Environmental Standards and Regulations Enforcement Agency (NESREA 2009, Bahaa-Eldin et al. 2008).

Table 1. *Soil Heavy Metal Concentrations at Waste Sites*

S/ No.	Concentration of the Metals				
	Waste Sites in Sokoto Metropolis	**Zn**	**Pb**	**Cr**	**Cd**
1	Ruijin Sambo	0.594	0.397	0.076	0.016
2	MagajiGari	0.174	0.513	0.112	0.007
3	Waziri area	0.101	0.533	0.235	0.007
4	Magaji Rafi area	0.242	0.383	0.183	0.010
5	Tudun Wada	0.493	0.344	0.131	0.017
6	Waziri Abbas area	0.691	0.221	0.221	0.023
7	Eastern bye-pass	0.348	0.524	0.168	0.026
8	Mabera area	0.890	0.442	0.217	0.008
9	Arkila	0.131	0.338	0.141	0.011
Mean Total		0.407 ± 0.28	0.411 ± 0.10	0.165 ± 0.05	0.014 ± 0.001

Source: Authors' Compilation.

Table 2.*Critical Limits for Heavy Metals in Soils*

Metals	Zn	Pb	Cr	Cd
Critical Limit	421	164	100	3

Source: NESREA 2009.

Challenges of Waste Disposal in Sokoto Metropolis

In Sokoto metropolis, just as in some urban centers and cities in Nigeria, recycling activities are not popular and are almost none existence. But, the recovery of items from wastes (scavenging) is being practiced on a large scale. This type of recovery takes place at both legal and illegal dump sites where scavengers search continually for valuable items like; metals, plastics, and bottles to be reused or for sale to buyers of different type as scraps (Ahmed et al. 2017, Oyedele et al. 2008). In general, treatment of solid wastes is not often carried out in Nigeria. Incineration of wastes or use of approved sanitary landfill is non-existent. The most common practice is open dumping and burning of waste within residential areas and at illegal and legal dumps are very common in some major urban centers like; Sokoto and other places in the northern parts of Nigeria. Other strategies employed in disposing waste in the country include; collection, composting, transfer and bury all which are not modern means of waste management.

Most of the above are crude measures of wastes management and control and they are improper disposal or storage of waste that constitute hazards to the society through the pollution of air, land and water. Thus, waste management has become a common issue of discourse among individuals, groups and governments and there is the need for its overhaul development to meet the modern world standard (Partha et al. 2011).

Roles Play SEPA on Waste Management in Sokoto

The major roles of the Sokoto Environmental Protection Agency (SEPA) are to keep the metropolis clean, collect and evacuate household solid wastes at designated points in the metropolis and enforce compliance with sanitary rules and regulations. SEPA is the only authorized body vested with waste management responsibility, although scavengers usually engage themselves at the waste sites collecting metal parts, plastic materials and other items that can be industrially reused or recycled. However, the wanton littering of the streets with heaps of wastes is an illustration of the fact that the Agency is overwhelmed. The process of keeping the metropolis clean involves a general sanitation exercise observed for three hours once in a month, and this takes place on the last Saturday of the month. The exercise is expected to involve every able inhabitant of the metropolis cleaning his or her environment between 7am and 10am within when vehicular movements are not allowed. However, this practice has remained a mere observance as movements only get restricted with little participation by the city residents. Surroundings are supposed to be swept while wastes derived from the activity are expected to be deposited at designated receptacles and areas from where they are collected by the SEPA.

Wastes are either dumped at open spaces indiscriminately at points designated by inhabitants of an area or into receptacles provided by the Agency, the capacities of which are fast exceeded largely due to the high volumes of generated waste. The receptacles are either metallic containers or refuse bunkers located at strategic places. Nonetheless, residents fail to access the points, thereby dumping piles of rubbish which normally litter the roads and street corners of the metropolis. This situation is worse in densely populated areas of Sokoto city center such as; Sarkin Zamfara B ward, Sarkin Zamfara ward A, Rijia ward A, Rijiya ward B and Sudan Wada Ward A and B respectively (in Sokoto South LGA). It is also very visible in areas like Magajin-Garin ward A and B and Waziri Ward A and B respectively (in Sokoto LGA) of Sokoto metropolis as evident in Figures 3-10.

Characteristics of Wastes Generated by Households in Sokoto City

The types of solid waste generated by households in the metropolis are biodegradable and non-biodegradable. The biodegradable waste include vegetables, food remnants, paper, cartons, textile materials, animal carcass, leaves, grasses, and wood products which constitute approximately 98% of the total waste being generated. While, a negligible amount of non-biodegradable waste includes; bottles, glass, polythene bags, plastic materials and scrap metals are generated, evacuated and disposed daily. An approximate amount of solid waste generated, evacuated and disposed daily is about 750,000kg (750tons), weekly 5,250,000 kg (5,250tons), monthly 21,000,000kg (21,000tons) and yearly at about 252,000,000kg (252,000tons). The waste materials collected by SEPA have either spilled to the ground from the receptacles due to overuse or are intentionally dumped on the ground in massive proportions by the residents. In collecting solid wastes at such sites, heavy equipment such as bulldozers, pay loaders, tractors, trucks and tippers, wheelbarrows, shovels, forks, among others are used. Waste transportation is carried out by high capacity tippers so that they can convey high volumes over long distances to the treatment sites. These wastes conveyed by the carriers (Figure 8) are routinely contained with tarpaulin so they do not get blown out of the vehicle in transit, thereby becoming stranded and dirtying the roads; also, the wastes are contained to prevent escape of noisome odors from the waste.

Figure 3. *Waste Dump Site at Maituta Road*

Figure 4. *Waste Dump Site at Sarkin-Zamfara ward 'A'*

Figure 5. *Waste Dump-site at Sarkin ZamfaraWard 'B'*

Figure 6. *Waste Dump Site at Rijia-Ward 'A'*

Figure 7. *Waste Dump Site at TudunWada Area*

Figure 8. *Equipment for Evacuating Solid Waste*

Figure 9. *SEPA's Metal Skip for Safe Refuse*

Figure 10. *Opened Waste Dump Site Disposal at Waziri Ward 'A'*

Results and Discussion

On the general feeling of respondents on the cleanliness of the metropolis, 89% of them agreed that Sokoto metropolis is dirty. They argued that the metropolis is characterized by heaps of household solid wastes which are left stranded for long periods of time before evacuated. As some of the generated wastes are biodegradable, most streets especially in the congested areas remain air polluted, mosquito infested and littered with nylons of different types.

On the mechanism used by households to control solid waste in the metropolis, most respondents claimed SEPA provided refuse bunkers and metal skip that are distributed at strategic locations within the metropolis, but are grossly inadequate and located at far distances from most residents. This however has made the residents of the metropolis to adopt the method of designating an open space as household solid waste dump site. Other residents have equally cultivated the habit of dumping their waste in nearby bushes and uncompleted buildings or open plots of land, and in front of drainage along major streets. Some residents indiscriminately dump waste in front of their houses while some rich individuals among them organized for the services of private firms or local scavengers who go about with wheel barrows to collect household solid wastes from homes on payment services. These groups of refuse collectors are mostly found every morning in densely populated areas of the metropolis and commercial areas of Emir Yahaya Road, Rijiya Area, Old Airport Area, Ahmadu Bello way, Zoo lane area, Jallen Area and Fodio Road Area respectively to render their services. This practice of indiscriminate refuse dumping has led to the situation in which improperly sited open dumps deface several parts of the major roads, streets, street corners and high ways in the metropolis with exposed and fermenting refuse with repugnant, offensive and nuisance odors almost everywhere in the metropolis.

On the frequency of waste evacuation by SEPA, 74% of the respondents argued that wastes at their area are evacuated about once a month, while 26% could not be specific but maintained that the frequency is low. In terms of the mechanism of waste management, 56% of the respondents argued that best and standard practices have not been adopted by SEPA. According to them, the use of heavy duty trucks and earth moving machineries that driven and operated for many hours in the densely populated environment cause noise and air pollution which is detrimental to human health. This is besides the traffic impendence that comes with the operations of these heavy duty machineries. About 90% of the respondents also argued that SEPA transports waste materials without covering the loaded trucks with tarpaulin, thereby making the materials in transit to fly and drop on the roads. Thus, such materials find their ways into the drainage channels to cause further problem.

Other salient reasons in which mechanism adopted for household solid waste collection and disposal could not be said to be one of the best standard practice could be traced to the unplanned houses, narrow and none paved winding roads, streets and degraded environment which prevent timely evacuation of piles of rubbish littering the roads and street corners. Respondents further argued that lack of adherence to city planning is a fundamental reason for inaccessibility. It could also hamper the free movement of appropriate refuse collection and disposal equipment such as compactor trucks.

In the case of waste control and management in Sokoto through heavy metal concentrations studies, this was found to be below the critical limits set by the NESREA. The waste materials that generate them are essentially domestic. This gives a room for a guess that perhaps domestic wastes are fewer sources of heavy metals than industrial wastes which is partly why low values were observed in this study. It is also safe to infer that sandy soil which largely characterizes the study area is partly responsible for the observed concentrations as leaching that occurs mostly in sandy soils around the metropolis.

Upon all the government efforts to alleviate poor waste management and control in Sokoto metropolis, a number of challenges still continued to crop up as a result of the following.

- Dwindle of moral ethics towards environment enlighten on which most people are yet to learn or comply due to their indifferent attitudes towards environmental management and control.
- Increasing migrant traders into the city from all over neighboring states and countries that continuing to increasing the quantity of waste generated, thus making it more difficult to make adequate provision to commensurate with wastes generated.
- Distribution of heavy metals [lead (Pb), copper (Cu) and zinc (Zn)] is relevant in surface soil study (e-waste) and, recycling. The evaluationof pollution size (spot size, small area or larger), as well as assess to heavy metal transport into the surrounding soil environment have its challenges in Sahellian region like Sokoto (Fujimori and Takigami 2014).
- No enough manpower to manage wastes as there are just few sanitation and environment engineers in the state. Whereas, most private sector operators in waste management are mainly political stalwarts and who have little knowledge about waste control and management.
- Weak enforcement agency mostly in developing countries also makes people to be careless with waste management policies.
- Lack of modern technology/lethargy.
- Poor funding by Waste Management Agency i.e., in places where people pay to dispose waste makes it a challenge for the financially less privileged to comply with such policies (Ahmed et al.2017).

This study which assessed urban solid waste management in Sokoto state with its attention focused on city of Sokoto specifically, the work sought to find out why indiscriminate solid waste dumps/disposal have persisted in the city. We intend to investigate the measures to put in order to curtail the tide and ascertain the extent to which indiscriminate waste disposal affects people’s health and environment and other ways of life. Evacuated wastes are dumped at the designated treatment points only in the outlying parts of the metropolis. While dumping distance not enough to prevent pollution to the city. Some dumping of refuse is done in the open spaces while others are at any available pits. Because Sokoto metropolis experiences high and frequent winds and since the capacity to industrially recycle wastes is lacking, the wastes are incinerated to prevent them from getting transported back to their origins by winds. Incineration is also carried out to prevent mosquito breeding at the treatment sites. On the challenges faced by the SEPA, many residents of the city cited paucity of funds, inadequacy of equipment, inaccessibility of some streets especially the congested and unplanned areas and non-compliance of the residents to sanitary rules and regulations as the main problems bedeviling the Agency’s operations. According to them, funds are grossly inadequate to purchase the necessary equipment like row-row, waste bins, towing vehicles, waste pulverization machines among other modern gadgets for daily use by waste managers.

Conclusions

The findings of this study leave nobody in doubt about the devastating effects of urban solid waste in Sokoto metropolis as a result of inapt and dwindling waste management. We therefore put forward that both the individuals and the government through SEPA have some decisive roles to play in synthesis residents of metropolis on efforts to educate them about health living standard by all and sundry. As the resultant negative consequences will have multiplier effects on the present and future inhabitants of the metropolis. Government is therefore advised to re-orientate the masses through enlightenment campaigns about best ways to dispose solid wastes with the seriousness they deserve if they must keep faith with protecting the environment and lives of people in Sokoto states in general. The study avers that SEPA's waste control efforts are grossly inadequate, besides their collecting bins spots locations that are too far from one and another, and/or partly the residents manage their waste products by indiscriminate dumping on different illegal avenues by households. All these measures must be discouraged, while SEPA is encouraged from all measures that hampering their progress such as poor funding, inadequate machinery and unplanned nature of most parts of the metropolis which imposes considerable limitations on waste evacuation, deposition and outright total disposal.

Recommendations

In line with the findings from this study and its implications, the following predictable mitigation features are put forward on the syndrome to serve as futuristic solutions to the waste management challenges in Sokoto metropolis.

i. Sokoto State in general, should as a matter of urgency strengthen the already established SEPA to manage and preserve the environment, and protect its inhabitants from hazardous waste problems by making it incumbent on all Local Government Areas in the state, to join hands in the crusade for hygienic standard in their areas.
ii. The State Government could not shoulder all the brunt of waste control and management, but government should establish partner with firms under public-private-partnership (PPP) arrangement to commence operation in the state as co-specialists in waste management operation that would include: waste generation, sorting/separation, recycling and conversion as it is being done in some modern cities of the world (Bahaa-Eldin et al.2008).
iii. State government should as a matter of urgency; provide permanent waste dumpsites that must be far away from health service centers, markets,

schools, churches, commercial and residential areas. This will curtail the risk of infectious diseases catch and spread within the city environment.

iv. Landlords/head of households and other residents within the metropolis should be appropriately represented and well informed when planning for any new waste control management strategy.

v. Institutions like; Primary and secondary school should incorporate in their curricula relevant and important topics on waste control, this would make all students have knowledge of waste management from grassroots.

vi. The various media organizations including radio, television, magazines, and newspapers and so on should complement government's efforts to sensitize the residents on the dangers of dirty environment and the need to maintain good personal and environmental hygiene.

vii. All the above suggestions could work if followed with regular public enlightenments, symposia, workshops and seminars to sensitize residents on the modalities for waste control from point of generation to collection and disposal centers which must be increased beyond the current limited SEPA equipment.

viii. Employment of more skilled officers in environmental pollution control and waste management into SEPA would be another added advantage, they could as well work together with other health management bodies in the State in order to jointly uplift health condition of all the populace in Sokoto State and Nigeria in general.

References

Ahmed YA, Muhammed AA, Oyewo SO (2017) Health impact of leachates from illegal *dumpsites: case study of Kubwa Abuja, Nigeria. Ethiopian Journal of Environmental Studies and Management* 10(1): 125–136.

Afon AO, Okewole A (2007) Estimating the quantity of solid waste generation in Oyo, Nigeria. *Waste Management & Research: The Journal for a Sustainable Circular Economy* 25(4): 371–379.

Akoto O, Nimako C, Asante BD (2016) Heavy metals enrichment in surface soil from abandoned waste disposal sites in a hot and wet tropical area. *Environmental Processes* 3(Aug): 747–761.

Atsegbua LA (2003) *Environmental law in Nigeria: theory and practice*. Lagos, Nigeria Ababa Press.

Bahaa-Eldin EAR, Yusoff I, Rahim SA, Zuhairi WYW, Ghani MRA (2008) Heavy metal contamination of soil beneath a waste disposal site at Dengkil, Selangor, and Malaysia. *Soil and Sediment Contamination* 17(5): 449–466.

Bogner J, Spokas K, Chanton J, Powelson D, Abichou T (2005) Modeling landfill methane emissions from biocovers: a combined theoretical-empirical approach. In *Proceedings of the Sardinia 2005 International Solid and Hazardous Waste Symposium* (CISA). University of Cagliari.

Cirella GT, Iyalomhe FO, Adekola PO (2019) Determinants of flooding and strategies for mitigation: two-year case study of Benin City. *Geosciences* 9(3): 136.

Dladla I, Machete F, Shale K (2016) A review of factors associated with indiscriminate dumping of waste in eleven African countries. *African Journal of Science Technology Innovation and Development* 8(5–6): 475–481.

Douglas SE (2004) The politics of Nigeria underdevelopment. *Journal of Policy and Development Studies* 1(2) 34–39.

European Commission (2020) *Circular economy in cities*. European Commission.

Ezeudu OB, Ezeudu TS (2019) Implementation of circular economy principles in industrial solid waste management: case studies from a developing economy (Nigeria). *Recycling* 4(4): 42.

Federal Environmental Protection Agency – FEPA (1989) *National policy on the environment.* Federal Republic of Nigeria.

Federal Ministry of Environment – FME (2018) *First biennial update report under the united nations framework convention on climate change*. Abuja: Federal Ministry of Environment.

Fujimori T, Takigami H (2014) Pollution distribution of heavy metals in surface soil at an informal electronic-waste recycling site. *Environmental Geochemistry and Health* 36(1): 159–168.

Hoornweg D, Bhada-Tata P (2012) *What a waste: a global review of solid waste management.* Urban Development Series; Knowledge Papers No. 15. Washington: World Bank.

Huang Q, Wang Q, Dong L, Xi B, Zhou B (2006) The current situation of solid waste management in China. *Journal of Materials Cycles and Waste Management* 8(1): 63–69.

Ita M (2000) *Waste – Is the developing world ready*. Science in Africa.

Iwegbue CMA, Isirimah NO, Igwe C, McWilliams ES (2006) Characteristic levels of heavy metals in soil profiles of automobile mechanic waste dumps in Nigeria. *The Environmentalist* 26(2): 123–128.

Jimoh IA (2005) A new approach to municipal waste management in Nigeria. In *International Conference on Energy, Environment and Disasters–INCEED.* USA: Charlotte N.C.

Joseph ON, Chinyere N, Chidi I (2016) Urban solid waste management and environmental sustainability in Abakaliki Urban, Nigeria. *European Scientific Journal* 12(23): 153–185.

Laurent A, Clavreul J, Bernstad A, Bakas I, Niero M, Gentil E (2014) Methodological guidance for a better practice. *Waste Management* 34 (3): 589–606.

Malcolm RA (1994) *Guide to environmental law, EC directive 91/156*. London: Sweet & Maxwell.

Momodu NS, Dimuna KO, Dimuna JE (2011) Mitigating the impacts of solid wastes in urban centers in Nigeria. *Journal of Human Ecology* 34(2): 125–133.

Monni S, Pipatti R, Lehtila A, Savolainen I, Syri S (2006) *Global climate change mitigation scenarios for solid waste management.* Espoo: VTT Technical Research Centre of Finland.

Mowoe KM (1990) Quality of life and environmental pollution and protection. In JA Omotola (ed.), *Environmental Law in Nigeria*. Lagos, Nigeria: Faculty of Law, University of Lagos.

National Environmental Standards and Regulations Enforcement Agency – NESREA (2009) *National environmental (sanitation and wastes control) regulations.* NESREA.

Onwughara IN, Nnorom IC, Kanno OC (2010) Issues in roadside disposal habit of municipal solid waste environmental impacts and implementation of sound management practices in developing country "Nigeria". *International Journal of Environmental Science and Development* 1(5): 23–31.

Oseghale P (2011) *Waste management handling in Benin City*. Helsinki: Arcada University of Applied Sciences.

Ossai OS (2020) Comparative evaluation of qualitative and quantitative biogas production potential of oil palm fronds and co-digestion with cow dung. *Journal of Energy Technologies and Policy* 3(4): 25–33.

Oxford Advanced Learner's Dictionary (1998) *Special price edition*. England: Oxford University Press.

Oyedele DJ, Gasu MB, Awotoye OO (2008) Changes in soil properties and plant uptake of heavy metals on selected municipal solid waste dump sites in Ile-Ife, Nigeria. *African Journal of Environmental Science and Technology* 3(5): 107–115.

Partha V, Murthy NN, Saxena PR (2011) Assessment of heavy metal contamination in soil around hazardous waste disposal sites in Hyderabad city (India): natural and anthropogenic implications. *Journal of Environmental Research and Management* 2(2): 27–34.

Rodgers M (2011) *Fundamentals of development administration.* London: S. Publishers.

Sipra AT, Gao N, Sarwar H (2018) Municipal solid waste (MSW) pyrolysis for biofuel production: a review of effects of MSW components and catalysts. *Fuel Processing Technology* 175(Jun) 131-147.

Tijani MN, Okunlola OA, Ikpe EU (2007) A geochemical assessment of water and bottom sediments contamination of Eleyiele Lake Catchment, Ibadan, Southwestern Nigeria. *Journal of Mining and Geology* 19(1): 105–120.

UK Environmental Protection Act 1990 (2017, October 1) Waste definition for community. UK: Environmental Protection Agency.

UN-HABITAT (2010) *Solid waste management in the world's cities: water and sanitation in the world's cities*. London: Earthscan.

Yuan X, Fan X, Liang J, Mengyue L (2019) Public perception towards waste-to-energy as a waste management strategy: a case from Shandong, China. *International Journal of Environmental Research and Public Health* 16(16): 2997.

Zhang C, Xu T, Feng H, Chen S (2019) Greenhouse gas emissions from landfills: a review and bibliometric analysis. *Sustainability* 11(8): 2282.

Athens Journal of Sciences- Volume 8, Issue 4, December 2021 – Pages 249-272

Mineral Exploration in Mawat Region, Kurdistan-Iraq, Based on Satellite Data and Terrain Prospection

By Marinko Oluić[*], Sreten Romandić[±] & Ratko Vasiljević[°]

The main goal of the presented exploration was to estimate potential for mineralization in the Mawat ophiolitic massif in Kurdistan, Iraq. The aim of the study was to explore existing copper mineralization and assessor elements gold, platinoids and chromium. Geological exploration detected two types of Cu occurrence a) secondary Cu carbonates (malachite) and b) Cu sulfides (chalcopyrite-pyrite). The Mawat region is mostly built of ultrabasic and basic rocks: peridotites, gabbros, serpentinites and basalts which are heavily deformed, with faults mostly oriented NNW-SSE, and NE-SW. The first phase of exploration comprised digital processing of ASTER and QuickBird satellite images, with appropriate geometrical and radiometric corrections and transformation into coordinate system. Color composite images were produced in different scales. They served to define lithological composition, tectonic settings, location of the points of interest etc. The field work was designed to check satellite data in situ, with focus on perspective rock formations, which might host copper mineralization, and other elements. The host rocks of the ore occurrences are primarily gabbros and metagabbros intersected by diabase dykes, epidote and quartz veins. Secondary mineralization is the product of surficial weathering and it is represented by malachite and limonite. The geophysical survey was very useful in the detection of area with elevated induced polarization and low resistivity. Three perspective areas have been selected for detailed explorations: Waraz, Mirava-Chenara and Konjirin-Kuradawi. The concentration of copper varies highly in very wide ranges; the maximum measured concentration of Cu was determined in Waraz area 6.7%. Some rock samples also show concentration of gold from 0.36 to 2.59 ppm Au.

Keywords: *Mawat ophiolitic massif, geologic-geophysical explorations, copper mineralization, Kurdistan-Iraq*

Introduction

The goal of this exploration was to estimate potential for mineralization of Mawat ophiolitic massif in Kurdistan, Iraq. The aim of the study was to explore existing mineralization of copper as well as of other metals like gold, platinoids, chromium etc. The explored area has about 250 km^2, about 40 km^2 of which was selected for detailed exploration of mineral resources. In addition to geologic-geophysical survey, satellite *ASTER* and *QuickBird* imagery have also been used. Color composite images were produced in different scales, which served for rock discrimination, registration of tectonic elements, location of control and sampling

---

[*] Researcher, GEO-SAT Ltd, Croatia.
[±] Researcher, GEO-SAT Ltd, Croatia.
[°] Researcher, ECOINA Ltd, Croatia.

points, etc. The field work was designed to check satellite data *in situ,* with focus on perspective rock formations, which might host mineralized rocks. The ore host rocks are primarily gabbros and metagabbro intersected by diabase dykes and epidote and quartz vein.

Secondary mineralization is the product of surficial weathering and is represented by malachite and limonite. The geophysical explorations were applied in detection of anomaly area (inducted polarization-*IP*, magnetic resistivity and *SP* methods) and proved very useful.

Three areas: *Waraz, Konjirin-Kuradawi and Mirava-Chenara area* were selected as potential by perspective for increased mineralization and were subjected to detailed exploration and sampling for chemical and petrological analyses. Measurement Cu in rock samples in ppm are as follows: Waraz area 1.53-60,705 ppm, Konjirin-Kuradavi 68-36287 ppm and Mirava-Chenaran 135-16,803 ppm. Maximum value of 6.7% Cu was determined in Waraz area. In some rock samples the gold concentration of 0.36 and 2.59 ppm were registered.

Study Area

The study area is situated in northeastern part of Iraq (Kurdistan), about 30 km north of Sulaimany City (Figure 1), with topography altitudes which range from ca 940 m (south part) to more than 1,400 m a.s.l. (north part). The main ultramafic body represents low area, surrounded by high peaks made of mafic intrusions which are grey and dark green in color showing pseudo stratification.

Figure 1. *Positional of the Explored Area in Mawat Region, Kurdistan-Iraq*

Source: Oluić et al. 2007.

Geological Setting

According to previous geological studies, the studied area belongs to the Zagros Mt. chain which extends SE-NW. It is a young Alpine orogeny formed by collision of African elements with Eurasian continental plate, and closing the Tethyan Ocean (Ismail et al. 2017). The Zagros orogenic system consists of several large distinctive geotectonic units which correspond to Cretaceous-Palaegene subduction of the Arabian plate beneath the Central/East Iran microplate, which is still active in the prolongation within the Gulf area. A wider area is built of Arabian platform formations, covered by Tertiary foreland units. Early foreland formations are *Kolosh Tanjero, Shiranish,* and late foreland formations are *Sinjar, Gercus, Pila Spi, Lower Fars* and *Upper Fars* (Hassan et al. 2015). These molasse formations are overthrust by ophiolitic mélange incorporated within the Qulqula Uper Cretaceus hinterland group. They indicate a regional Zagros nappe system and have a tongue-shaped form, named Mawat Nappe. Its central part consists of ophiolite and metamorphic rocks, surrounded by outcrops of Red bed series, as well as Naopurdan Series. Al-Mehaidi published Simplied geological map of Mawat Ophiolite Complex NE Iraq (Al-Mehaidi 1974).

More detailed chronological overview of earlier studies is given in the following section.

Previous Studies

Mawat ophiolitic massif was studied by numerous geologists. Bolton (1955) made the first geological map of this region and discussed tectonical zones as well as economic prospects of the area, and named, and distinguished both Bulfat and Quandil thrust blocks.

Geology of the central sector of the Mawat igneous rocks has been published by Jassim (1975). The dispersion of Cu, Ni, and Cr mineralization in Mawat ophiolite complex was reported by Al-Hashimi and Al-Mehaidi (1975). The northern part of studied area was explored by Hamasalh (1982) who wrote that ultramafic rocks comprise peridotites, dunites, pyroxenites and hornblendites which contain more than 90% mafic minerals.

Zagros Upper Cretaceous ophiolites as well as similar-aged ophiolites in Turkey, Cyprus and Oman are coeval and represent remnants of a late Cretaceous oceanic fore-arc formed along the southern margin of Eurasia. Zagros ophiolites and other Upper Cretaceous Tethyan ophiolites of SW Asia are broadly similar in terms of age, lithological components and geochemical evolution (Moghadam and Stern 2011).

The Mawat extensional basin formed without creation of new oceanic basement. During the extension, huge volumes of mafic lava were intruded into 3 block during the Late Cretaceous. The Mawat complex does not show a typical ophiolite sequence, and it is composed mainly of mafic rocks, which have been intruded into an extensional tectonic regime on the Arabian passive margin. It is possible that some extensional regime affected the passive margin of the Arabian Plate since the Late Paleozoic to the Late Mesozoic and caused thinning of the lithosphere and hot depleted mantle-plume material was melted to a high degree (Azizi et al. 2013).

The geological prospecting for copper mineralization in Waraz locality, Mawat Igneous complex was performed by group of domestic experts such as Al-Hilali et al. (1991), etc. According to earlier conclusions, Mawat massif was generally considered without economical importance (Bolton 1955). Power (1954) considered copper occurrences unimportant and without economical potential. Smirnov and Nelidov (1962) in Waraz area determined 3.71% of Cu and concluded that mineralization is insignificiants with no commercial concentrations of copper. However, some newer exploration (Al-Hashimi and Al-Mehaidi 1975) reported that copper content which in the mineralized zone reaches up to 54140 ppm Cu (5.4% Cu). Detailed geological investigations in the Waraz locality with the one borehole (240 m deep) allows for recognition of two types of Cu occurrence a) secondary Cu carbonates (malachite) and b) Cu sulfides (chalcopyrite-pyrite) which is probably primary mineralization. Geochemical analysis of borehole samples provided concentrations of copper in span from 11 ppm to 4,910 ppm (average 638 ppm).

As it is prominent from older references, mineral ore potential in this area have been known for a long time, but, remains unexplored due logistical and sometimes political reasons, and due the same reasons, these areas are difficult to map using traditional methods (Othman and Gloaguen 2014). The authors demonstrated the potential of the Support Vector Machine (SVM) algorithm for classifying the lithological units of Mawat ophiolite complex, using Advanced Space-borne Thermal Emission and Reflection radiometer (ASTER) satellite data. The SVM algorithm was specifically used to detect chromite occurrences. The collected samples from fieldwork show corresponded to remote sensing, which has important implications for starting to explore chromite in the ophiolite regions in Iraq using remote sensing tools (Othman and Gloaguen 2014).

Prospectivity of this area was confirmed with more recent papers: Yara and Mohammad (2018) concluded that "Two types of primary mineralization occur in the Mirawa, sulfides which are represent by pyrite and chalcopyrite. The oxides are magnetite and ilmenite. They occur either as aggregates or disseminated and as vein fillings. Two stages of mineralization have been identified according to textural features (synentic and epigenetic). The alteration of this primary phase by supergene solutions forms secondary mineralizations which are represented by covellite, hematite and goethite. Detailed petrographic and microstructure observations reveal that formation of the Mirawa mineralization was related to magmatism and shearing as a result of Eocene crustal extension during the final stages of exhumation of a metamorphic rock complex".

Recent exploration of Mawat Ophiolite complex documented copper sulfides (chalcopyrite, bornite, chalcocite and covellite) in copper-rich deposits (Yassin et al. 2015).

Yara (2019a) summarised knowledge on copper deposits in Mawat region and pointed that copper mineralization underwent different stages of deformation and alteration and distinguished two types of primary mineralization: (1) sulfides, which are represented by pyrite and chalcopyrite, and (2) oxides, represented by magnetite and ilmenite. The mineralization occurs as disseminated and vein filling. The mineral assemblage is chalcopyrite, pyrite, magnetite and ilmenite as primary minerals, whereas covellite, malachite, hematite and goethite are the secondary minerals.

Yara (2019b) confirmed that Cu-mineralization consists of chalcopyrite, pyrite, malachite and azurite, with Cu content between 2.84 and 23%. According to mineral paragenesis in the Kuradawe copper occurrence, using petrographic, geochemical and stable isotopes methods, he concluded that the ore minerals and the host rocks suffered the same metamorphic history. Paragenetic sequence show three stages of mineralization; orthomagmatic, hypogene and supergene. The δ34S data of the sulfide minerals reveal that the source of the mineralized fluids is of granitic composition.

It is important to point that Al-Bassam (2013) referenced to lack of estimation of economic properties of these deposits: Despite the numerous showings of copper mineralization in the Kurdistan Region of NE Iraq, none of which have been investigated in detail to enable accurate assessment of tonnage, grade, mining conditions and upgrading potential. However, in view of the numerous Cu deposits in Cyprus, Turkey, Iran and Oman, which are all related to the Cretaceous ophiolites and are commercially producing copper, it can be anticipated that the potential of discovering commercial Cu deposits in the age-equivalent ophiolite complexes of the Kurdistan Region is encouraging.

Geologic-Tectonically Exploration

Satellite Imagery - Analysis and Interpretation

In this study, Satellite imagery obtained by Tera-ASTER and QuickBird satellites were used in two exploration phases (Oluić et al. 2007; 2008). ASTER image cover wide spectral region with 14 bands and spatial resolution which varies from 15 m, 30 m and 90 m, covers the area of 60 x 60 km. These resolutions were suitable for regional interpretation of the Mawat complex. The images were used to evaluate large areas of terrain for a variety of properties like tectonics, rock discrimination, and geomorphology. QuickBird imagery has higher resolution (1-4 m) and was useful for more detailed analysis of physical landforms such as outcrops or structural features and for location of control and sampling points etc.

ASTER satellite color composite was produced from different spectral channels: 6, 3, 1; **3, 2, 1;** 9, 7, 5 and 3N/3B, in scale 1:25,000, while QuickBird Color composite produced in the scales 1:10,000 and 1:1,000. Color composites in the cartographic projection, were used for orientation, basis for drawing of collected data (GPS), and for tectonic interpretation and rock discrimination (Figure 2).

Figure 2. *ASTER Colour Composite (VNIR & SWIR) of Mawat Ophiolitic Complex: **B**-Basalt, Diabase, Metadiabase; **G**-Gabbro, **N**-Wallash-Naopurdan Nappe, Metagabbro; **P**- Peridotite, Serpentite, **RB**- Mollase - Redbed Series, F-Fold Zone; **Q**- Qulgula*

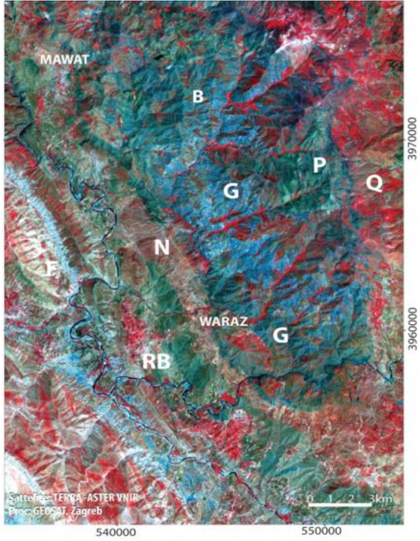

Source: image was recorded in 2003, digital proc. Oluić 2007.

In the NE part of the explored area predominant rocks are basalt and diabases (B), meta gabbro and gabbro (G), peridotites and serpentites (P), and the zone of Mollase-Redbeds unit (RB). In the SW part Mollase-Redbed series dominates, which extends in zonal form around the central part of the terrain. Wallash and Naopurdan Nappe have been thrusted ower Redbed series, which are very intensively disturbed (folded), with many plicative structures (anticlines and synclines). The rocks are intensely ruptured, with numerous faults predominantly NW-SE orientation (Oluić et al. 2008) (Figures 3-5).

Figure 3. *Digital Terrain Model of Mawat-Waraz Area (Satellite ASTER Image Shaded Relief Azimutt=315^o)*

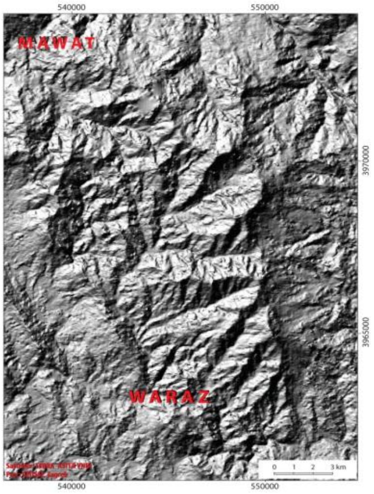

Figure 4. *Linaements in Mawat-Waraz Area Registrered on ASTER Imagery*

Figure 5. *Rose Diagram of Lineaments in Mawat-Waraz Area*

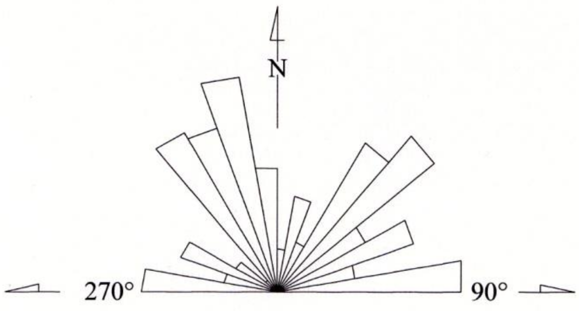

Dominant strikes of faults are NNW-SSE and NE-SW. Streams and deep valleys are predisposed by faults and are located along them (direction NE-SW). The localities on intersections of different fault systems frequently show enrichment in copper mineralization.

Field Work

The field work comprised two phases; first, gathering general information on geology of the explored area, and the second focused on detailed observation on the ore occurrences, their host rocks, mineralization, etc. The field work comprised cruises crosscutting geological units of the Mawat ophiolitic complex to acquire general idea on their mutual relationship with special accent on the position of mineralization. The rock composition is very heterogeneous, and the area is heavily tectonized (Figures 6 and 7). On crosscuts we have observed characteristics of upper Cretaceous Shiranish, Tanjiro, and Agra formations, Redbed series (molasses unit), and Naopurdan-Wallash Formation (melange nappe).

Figure 6. *Redbed Sediments - Intensely Folded, in Front of Zagros Overthrust*

Figure 7. *Bulfat Rock Complex in Forehead of Zagros Owerthrust*

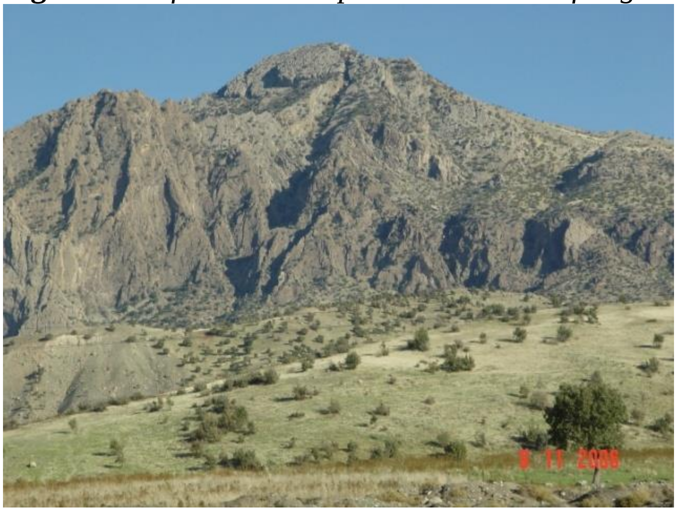

Special attention was given to the Mawat nappe ophiolite rocks including peridotites, serpentinites, gabbros, basaltic rocks and metamorphics rocks of the Gimo sequence. More detailed work was carried out on the three separate areas which were recognized as most promising for copper mineralization.

Detailed Exploration of the Separated Locality

Three localities were identified as potential perspective zones of increased sulfide mineralization, and selected for detailed geological and geophysical explorations. These are Waraz (A), Kanjirin-Kuradawi (B) and Mirawa-Chenara (C) localities (Figure 8).

Figure 8. *ASTER Color Composite of Waraz-Mawat Area and Perspective Localities (A, B, C)*

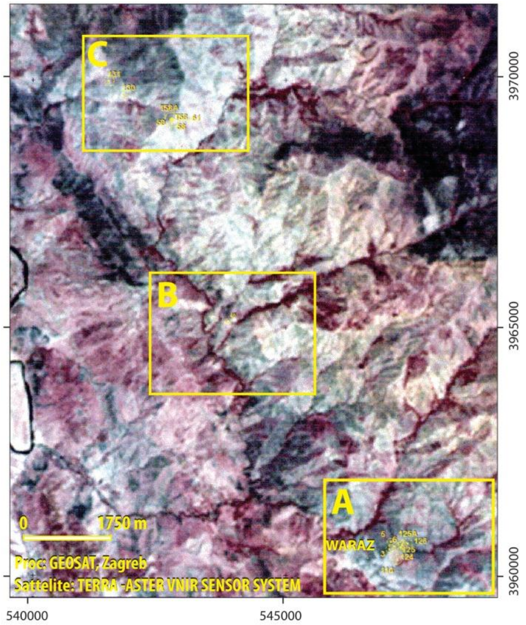

<u>Waraz Area (A)</u>

Waraz area is located in southern part of Mawat ophiolitic massif and has the surface of about 12 km^2 (Figure 8). Based on interpretation of satellite data, geological field reconnaissance and geophysical survey, as well as microscopic and geochemical study, the Geological sketch-map was produced displaying the host rocks, tectonic elements and mineralization zone (Figure 9).

Figure 9. *Geological Sketch-Map of the Waraz Area with Mineralization Zone*

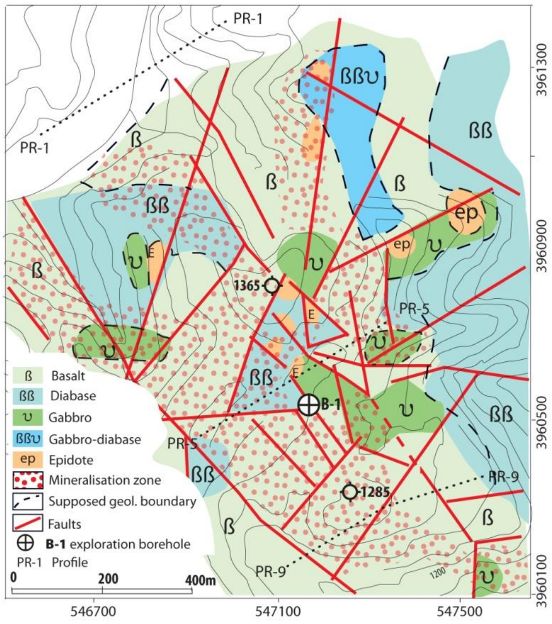

Source: Olujić et al. 2008.

The map illustrates distribution of major rock types (upper pillow lavas, sheeted dykes etc.), and perspective zones of copper mineralization. More dominant rocks are basalts (β) and diabase (ββ), followed by gabbros (Ʊ) which are frequently followed by epidotes veins, isolated in different blocks. The terrain is intensely tectonized and cut by numerous faults in various orientations (Figure 10).

Figure 10. *Rose Diagram of Ruptures in Waraz Area*

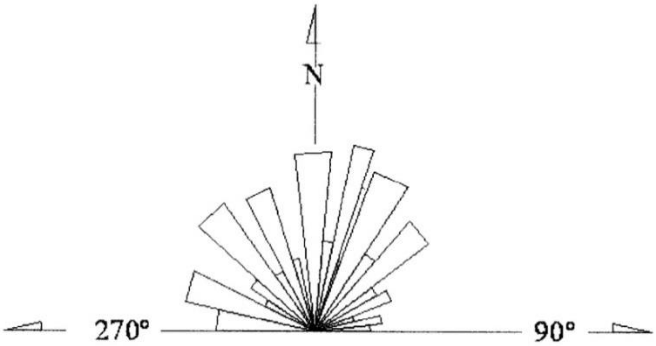

The mineralization zone extends coherently in SE-NW direction in the length of about 1,500 m and about 800 m wide in the central part of explored terrain. Mineralization is mostly located in pillow lavas, basaltic dykes and gabbro-diabase formation (Figure 11).

Figure 11. *Pillow Lava Higly Tectonized Contains Copper Mineralization*

Copper ore crops out as thin horizons, ranging from 10 cm to 50 cm in thickness and between 1 to 5 m in length, distributed within an area of about 0.4 km^2. Mineralization is situated within sheared and fractured zones in the basalts and greenschists, closely associated with acidic rocks and quartz veins. The sheared and fractured zone strikes NW and dips 50-70^o to NE. Mineral association consists of malachite, pyrite, limonite and chalcopyrite. The copper content in mineralized zone varies in very wide ranges from 1.53 to 60,505 ppm.

Primary minerals in the mineralization zone are represented by: chalcopyrite, bournite and pyrite. In the oxidation process from chalcopyrite, malachite and limonite were developed, and from pyrite formed limonite. The rocks were intensely fractured and dissected by numerous epidotic veins. Mineralization is evidenced by limonatization which primarily follows epidotic veins. At places, one may find traces of the secondary copper mineral malachite, originated by weathering of chalcopyrite. The gabbro-diabase formation is crosscut by numerous epidote and, in lesser extent, quartz veins. The intensity of mineralization correlates well with the intensity of epidotisation.

Geophysical survey

Geophysical survey (geoelectric and geomagnetic techniques) were utilized with the aim to identify a) the distribution of lithological units with sulfide mineralization, b) faults and fault zones, and c) the intensity of total magnetic field (*ΔT)*. Geoelectric mapping and sounding was applied for the geophysical/ geoelectric surveys, which included induced polarization (*IP)* techniques electrical resistivity method. The used method in combination with field reconnaissance resulted in data showing sulfide mineralization and its field distribution (Figure 12).

Figure 12. *Induced Polarization (IP) Anomaly and* **ϱa** *Value of Lower and Higher Resistivity (B-1 Borehole)*

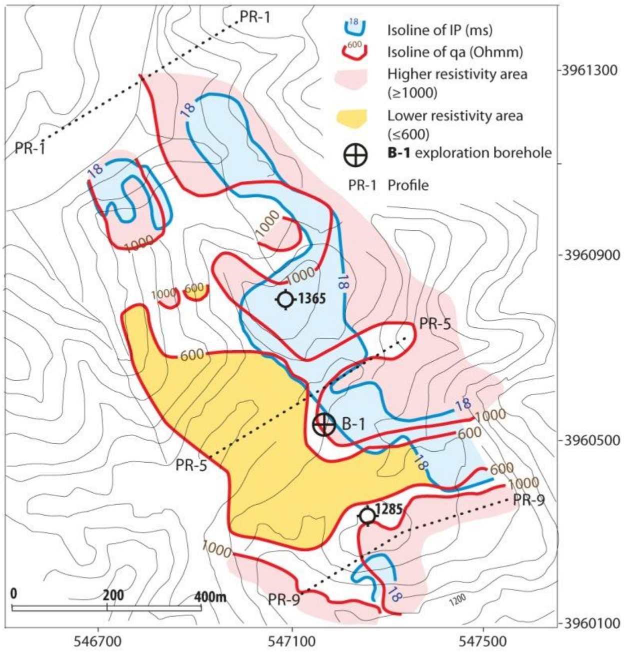

The zones with increased induced polarization-*IP* value are, as a rule, the zones of increased sulfide mineralization, which were registerd almost in all measured profiles, in the area of about 1.5 km^2. The *IP* values showed that the primary sulfides are situated in the compact gabbro-diabase rocks. Larger zones of lower electrical resistence, characteristic for diabase rocks with enrichment of secondary minerals (limonite, malachite with epidots), are located westwards and eastward of the exploration borehole B-1.

The higher *IP* values were registared in the areas with increased mineralization of secundare minerals (limonite and malachite with epidots). The values of gradients self- potentia (*SP)* changed from -25 mV to more than + 45 mV. This data suggest that the increased self-potential *IP* are related to the areas with increased values of *IP* polarization. Decreasing values of *IP* indicate secondary mineralization like in the locality west of borehole B-1. There are registered lower values of eletric resistivity because of increased mineralization.

The anomalies of ΔT changed within bounds from 46,700 to 48,600 that indicate strong magnetic field, because of the presence of basalt and metabasalt with magnetic minerals (e.g., piroxene). The expressive anomalies of ΔT compared with anomalies of *IP* are shown in Figure 13. It is obvious that the orientation of anomaly have NW-SE strike that coincides with tectonic dislocations.

Figure 13. *Waraz Locality: IP Anomaly and Intensity of Total Magnetic Field* $\boldsymbol{\Delta T}$

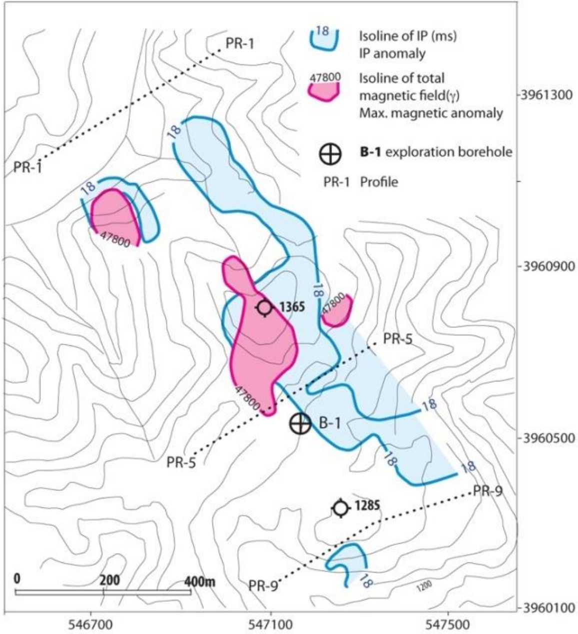

Larger magnetic anomaly in central part of the explored area corresponds with the zone of diabase rocks and secondary minerals – malachite, limonite etc.

Mineralization

The main host rocks of mineralization in Waraz area are pillow lava formation connected with basalt and basalt dykes and epidote veins, that showed *IP* measurement. Pillow lava lithofacies is highly tectonized, along the regional sheared zone. The potential area of ore mineralization has the area of about 3 km^2. The mineralization host rocks are located at the very contact of the gabbro-diabase formation. Gabbro-diabase formation contains primary and secondary mineralization (Figure 14). Locally, pillow lava formation is thrusted over the gabbro-diabase formation or onto the Naopurdan mélange.

Figure 14. *Secondary Copper Mineralization Within Gabbro-Diabase Formation*

The zone can be recognised by limonitization of sulfides, and limonite staining on the rocks and numerous outcrops of secondary copper mineralization with malachites. The source of copper which occurrs in the pillow lava formation has a significent importance. It is recognized by widespread occurrence of secondary minerals (limonite, malachite, azurite) and primary sulfide minerals (chalcopyrite, pyrite, bornite). The gabbro-diabase formation is crosscut by numerous epidote and, in lasser extent, quartz veins. The intensity of mineralization correlates well with the intensity of epidotization. Massive limonite were formed stainings on the basalt after oxidation of massive vein sulfide-malachite (Figure 15).

Figure 15. *Samples of Secondary Copper Minerals (Malachite)*

Geochemical analysis of representative rock samples taken *in situ* showed that the samples have increased Cu and some increased values of Au, Ti, and Fe (Table 1). The other elements Cr, Ni, As, Mo, Ag, Rb, Bi, and Zn contain lesser concentracions.

Table 1. *Contents of Au, Ti, Fe and Cu in the Analysed Samples (10,000 ppm=1% Cu). (Eurotest Control, Sofia, 2007)*

Nr	Sample No	Au (ppm)	Ti (ppm)	Fe (%)	Cu (ppm)
1	W-206	<0.05	2,452	5.63	4,226
2	W-111	<0.05	1,362	2.71	1.53
3	W-53	<0.27	677	8.89	60,705
4	W-23	<0.05	949	3.51	174
5	W-22	<0.05	695	1.34	35
6	W-77	<0.05	1,587	4.46	621
7	W-30	<0.05	613	4.41	8,073

The Rare Earth Elements (REE) were also analysed (16 elements), and (TR) 51 elements, but the concentration of the elements have not increased values.

Konjirin-Kuradawi Area (B)

This area is situated in central part of the Mawat ophiolitic complex, and covers the area of about 6 km^2 (Figure 8). The area is primarily composed of the gabbro-diabase formation. Gabbro-diabase formation are cut by epidote and quartz veins, which contain limonite and malachite (Figure 16). The Konjirin area contains basaltoids of the pillow lava formation and a sheet dyke complex. At the contact with the mélange it obtained a wide range of textures from the pegmatitic gabbro, micro- and medium crystalline leucocratic and melanocratic gabbro, and at places achieved doleritic and diabase texture. The dominating types of the rocks in the study area are: diabase, gabbro, plagiogranite and epidotic veins.

Figure 16. *Mineralization Zone of Gabbro-Diabase Rocks with Epidote and Quartz Veines*

Tectonics in this area was very active and the rocks are very dissured and disarrangement. Specially stressed is the fault zone, NW-SE strike which is cut by numerous transverse faults (Figure 17).

Figure 17. *Rose Diagram of Ruptures in Konjirin Kuradawi Area*

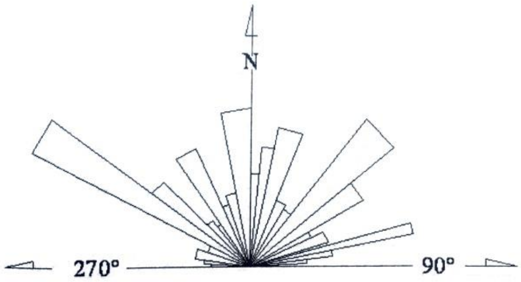

At the same time the localities with increased mineralization and limonatisation have been registered. In the diabase-gabbroid rocks were registered Fe-Cu ore effusive cataclastite enriched with iron and copper minerals, which at the surface create limonite and malachite coatings. Flasered metadiabase (altered into greenshist metamorphic facies) have been determined by microscopic analyse (Figure 18).

Figure 18. *Thin-Section of Flasered Metadiabase in Konjirin Area (P32x. N^+)*

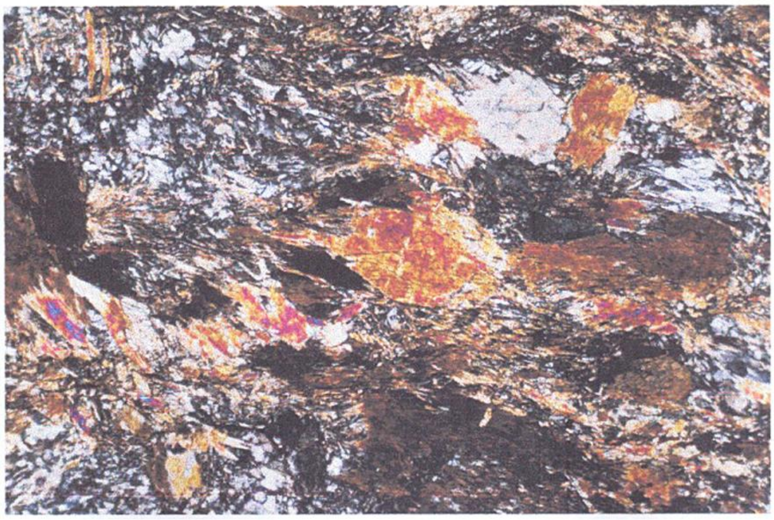

Geophysical survey

The map of induced polarization has values of *IP* between 2 msec and 34 msec. Zones with higher values of *IP*, with higher sulfide mineralization, are determined only on geoelectric profile measured in a creek, probably in a fault zone. On the map of apparent resistivity (ϱa) values of ϱa are in span between less then 600 Ohmm up to more than 2,800 Ohmm. The zones of higher mineralization *IP* are probably located on the contact of lower- and higher electrical resistivities and they are also coused by faults.

The map of self potential *SP* shows values of *SP* in range from -32 mV to over +28 mV. The values of *SP* also changed polarity on the contact zones.

The map of total magnetic intensity field (*ΔT)* shows values of *ΔT* in the span of 46,200Ý up to 49,800Ý. Higher values of total magnetic field *ΔT* are detected on the north and northwest parts of the exploration area, partly on the same place where induced polarization *IP* is also high. Based on measurement data, it could be concluded that anomaly zone *IP* of smaller dimension is situated on the intersection of larger dislocations with NE-SW and NW-SE strike. The zones of lower and higher resistivity generally corrrespond to existeing NW-SE dislocations.

Mineralization

The mineralized zone generally stretches from SE to NW, and is the best develloped in central part of the terrain. The main bearer of the mineralization are pillow lavas, connected with basaltic rocks and basaltic dykes, as well as with well developed epidote-quartz, closely associated with leucocratic rocks, supposingly plagiogranite. A wide zone of alteration has been recorded on the southern border of the Konjirin exploration area (Figure 19).

Figure 19. *Alteration Zone with a Few Meters Thick Mineralization*

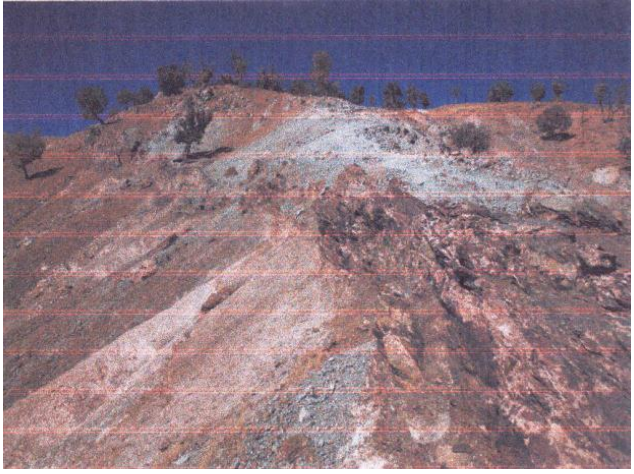

A fairly large number of geochemical analysis have been done, but here are presented only some of them (Table 2).

Table 2. *The Contents of Some Analysed Sampels: Au, Ti, Fe, Cu (Eurotest Control, Sofia, 2007)*

Nr	Sample No	Au (ppm)	Ti (ppm)	Fe (%)	Cu (ppm)
1	K-108	1.10	529	8.15	36.287
2	K-7A	0.10	3,261	7.12	16.430
3	K-6A	0.12	3,118	7.68	21.648
4	K-91	<0.05	896	4.50	217
5	K-4A	0.05	97	2.66	2,324
6	K-62	<0.05	269	3.69	94
7	K-20	<0.05	787	3.90	68
8	K-303D	0.05	268	5.51	1,354
9	K-16	<0.05	290	2.26	446
10	K-82D	0.05	1,683	2.44	3,652

It is obvious that the copper value have significantly increased Cu concentration in relation to others values.

Mirava – Chenaran Area (C)

Mirava-Chenaran area is situated in northern part of the Waraz-Mawat ophiolitic complex, and covers about 9 km^2 (Figure 8). Dominant rocks are gabbro with metagabbro, then basalts with metabasalts, metatuff/effusive and quartz-metaeffusives (Figure 20).

Figure 20. *Thin-Section of Actinolite Shist with Iron Minerals (Actinolite, Acidie Plagioclase, Quartz-Epidote, Chlorite), the Rock is Rich with Magnetite and Pyrite (P32x. N$^+$)*

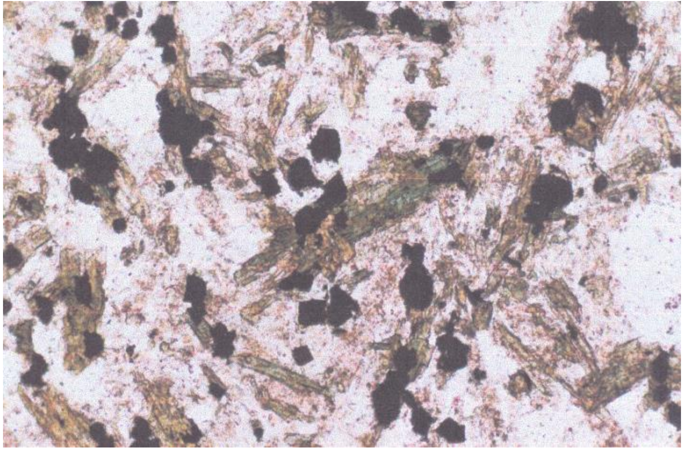

Diabase was found in central part of the area, and in places metadiabase is located more often along tectonic dislocations. Locally, plagiogranite was determined which can be gold bearer rocks. Epidote rocks are located in eastern and northwestern part of the area, more often connected to gabbro and diabase. These rocks often comprise increased mineralization especially of secondary minerals. Epidotic mineralized veins are connected to tectonic ruptures, and they are good indication of the mineralization. Tectonic activity in this area was very intensive, in particular radial tectonic, one can observe two general directions of faults: NW-SE, known as Zagros trend and NE-SW (Figure 21).

Figure 21. *Rose Diagram of Ruptures in Mirava-Chenaran Area*

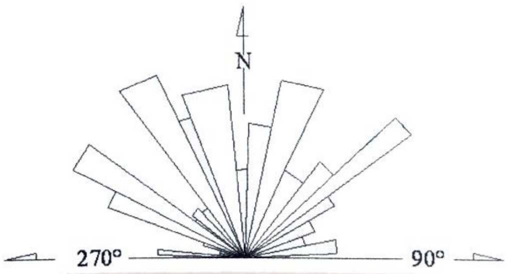

Geophysical survey

The same geophysical techniques have been used like in the studied areas A and B. Two *IP* smaller anomalies (15-70 msec) were registered in the zones of increased electric resistivity ϱa which have been caused by gabbro and basalte rocks, that indicate increased sulfide mineralization Figure 22).

Figure 22. *Induced Polarization (IP) Anomalies and ϱa Value of Lower and Higher Resistivity*

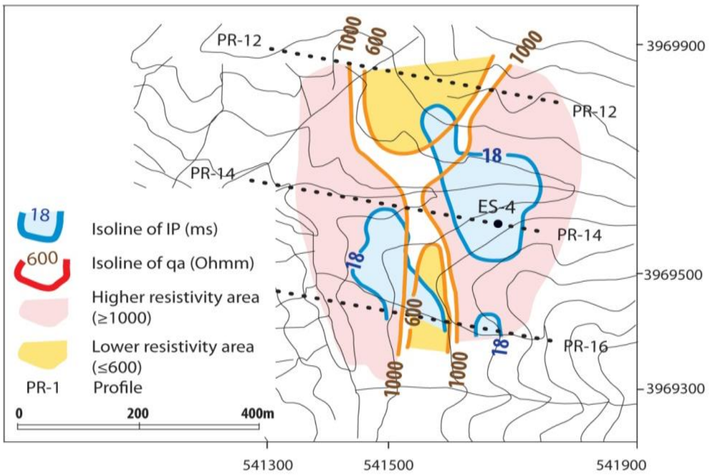

The zones of lower electric resistivity can be related to the occurence of epidote, and that coincide with tectonic dislocations of NW-SE strike.

Mineralization

The main bearer of mineralization in this area is pillow lava formation connected to basalts and basalt dykes. Mineralization is connected with well developed epidote-quartz, closely associated with leucocratic rocks, supposingly plagiogranite.

The outcrops with rich mineralization occur along the roadcut near the village of Mirava and Chenaran. It consists of highly limonitized gabbro and diabase dykes with occurences of secondary and primary copper mineralization (Figure 23).

Figure 23. *Gabbro-Diabase Formation with Epidote-Quartz Veins and Copper Mineralization (Close to the Road to Mirava)*

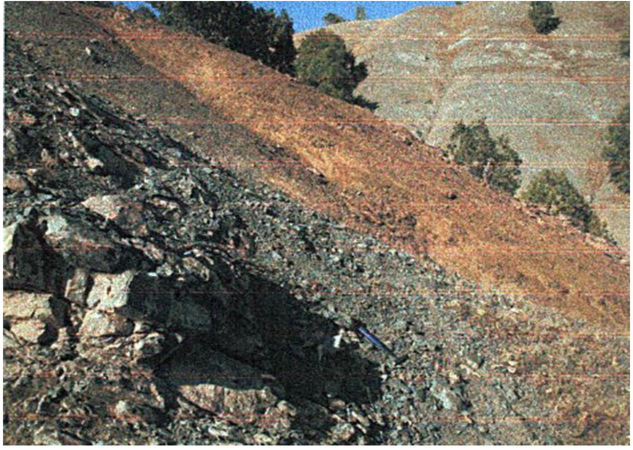

The rocks are intensely fractured and dissected by several generations of veins. The first system consists of epidote veins, ranging in size from several cm to 0.5m. The epidote veins are cut by quartz veins. Mineralization consists of secondary copper minerals, malachite and iron oxides. The whole rock unit was intruded by diabase dykes and sills, up to 1 m thick. Mineralization is closely related to the epidote-quartz veining (Figure 24).

Figure 24. *Diabase Dykes Intruded and Tectonically Displaced in the Gabbro Rocks*

The *Chenaran locality* is characterised by a wide limonitizatin zone, which follows general strikes of the rock formations, mostly built of gabbro-diabase. Its intensity increases toward the Chenaran Village, where epidote-quartz ore veins are exposed, with malachite, limonite and primary sulfide minerals. The locality is mostly composed of gabbro-diabase rocks, which incorporate significante masses of plagiogranites (Figure 25).

Figure 25. *Copper Mineralization: Primary Mineralization: Bornite, Chalcopyrite and Pyrite, and Secondari: Malachite and Limonite, (Near Chenaran Village)*

Primary mineralization zone it is evident in the Mirava village locality too, in gabbro-diabase formation, which incorporates significante masses of plagiogranites (Figure 26).

Figure 26. *Mineralization Zone in Gabbro-Diabase with Plagiogranites in the Mirava Village Locality*

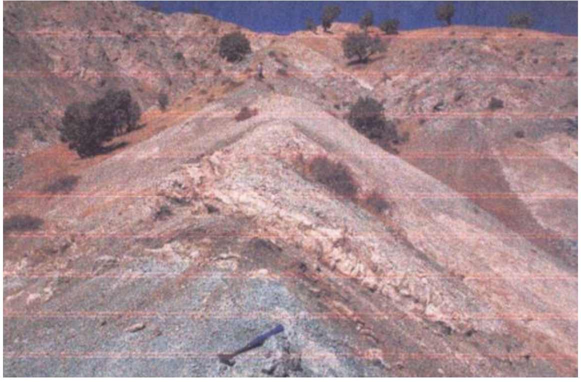

The Mirava locality is build of basalt-diabase formation with variable contribution of diabase, epidote-quartz veinis, gabbro pegmatites, and several zones of plagiogranites which are closely associated with mineralization. The mineralization is recognized in many outcrops in the area which extends from Mirava village to the contact with the Naopurdan formation. The plagiogranites contain 2.5g/t gold. The area of mineralization is very large, approximates 10 km^2.

The clear signs of the primary mineralization are weathering products of sulfide: limonite, malachite, and chalcocite. Primary mineralization, consisting of bornite, chalcopyrite and pyrite (Figure 27) underwent replacement within the cementation zone, by chalcocite. The secondary mineralization is dominated by massive limonite and brown stainings of limonite (e.g., goetite) over the surfice surrounding host rocks. With decreased weathering, oxidizing zone turned sulfides into malachite and limonite, with rare relics of the chalcocite (Figure 28).

Figure 27. *Copper Minerals: Chalcopyrite, Bornite, Pyrite and Malachite and Limonite in the Epidote-Quartz Veins*

Figure 28. *Copper Mineralization - Highly Weathered Rock, with Malachite and Limonite*

The mineralization zone can be followed generaly from SE to NW and is the best developed in the central part of the study area. The southeastern boundary of the mineralization is not constrained; a possible extension of the mineralization zone extends toward Waraz. Mineralization terminates on the north above the Kuradawi village too.

Geochemical analysis has been done on 17 elements and gold. The contents of gold in analysed samples is low (<0.05-0.22 ppm) and the contents in other elements is insignificant. Here are presented only Au, Ti, Fe, and Cu (Table 3).

Table 3. *The Content of Au, Ti, Fe and Cu in the Analysed Samples (Eurotest Control, Sofia, 2007)*

Nr	Sample No	Au (ppm)	Ti (ppm)	Fe (%)	Cu (ppm)
1	M-62	<0.05	1,257	4.05	919
2	M-224	<0.05	1,881	10.56	286
3	M-267	<0.05	2,320	5.46	232
4	M-63	<0.05	1037	6.86	135
5	M-217D	<0.05	2,065	3.17	478
6	M-246	0.22	1,428	3.89	5,875
7	M-204	0.05	993	6.26	16,803
8	M-266	<0.05	2,948	2.71	4,378

Conclusions

Geological exploration of copper mineralization was in the area of Mawat ophiolitic massif. Satellite *ASTER* and *QuickBird* images were used together with field prospection and geophysical survey, as well as petrographic and chemical analyses. The explored terrain is mostly composed of ultrabasic and basic rocks (peridotite, gabbros, serpentites, basalts, etc.). The rocks are intensely tectonised and intruded by numerous basic magmatic bodies. The host rocks of the mineralization are primarily gabbros and metagabbros intersected by diabase dykes, epidotic and quartz veins, covered by pillow lava formations. Copper mineralization is usually stained with limonite crust which is a good indicator of mineralization. Primary mineralization is represented by chalcopyrite, bournite and pyrite, while secondary mineralization malachite and limonite is a product of weathering.

In the study area, three smaller perspective areas were selected: *Waraz, Konjirin-Kuradawi* and Mirava-Chenaraan, which have copper mineralization. The registered concentration of copper varies highly, in wide range. The concentrations of Cu in samples are: Waraz area 1.53-60,705, Konjirin-Kuradawi 68-36,287 and Mirava-Chenaran 135-16,803 ppm. Maximum value of Cu was determined in the Waraz area 6.7% Cu. In some rock samples gold concentration of 0.36 and 2.59 ppm were also determined.

Based on the collected information, the possible perspective of the mineralization bearing rocks has been roughly estimated. Farther action in selected localities detailed explorations as well as drilling is recommendable in order to precisely define economic properties of this area.

Acknowledgments

Authors are very grateful to ECOINA Co, Zagreb, Croatia which supported this exploration. We also thank our colleague geologists: P. Buva, D. Milovanović, L. Palinkaš, and geophysicists: V. Samolov, M. Pandurov and M. Divljaković who worked with us in field exploration. Our sincere thanks goes to the Kurdish colleagues who assisted in this exploration. We also thank our colleague D. Koželj for his useful consultation. Our acknowledge get also to the Eurotest-Contral PLC Laboratory, Sofia- Bulgaria for ore elements and gold analysis, as well as to Croatian Geological Survey for micropetrographic analysis of samples.

References

Al-Bassam KS (2013) Mineral resources of Kurdistan Region, Iraq. Iraqi Bulletin of Geology and Mining 9(3): 102–127.

Al-Hashimi RA, Al-Mehaidi MH (1975) Cu, Cr dispersion in Mawat ophiolite complex, NE Iraq. *Journal of the Geological Society of Iraq* (special issue): 37–47.

Al-Hilali HAM et al. (1991) *Geological prospecting for copper mineralization in Waraz locality, Mawat igneous complex*. Baghdad, Iraq: Ministry of Industry and Minerals State Establishment of Geological Survey and Mining-Directorate of Geological Survey.

Al-Mehaidi (1974) Simplified geological map of Mawat Ophiolites Complex NE Iraq. *Journal of the Geological Society of Iraq* (special issue): 37–44.

Azizi H, Hadi A, Asahara Y, Mohammad YO (2013) Geochemistry and geodynamics of the Mawat mafic complex in the Zagros Suture zone, northeast Iraq. *European Journal of Geosciences* 5(4): 523–537.

Bolton CMG (1955) *Report on the geology and economic prospects of Qaladiza area site invest.* Co. Ltd. Report no. 32. Baghdad, Iraq: D.G. Geological Survey and Mineral Investigation Library.

Hamasalh RF (1982) *Petrochemistry, petrogenesis and tectonic setting of the Pauza ultramafic rocks-bulfat complex North-East Iraq, Kurdistan Region*. Master Thesis. Mosul, Iraq: University of Mosul.

Hassan MM, Brian G, Jones BG, Buckman S, Jubory IA, Ismail SA (2015) Source area and tectonic provenance of Paleocene–Eocene red bed clastics from the Kurdistan area NE Iraq: bulk-rock geochemistry constraints. *Journal of African Earth Sciences* 109(Sep): 68–86.

Ismail A, Sarmad A, Nutman AP, Bennet VC, Jones BG (2017) The Pushtashan juvenile suprasubduction zone assemblage of Kurdistan (northeastern Iraq): a Cretaceous (Cenomanian) NeoTethys missing link. *Geoscience Frontiers* 8(5): 1073–1087.

Jassim SZ (1975) Geology of the central sector of the Mawat igneous rocks, Northeastern Iraq. *Journal of the Geological Society of Iraq* 6: 83–92.

Moghadam HS, Stern RJ (2011) Geodynamic evolution of Upper Cretaceous Zagros ophiolites: formation of oceanic lithosphere above a nascent subduction zone. *Geological Magazine* 148(5–6): 762–801.

Oluić M, Palinkaš L, Milovanović D, Vasiljević R, Buva P (2007) *Report on mineral exploration in Mawat Ophiolitic Massif, Kurdistan – Iraq (first exploration phase)*. Zagreb, Croatia: ECOINA. (Unpublished)

Oluić M, Palinkaš L, Milovanović D, Vasiljević R, Buva P, Romandić S, et al. (2008) *Report on mineral exploration in Mawat Ophiolitic Massif, Kurdistan – Iraq (second exploration phase)*. Zagreb, Croatia: ECOINA. (Unpublished)

Othman AA, Gloaguen R (2014) Improving lithological mapping by SVM classification of spectral and morphological features: the discovery of a new chromite body in the Mawat ophiolite complex (Kurdistan, NE Iraq). *Remote Sensing* 6(8): 6867–6896.

Power GL (1954) *Iraq mineral survey project, volume 3, six monthly report*. GSM Lib. No. 264.

Smirnov VA, Nelidov VP (1962) *Report on 1/200,000, prospecting correlation of the Sulaymanya-Choarta-penjwin area carried out in 1961*. GSM Lib. No. 290.

Yara IOM, Mohammad YO (2018) Iron-copper mineralization associated with metagabbro in Mirawa Village, Kurdistan region, northeastern Iraq. *Journal of Zankoy Sulaimani* 20 – 2 (Part-A).

Yara IOM (2019a) Copper mineralization in selected areas of Kurdistan Region, Iraq: a review on mineralogy and geochemistry. Iraqi Bulletin of Geology and Mining (special issue 8): 41–63.

Yara IOM (2019b) Mineralogy and stable sulfur isotopes of the sulfide mineralization in the Kuradawe Area, Mawat Ophiolite, Kurdistan Region, Northeastern Iraq. *Iraqi Bulletin of Geology and Mining* 16(1): 63–77.

Yassin T, Alabidi AJ,Hussain ML, Al-Ansari N, Knutsson S (2015) Copper ores in Mawat ophiolite complex (Part of ZSZ) NE Iraq. *Natural Resources* 6(10): 514–526.

Athens Journal of Sciences- Volume 8, Issue 4, December 2021 – Pages 273-308

Numerical Analysis of Boundary Layer Flow and Heat Transfer over a Stretching and Non-Stretching Bullet-Shaped Object

By Mohammed Ali[*] *& Md. Abdul Alim*[±]

The two-dimensional axisymmetric magnetohydrodynamic boundary layer flow with heat transfer of Newtonian fluid over a stretching and non-stretching bullet-shaped object has been investigated. Therefore, fluid flow and heat transfer have been investigated in two types of flow geometries such as the thicker surface $(s \geq 2)$ *and the thinner surface* $(0 < s < 2)$ *of the bullet-shaped object. The present analysis also focuses on the physical relevance and accurate trends of the boundary layer profiles which are adequate in the laminar boundary layer flow. The novelty of this current work is to discuss the effect of shape and size (surface thickness parameter s) and the stretching factor of the bullet-shaped object on the fluid velocity and temperature profiles within the boundary layer region also develop the relationship between the dependent and independent parameters by the correlation coefficient. The partial differential equations of momentum and energy have been reduced to a system of non-linear ordinary differential equations along with the transformed boundary conditions by applying the local similarity transformations. These coupled non-linear ordinary differential equations' governing the flow field has been solved by the Spectral Quasi-Linearization Method (SQLM). The numerical analysis of the SQLM has been carried out with MATLAB for investigating the effect of various controlling parameters on the flow fields. The residual error infinity norms have been analyzed to determine the speed of convergence and accuracy of the method. The numerical results have been displayed graphically and in tabular form and the physical behavior of the problem also discussed. The investigation shows that in the case of a thicker bullet-shaped object* $(s \geq 2)$ *the velocity profile does not approach the ambient condition asymptotically but intersects the axis with a steep angle and the boundary layer structure has no definite shape whereas in the case of a thinner bullet-shaped object* $(0 < s < 2)$ *the velocity profile converge the ambient condition asymptotically and the boundary layer structure has a definite shape. It is also noticed that thinner bullet-shaped object acts as good cooling conductor compared to thicker bullet-shaped object and the wall friction can be reduced much when thinner bullet-shaped object* $(0 < s < 2)$ *is used rather than the thicker bullet-shaped object* $(s \geq 2)$ *in both types of non-stretching or stretching bullet-shaped object* $(\varepsilon = \text{or} > 0)$.

Keywords: *forced convection, correlation coefficient, multiple regression, MHD, stretching*

---

[*] Associate Professor, Department of Mathematics, Chittagong University of Engineering & Technology, Bangladesh.

[±] Professor, Department of Mathematics, Bangladesh University of Engineering & Technology, Bangladesh.

Introduction

A systematic and detailed review of studies done in the past related to the present problem is under study. This helps us to understand the problems with its historical background, current status, and scope of application. The review of literature provides a synthesis of many documents and articles. The main purpose of the review is to summarize the related fields of interest coming from different mediums. The review helps us that how important the topic is and summarized the article for all that relates to the topic is essential. When an external flow past along objects it encompasses a variety of fluid mechanics phenomena. The nature of the flow field depends on the shape of the object. Even the simplest shaped objects, like a plate, may produce rather complex flows. Therefore, the flow pattern and related forces depend strongly on various parameters such as size, orientation, speed, and fluid properties. Therefore, the present problem will be helpful for designing bullet-shaped objects like Rocket, Missile, Aero plane, Bullet Train and Submarine, etc.

Due to the high applicability of this problem in such industrial phenomena, a large number of theoretical investigations are observed with different effects of physical parameters that have been presented during the last decades. Abo-Eldahab and Salem (2004) studied the boundary layer flow of non-Newtonian fluid and energy transfer over a power-law stretching surface with heat flux and observed that thermal boundary layer thickness reduces for the increasing values of mixed convection parameter but the reverse trend arises due to viscous dissipation, as a result, the energy transfer enhances. Aftab et al. (2018) analyzed the boundary layer power-law fluid flow over a moving permeable flat plate with viscous dissipation and heat generation. Ahmad et al. (2002) studied the mixed convection boundary layer flow by using the SQLM. This study concluded that the SQLM is suitable than another method. Later Ahmad et al. (2001) performed Bellman QLM for Neumann problems. Ajala et al. (2019) analyzed the boundary layer flow and energy transfer by the effect of the magnetic field, variable viscosity, and thermal radiation. Ajaykumar and Srinivasa (2020) studied the effect of variable viscosity on unsteady Magneto Hydrodynamics (MHD) laminar boundary layer flow with heat transfer over a stretching surface. Alarifi et al. (2019) discussed the influence of the sink or source on MHD boundary layer flow with heat transfer over a vertical stretching surface. Asaithambi (1998) discussed the Falkner – Skan equation by applying the finite difference method and found a similar solution. Ashwini and Eswara (2012) discussed that the boundary layer separation is delayed due to magnetic field parameter and the dual solutions are arises in case of decelerating flow regime. Ashwini and Eswara (2015) performed the unsteady MHD decelerating boundary layer wedge flow with heat generation. Awaludin et al. (2018) developed the stability model of MHD boundary layer flow over a stretching wedge. Daba et al. (2015) studied the mixed convection BL flow and heat transfer with convective boundary conditions over a vertical stretching surface. Marneni and Ashraf (2015) observed that the momentum and thermal boundary layer thicknesses decrease with the increase of Eckert number in the presence of suction and heat absorption when the wedge stretches slower than the free stream flow, Ashwini and Eswara (2015) discussed that the dual solutions exist in forced convection decelerating flow regime and the magnetic field stabilizes the flow which in turn delays the boundary layer separation from the wedge surface, Kandasamy and Mohammad (2015) investigated theoretically the impact of a convective surface on the heat transfer characteristics of water-based nanofluids over a static or moving wedge in the presence of magnetic field with variable stream condition and show that the temperature distribution in a nanofluid in the presence of thermal radiation with magnetic influenced by the convection parameter. Alam et al. (2016) studied numerically the effects of variable fluid properties and thermophoresis on unsteady forced convective boundary layer flow along with a permeable stretching/shrinking wedge. The results show that the Prandtl number, as well as the Schmidt number, varies significantly within the boundary layer for the flow with variable thermal conductivity and viscosity, Falana et al. (2016) studied the influence of Brownian motion and thermophoresis on a nonlinearly permeable stretching sheet in a nanofluid and found that the temperature rises for Brownian motion, thermophoresis and stretching ratio, Mabood et al. (2016) has been carried out to examine the effects of volume fraction of nanoparticles, suction/injection, and convective heat and mass transfer parameters on MHD stagnation point flow of water-based nanofluids and found that the friction factor and heat and mass transfer rates increase with magnetic field and suction/injection parameters. Nageeb et al. (2017) investigated the effects of thermal radiation, soret, and dufour parameters on mixed convection and nanofluid flow over a stretching sheet in the presence of a magnetic field. Mustaqim et al. (2018) studied the problem of the steady two-dimensional stagnation-point flow of heat and mass transfer over a shrinking sheet with the effect of radiation and velocity slip. Dual solutions are obtained. Therefore, they established a stability analysis that determines which solution is linearly stable and physically realizable. Kumar and Krishnan (2018) studied the axisymmetric boundary layer axial flow over a circular cylinder by using integral analysis. The analytical results are applicable to discuss the different flow regimes of axisymmetric boundary layers in the presence of pressure gradients. Aftab et al. (2018) investigated the combined effects of the thermal radiation, viscous dissipation, suction/injection, and internal heat generation/absorption on the boundary layer flow of a non-Newtonian power-law fluid over a semi-infinite permeable moving flat plate in parallel or reversely to a free stream. It was observed that the dual solutions exist when the flat plate and the free stream move in opposite directions. The velocity and temperature distributions are plotted and discussed for various values of the emerging physical parameters. Salleh et al. (2019) analyzed the steady boundary layer flow of a nanofluid past a thin needle under the influences of heat generation and chemical reaction. It is observed that the multiple (dual) solutions are likely to exist when the needle moves against the direction of the fluid flow. Therefore, the reduction in needle thickness provides the enlargement of the region of the dual solutions. The stable solution has been done by using a stability analysis. The obtained results indicate that the upper branch solutions are linearly stable, while the lower branch solutions are linearly unstable. The study also revealed that the rate of heat transfer is a decreasing function of heat generation parameter, while the rate of mass transfer is an increasing function of heat generation and chemical reaction parameters. Ibrahim and Tulu (2019) numerically inspected a steady laminar flow over a vertical stretching sheet with the existence of viscous dissipation, heat source/sink, and magnetic fields through a shooting scheme based Runge-Kutta-Fehlberg-integration algorithm. Findings reveal that the Nusselt number at the sheet surface augments, since the Hartmann number, stretching velocity ratio, and Hartmann number increase. Nevertheless, it reduces with respect to the heat generation/absorption coefficient. Jabeen et al. (2020) analyzed the MHD boundary layer flow over a nonlinear stretching sheet in a porous medium using semi-analytical approaches and proved that the flow field is effectively appreciable by injection and suction. Megahed et al. (2021) studied the effects of the extended heat flux and variable fluid properties on the unsteady laminar MHD flow and heat transfer over a stretching sheet. Irfan et al. (2020) discussed the effects of unsteady MHD stagnation point flow of heat and mass transfer across a stretching/shrinking surface in a porous medium with internal heat generation/absorption, thermal radiation, and chemical reaction. Muthukumaran and Bathrinathan (2020) studied the analytical solution of mixed convection boundary layer flows with suction, injection (blowing) and viscous dissipation over a vertical stretching sheet near the stagnation point. Shateyi and Muzara (2020) discussed the boundary layer nanofluid flow over a Non-Linearly Stretching surface with the effects of viscous dissipation and chemical reaction..

The above discussion and review of the literature show that the mentioned works are restricted only for the case of flow around a flat plate, cone, wedge or cylindrical shape geometry with some physical conditions but to the best of author's knowledge, no published work has been found on boundary layer flow over a bullet-shaped geometry.

The main purpose of this problem is to investigate the MHD axisymmetric boundary layer flow and heat transfer over stretching and non-stretching bullet-shaped object with internal heat generation parameter. Also analyzed the relationship between the physical parameters and flow profiles by applying the correlation coefficient and multiple regressions. Motivated by the previous studies, the present problem tries to fill the existing gaps in the field of boundary layer theory. The innovation of this present problem lies in the unification of more physical parameters into the governing equations and an attempt to give a thorough analysis of how the flow properties are affected by these parameters. Also, the novelty of the current paper lies in the application of the recently developed numerical method to solve these highly nonlinear equations.

So the purpose of the present work is to study the effect of various parameters such as magnetic effect, stretching factor, heat generation, size and shape of the surface on momentum and thermal behavior of the fluid, skin friction coefficient, rate of heat transfer, nature of solutions within the boundary layer over a bullet-shaped object by using a spectral quasi-linearization iterative scheme.

Mathematical Model and Similarity Analysis

Let us consider the steady two-dimensional MHD laminar boundary layer flow of an incompressible, electrically conducting, and viscous Newtonian fluid over a stretching bullet-shaped surface in a bulk fluid at a constant temperature T_∞. A schematic representation of the physical model and coordinate system as shown in Figure 1. It is assumed that the free stream and the stretching velocities are U_∞ and U_w respectively, x is the coordinate measured along the bullet-shaped surface, r is the coordinate measured in the radial directions respectively.

Figure 1. *Flow Geometry and Coordinate System*

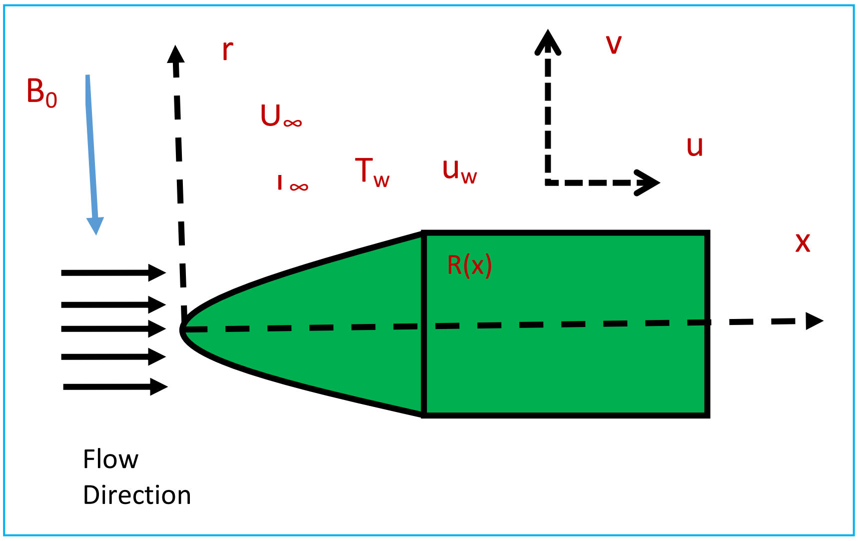

We assumed that the temperature of the surface is T_w, where $T_w > T_\infty$ corresponds to a heated surface (assisting flow) and $T_w < T_\infty$ corresponds to a cooled surface (opposing flow). The surface has an isothermal surface, and kept at temperatures T_w such that the temperature differences within the flow are sufficiently small. The small magnitude of the temperature difference allows expression of the Taylor series expansion about the free stream temperature T_∞ as a linear function of temperature at any interior point within the flow region. The magnetic field B_0 is imposed perpendicular to the direction of the flow and the induced magnetic field can be neglected due to the smallest magnetic Reynolds number. The surface moves with a velocity $U_w(x)$, in the same or opposite direction of the free stream velocity $U_\infty(x)$. It is also assumed that the external electric field is zero and the electric field due to polarization of charges is negligible. The velocity of the surface $U_w(x)$, the free stream velocity $U_\infty(x)$ and the temperature of the surface T_w are respectively defined as $U_w(x) = ax^m, U_\infty(x) = bx^m, T_w(x) = x^{2m-1}$, where a and b$(b > 0)$ are the stretching rate of the sheet and straining rate parameters respectively with $a > 0$ for stretching case and $a < 0$ for the shrinking case. Also, m is the power-law index parameter of velocity and temperature. It may be noted that the constant b is proportional to the free stream velocity far away from the surface. An axial pressure gradient is imposed inside the boundary layer due to variable axial free-stream.

Therefore, the governing partial differential equations of continuity, momentum and thermal energy are as follows

Equation of continuity:

$$\frac{\partial}{\partial x}(ru)+\frac{\partial}{\partial r}(rv)=0$$

(1)

Momentum equation:

$$\mathrm{u}\frac{\partial \mathrm{u}}{\partial \mathrm{x}}+\mathrm{v}\frac{\partial \mathrm{u}}{\partial r}=\mathrm{U}\frac{\mathrm{dU}}{\mathrm{dx}}+\frac{\nu}{r}\left(\frac{\partial \mathrm{u}}{\partial \mathrm{r}}+r\frac{\partial^2 \mathrm{u}}{\partial \mathrm{r}^2}\right)+\frac{\sigma \mathrm{B_0}^2}{\rho}(\mathrm{U}-\mathrm{u})$$

$$where\ -\frac{1}{\rho}\frac{\partial p}{\partial x}=\mathrm{U}(x)\frac{\mathrm{dU}(x)}{\mathrm{dx}}$$

(2)

Energy equation:

$$\mathrm{u}\frac{\partial \mathrm{T}}{\partial \mathrm{x}}+\mathrm{v}\frac{\partial \mathrm{T}}{\partial \mathrm{r}}=\frac{\alpha}{r}\left(\frac{\partial T}{\partial r}+r\frac{\partial^2 \mathrm{T}}{\partial \mathrm{r}^2}\right)+\frac{Q}{\rho C_p}(T-T_\infty) \tag{3}$$

The above equations are subject to the following boundary conditions

$$\begin{aligned}&u=U_w(x),\ v=0,\ T=T_w\ \ at\ \ r=R(x)\ and\\&u\to U_\infty(x)=U, T\to T_\infty, as\ \ r\to\infty\end{aligned} \tag{4}$$

where R(x) prescribes the surface shape and size of the axisymmetric body, u and v are the velocity components along with the axial and radial directions (x,r) respectively, ν is the kinematic viscosity of the fluid, ρ is the density of the fluid, the term $\frac{\sigma B_0^2}{\rho}u$ describes the x component of the magnetic field where $\frac{\sigma B_0^2}{\rho}$ is the magnetic parameter which is the ratio of the electromagnetic force to the inertial force, B_0 is the magnetic field intensity, α is the thermal diffusivity of the fluid and T is the fluid temperature respectively. The magnetic field usually applied in the y direction normal to the boundary layer flow. The flow is in x-direction whose velocity component is u. Thus J × B, representing Lorentz force becomes $-\frac{\sigma B_0^2}{\rho}u$. The negative sign in the term is because of retardation. The first term on the right-hand side of equation (2) refers to the pressure gradient in the stream wise direction, as calculated from the Euler's equation for inviscid fluid.

To obtain the similarity solutions for the system of equation (1) – equation (3) subject to the boundary conditions (4), we use the following axisymmetric similarity transformation as:

$$\eta = \frac{Ur^2}{\nu x},\ \ \psi = \nu x f\left(\eta\right), T = x^{2m-1}\theta\left(\eta\right) \qquad (5)$$

where ψ is the stream function and is defined by the velocity components $u = \frac{1}{r}\frac{\partial \psi}{\partial r}$ and $v = -\frac{1}{r}\frac{\partial \psi}{\partial x}$, η is the similarity variable, U_w is the surface velocity and U_∞ is the free stream velocity. The expression η gives the shape and size of the body, when we put η = s in the expression $\eta = \frac{Ur^2}{\nu x}$, we get the dimensionless radius $R\left(x\right) = \sqrt{\frac{\nu s x^{1-m}}{a+b}}$.

The continuity equation (1) is identically satisfied by the equation (5) and the equations (2) and (3) are transformed into non-dimensional, nonlinear and coupled ordinary differential equations by applying the similarity transformation as

$$\eta f''' + f'' + \frac{1}{2} f f'' + \frac{m}{8}\left(1 - 4f'^2\right) + \frac{M}{8}\left(1 - 2f'\right) = 0 \qquad (6)$$

$$\eta\theta'' + \frac{1}{2}\theta' + \frac{1}{2}\Pr\left[f\ \theta' - \left(2m-1\right) f'\ \theta\right] + \frac{1}{4}\Pr Q^{*}\theta = 0 \qquad (7)$$

and the transformed boundary conditions are

$$\begin{aligned} &f\left(\eta\right) = 0,\ f'\left(\eta\right) = \frac{\varepsilon}{2}, \theta\left(\eta\right) = 1,\ at\ \eta = s,\ and \\ &f'\left(\eta\right) \to \frac{1}{2}, \theta\left(\eta\right) \to 0\ \ as\ \eta \to \infty \end{aligned} \qquad (8)$$

Where prime denotes differentiation with respect to η, $\varepsilon = \frac{U_w}{U_\infty}$ is the velocity ratio parameter between the surface and the composite velocity. It is mentioned here that the velocity ratio parameter $\varepsilon > 1$ means that the surface stretches faster than that of the free stream flow and $\varepsilon < 1$ means that the surface slower than that of the free stream flow. Here, $\varepsilon > 0$ is for stretching and $\varepsilon < 0$ is for shrinking. On the other hand, ε = 0 and ε = 1 correspond to a fixed surface in a moving fluid (Blasius flow) and a moving surface in a quiescent fluid (Sakiadis flow), respectively. The range $0 < \varepsilon < 1$ indicates that the surface and the fluid move in the same direction. If $\varepsilon < 0$ the free stream is directed towards the positive x - direction, while the surface moves towards the negative x-direction. When $\varepsilon > 1$, the free stream is directed towards the negative x-direction, while the surface moves towards the positive x-direction. However, the present analysis has performed only for the case $\varepsilon \leq 2$.

The dimensionless parameters M is the magnetic parameter, m is the power-law index parameter, ε is the stretching parameter Pr is the Prandtl number, and Q* is the heat generation parameter which is defined as

$$\mathrm{M} = \frac{\sigma \mathrm{B}_0^2 \mathrm{x}}{2\rho \mathrm{U}}, \varepsilon = \frac{\mathrm{U}_w}{\mathrm{U}}, \ \mathrm{Pr} = \frac{\nu}{\alpha}, Q^* = \frac{Qx}{\rho U_w c_p}$$

In practical applications, two quantities of physical interest are to be determined, such as surface shear stress and the rate of heat transfer at the surface. These may be obtained in terms of the local skin-friction coefficient C_f and the local Nusselt number, Nu_x. The skin friction and Nusselt number are the dimensionless shear stress at the surface and dimensionless heat flux at the surface respectively and can be expressed as the following way.

We have the shear stress at the surface $\tau_w = \mu \left(\frac{\partial u}{\partial r} \right)_{r=0}$ and the local skin friction coefficient $C_f = \frac{2\tau_w}{\rho U^2}$

By applying the equations (4) and (5), we obtain the local skin friction coefficient

$$C_f = \frac{\mu}{\rho U^2} \left(\frac{\partial u}{\partial r} \right)_{r=0} = 4\sqrt{\frac{\eta}{\mathrm{Re}_x}} f''(\eta) \Rightarrow C_f \sqrt{\mathrm{Re}_x} = 4\sqrt{\eta} f''(\eta)$$

The local Nusselt number for the convective boundary condition is defined as $Nu_x = \frac{xq_w}{\kappa (T_w - T_\infty)}$. Where q_w is the wall heat flux and can be defined as $q_w = -\kappa \left(\frac{\partial T}{\partial r} \right)_{r=0}$.

By using the equations (4) and (5), we obtain the local Nusselt number $Nu_x (\mathrm{Re}_x)^{-1/2} = -2\sqrt{\eta} \theta'(\eta)$

Procedure of Numerical Solution

Bellman and Kalaba (1965) were the first to apply the QLM about half a century ago to solve nonlinear ordinary and partial differential equations. Since the differential equation is highly non-linear and it is almost impossible to find the closed-form analytic solution. The SQLM (2020) is a combination of two methods: (i) the Quasi-linearization method (QLM) and (ii) the Chebyshev spectral collocation method. The QLM is the generalization of Newton–Raphson-based method and is used to linearize the non-linear ODEs into linear ODEs. The QLM approaches that the difference between the approximate solution at the present iteration and the previous iteration is very small. The numerical simulation of the present problem is obtained with the help of SQLM which gives highly accurate results. Since the similarity variable converges to $\eta \to \infty$ but the present simulation has been performed for a finite domain of η. Therefore, the dimensionless velocity and energy distribution within the boundary layer asymptotically tends to a free stream velocity that satisfies the boundary conditions. The numerical solution for the above equations for various values of magnetic parameter M, power-law index parameter m, the thickness of the surface s, stretching ratio ε and Prandtl number Pr are analyzed using the quasi-linearization technique. Applying SQLM, the system of equations (6) and (7) are converted into the following iterative sequence of linear differential equations.

$$\mathrm{a}_{0,\mathrm{t}} f'''_{\mathrm{t}+1}(\eta) + \mathrm{a}_{1,\mathrm{t}} f''_{\mathrm{t}+1}(\eta) + \mathrm{a}_{2,\mathrm{t}} f'_{\mathrm{t}+1}(\eta) + \mathrm{a}_{3,\mathrm{t}} f_{\mathrm{t}+1}(\eta) = R_{1,\mathrm{t}}(\eta) \qquad (9)$$

$$\mathrm{b}_{0,\mathrm{t}}\theta''_{t+1}(\eta) + \mathrm{b}_{1,\mathrm{t}}\theta'_{t+1}(\eta) + \mathrm{b}_{2,\mathrm{t}}\theta(\eta) + \mathrm{b}_{3,\mathrm{t}} f'_{t+1}(\eta) + \mathrm{b}_{4,\mathrm{t}} f_{t+1}(\eta) = R_{2,t}(\eta) \qquad (10)$$

The subscripts *t* and *t + 1* denote previous and current approximations.
The transformed boundary conditions are

$$f_{t+1}(xN_x) = 0,\ f_{t+1}(xN_{x-1}) = \frac{\varepsilon}{2}, \theta_{\mathrm{t}+1}(xN_x) = 1, \text{ at } \eta = 0$$

$$f_{t+1}(x_0) = 0,\ f_{t+1}(x_0) = \frac{1}{2}, \theta_{\mathrm{t}+1}(x_0) = 0, \text{ as } \eta \to \infty$$

The variable coefficients obtained from the previous iteration are given by

$$a_{0,t} = \frac{\partial f}{\partial f'''} = \eta, a_{1,t} = \frac{\partial f}{\partial f''} = \frac{1}{2} + \frac{1}{2} f_t, a_{2,t} = \frac{\partial f}{\partial f'} = -mf_t' - \frac{M}{4}, a_{3,t} = \frac{\partial f}{\partial f} = \frac{1}{2} f_t''$$

$$b_{0,t} = \frac{\partial \theta}{\partial \theta''} = \eta, b_{1,t} = \frac{\partial \theta}{\partial \theta'} = \frac{1}{2} + \frac{\Pr}{2} f_t, b_{2,t} = \frac{\partial \theta}{\partial \theta} = \frac{1}{4} \Pr Q^* - \frac{\Pr(2m-1)}{2} f_t'$$

$$b_{3,t} = \frac{\partial \theta}{\partial f'} = -\frac{\Pr(2m-1)}{2}\theta_t, b_{4,t} = \frac{\partial \theta}{\partial f} = \frac{\Pr}{2}\theta_t'$$

$$R_{1,t}(\eta) = a_{0,t} f_t''' + a_{1,t} f_t'' + a_{2,t} f_t' + a_{3,t} f_t - F\left[\eta, f(\eta), f'(\eta), f''(\eta)\ldots\ldots f^n(\eta)\right]$$

$$= \frac{1}{2} f_t f'' - \frac{m}{2} f_t^2 - \frac{m}{8} - \frac{M}{8}$$

$$R_{2,t}(\eta) = b_{0,t}\theta_t'' + b_{1,t}\theta_t' + b_{2,t}\theta_t + b_{3,t} f_t' + b_{4,t} f_t$$

$$-F\left[\eta, f(\eta), f'(\eta), f''(\eta)\ldots\ldots f^n(\eta)\right] = \frac{\Pr}{2}\left[f_t\theta_t' - (2m-1) f_t'\theta_t \right]$$

The linear differential equations (9) and (10) are solved iteratively by using the Chebyshev spectral collocation method (CSCM). The linear transformation

$x=\frac{2\eta}{L_\infty}-1$ is used to convert the domain [0, ∞) into the computational domain [−1, 1]. The unknown functions f_{r+1} and θ_{r+1} are determined with the help of CSCM, and Chebyshev interpolating polynomials. The derivatives of the functions f_{r+1} and θ_{r+1} at the Gauss–Lobatto collocation points are

$$x_i=\cos\left(\frac{\pi i}{N}\right), i=0,1,2,\ldots.N \text{ gives } \frac{d^n f_{t+1}\left(x_i\right)}{dx}=\sum_{k=0}^{N_1} D_{ik}^n f_{t+1}\left(x_k\right)=D^n F \quad (11)$$

Where, $D=\frac{L_\infty}{2}\mathrm{k}$, k is (N_1 + 1) × (N_1 + 1) differentiation matrix and $F=\left[f_{t+1}\left(x_0\right), f_{t+1}\left(x_1\right), f_{t+1}\left(x_2\right),\ldots.f_{t+1}\left(x_{N-1}\right), f_{t+1}\left(x_N\right)\right]^T$. Similarly, the nth derivatives of θ_{t+1} are given by

$$\frac{d^n\theta_{t+1}\left(x_i\right)}{dx}=\sum_{k=0}^{N_1} D_{ik}^n\theta_{t+1}\left(x_k\right)=D^n\Theta \quad (12)$$

By applying the Equations (11) and (12), the Equations (9) and (10) yields

$$\begin{bmatrix} A_{11} & A_{12} \\ A_{21} & A_{22} \end{bmatrix}\begin{bmatrix} F_{t+1} \\ \Theta_{t+1} \end{bmatrix}=\begin{bmatrix} R_{1,t} \\ R_{2,t} \end{bmatrix}, \text{Where}$$

$$A_{11}=a_{0,t}D^3+a_{1,t}D^2+a_{2,t}D+a_{3,t}, A_{12}=0I,$$

$$A_{21}=b_{3,t}D^2+b_{4,t}, A_{22}=b_{0,r}D^2+b_{1,t}D+b_{2,t}$$

The matrix **I** is of order (N_1 + 1) × (N_1 + 1).

Results and Discussion

The non-linear ODEs of the present problem are solved by applying SQLM. The convergence criteria of the solution are performed by the use of solution-based errors. These errors are defined by the differences between approximate solutions at the previous and current iteration levels *t* and *t* + 1, respectively. The error norms are defined as:

$$Error_f=\max_{0\le i\le N}\left\|F_{t+1,i}-F_{t,i}\right\| \text{ and } Error_\theta=\max_{0\le i\le N}\left\|\theta_{t+1,i}-\theta_{t,i}\right\|$$

The infinity norms of the residual errors are defined by

$$\left\|\mathrm{Re}\,s(f)\right\|_\infty=\left\|\eta f'''+f''+\frac{1}{2}ff''+\frac{m}{8}\left(1-4f'^2\right)+\frac{M}{8}\left(1-2f'\right)\right\| \text{ and}$$

$$\left\|\mathrm{Re}\, s(\theta)\right\|_\infty = \left\|\eta\theta'' + \frac{1}{2}\theta' + \frac{1}{2}\mathrm{Pr}\left[\, f\ \theta' \text{-} (2m-1)\ f'\ \theta + \frac{1}{2}Q^*\theta \right]\right\|$$

The impact of physical parameters on velocity $f'(\eta)$, temperature $\theta(\eta)$, skin friction, and the local Nusselt number is shown graphically. The numerical values of skin friction ($C_f\sqrt{\mathrm{Re}_x}$) and Nusselt number ($Nu_x\left(\sqrt{\mathrm{Re}_x}\right)^{-1}$) which are equivalent to velocity gradient $f''(\eta)$ and temperature gradient $\theta'(\eta)$ have been shown in Tables 1 and Table 2 respectively. The computations are done by taking N = 50 collocation points and solution-based errors are defined for the convergence of the numerical method. Again, Figures 16a and 16b show the error infinity norms and residual error infinity norms against iterations. Figure 16(a) represents the convergence for the present problem with iterations. From this, it is noticed that the error infinity norm decreases with the increasing number of iterations that confirm the convergence of the present method. So, it is observed that the present method converges after five iterations. On the other hand, Figure 16(b) assure the accuracy of the present method of less than 10^{-8} and 10^{-14} for $f(\eta)$ and $\theta(\eta)$ against after fourth iterations. It is seen that the residual error decreases with increasing the iterations. This proves the validity of the present method. The errors show that the SQLM is accurate giving errors of less than 10^{-8} within the fourth iteration. In this chapter the default parameters are taken as $M = 1.0$, $m = 1.0$, Pr = 0.71, ϵ = 0.0, 2.0 and s = 0.05, 2.0 throughout the calculation. The fluid velocity profile and skin friction have been depicted graphically versus boundary layer co-ordinate (η) in Figures 2-6 for the increasing effect of the controlling parameters such as magnetic (M), power-law index (m), stretching ratio (ϵ), and surface thickness (s) in the following sub-section. The numerical calculations have been carried out for a wide range of values of the mentioned parameters; $\mathrm{M}(1.0 \le \mathrm{M} \le 10.0)$, $\mathrm{m}(0.0 \le \mathrm{m} \le 3.0), \varepsilon(0.0 \le \varepsilon \le 2.0)$, $s(0.05 \le s \le 2.0)$, $\mathrm{Pr}(0.71 \le \mathrm{Pr} \le 7.0)$.

Velocity Profiles and Skin Friction Coefficient

Figure 2a and Figure 2b represent the influence of magnetic parameter on viscous fluid velocity profile for thinner (s = 0.05) and thicker surfaces (s = 2.0) when $\varepsilon < 1$, ϵ = 1.0 and $\varepsilon > 1$ respectively. It is noticed from these figures that the variation of the stretching ratio parameter has a significant effect on the velocity profile in connection with the magnetic parameter. These plots depict that the velocity profile of the viscous fluid and boundary layer thickness affected significantly with increasing magnetic parameters. From these figures, it is seen that the velocity profile of the viscous fluid and boundary layer thickness squeezes when $\varepsilon > 1$ and the fluid flow form an inverted boundary layer pattern but in the case of $\varepsilon < 1$, the reverse trend occurs in velocity profile both of the thinner and thicker surfaces of the bullet-shaped object. This happens because in presence of the term $\frac{\sigma B_0^{\ 2}}{\rho}(U_\infty - u)$ in equation (2) which is the combination of pressure force ($\frac{\sigma B_0^{\ 2}}{\rho}U_\infty$) and Lorentz force ($\frac{\sigma B_0^{\ 2}}{\rho}u$) terms.

Figure 2. *Effect of Magnetic Parameter (M) on Velocity Profile Taking (a) s = 0.05 and ϵ = 0.0 (Lower Panel), ϵ =1.0 (Separation Line), ϵ = 2.0 (Upper Panel), and (b) s = 2.0 and ϵ = 0.0 (Lower Panel), ϵ =1.0 (Separation Line), ϵ = 2.0 (Upper Panel)*

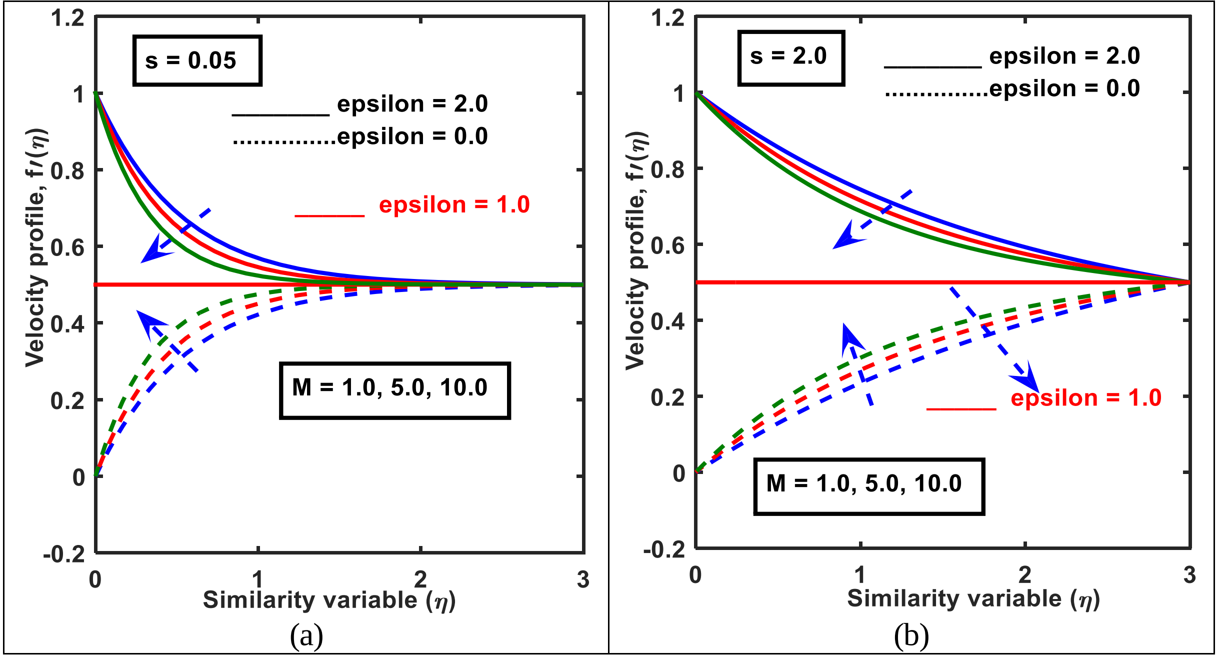

(a) (b)

The velocity profile squeezes when Lorentz's force is greater than the pressure force and vice-versa. Again, it is also seen that the surface velocity and the free stream velocity are equal in the case of ϵ = 1.0. It is also observed that, if the surface thickness parameter (*s*) reduces then the fluid flow form a certain boundary layer structure and the fluid velocity satisfies the far-field boundary condition. On the other hand, while surface thickness parameter (*s*) increases then the fluid flow does not satisfy the far-field boundary condition and the boundary layer structure has no definite shape. Therefore, the velocity boundary layer thickness is higher in the case of a thicker bullet-shaped object (*s* = 2.0) than the thinner bullet-shaped object (*s* = 0.05).

Figures 3a and 3b display the skin friction coefficient for the effect of the magnetic parameter (*M*) with stretching ratio parameter $\varepsilon < 1$ and $\varepsilon > 1$, and the surface thickness parameter *s* = 0.05, *s* = 1.0, respectively. From these figures, it is observed that the skin friction coefficient enhances in the case of $\varepsilon < 1$ but reduces while $\varepsilon > 1$ for both of the thinner and thicker surfaces of the bullet-shaped object. It is observed that the skin friction coefficient is inversely proportional to the dimensionless velocity gradient. The velocity gradient at the surface is positive when $\varepsilon < 1$ and negative due to $\varepsilon > 1$ but zero while ϵ = 1.0 for all values of the controlling parameters. The positive values of the velocity gradient indicate that the fluid applies a drag force on the bullet-shaped object, on the other hand, the bullet-shaped object exerts a drag force on the fluid flow while the velocity gradient is negative.

Figure 3. *Effect of Magnetic Parameter (M) on Skin Friction Coefficient Taking (a) s = 0.05 and ϵ = 0.0 (Upper Panel), ϵ = 2.0 (Lower Panel), and (b) s = 2.0 and ϵ = 0.0 (Upper Panel), ϵ = 2.0 (Lower Panel)*

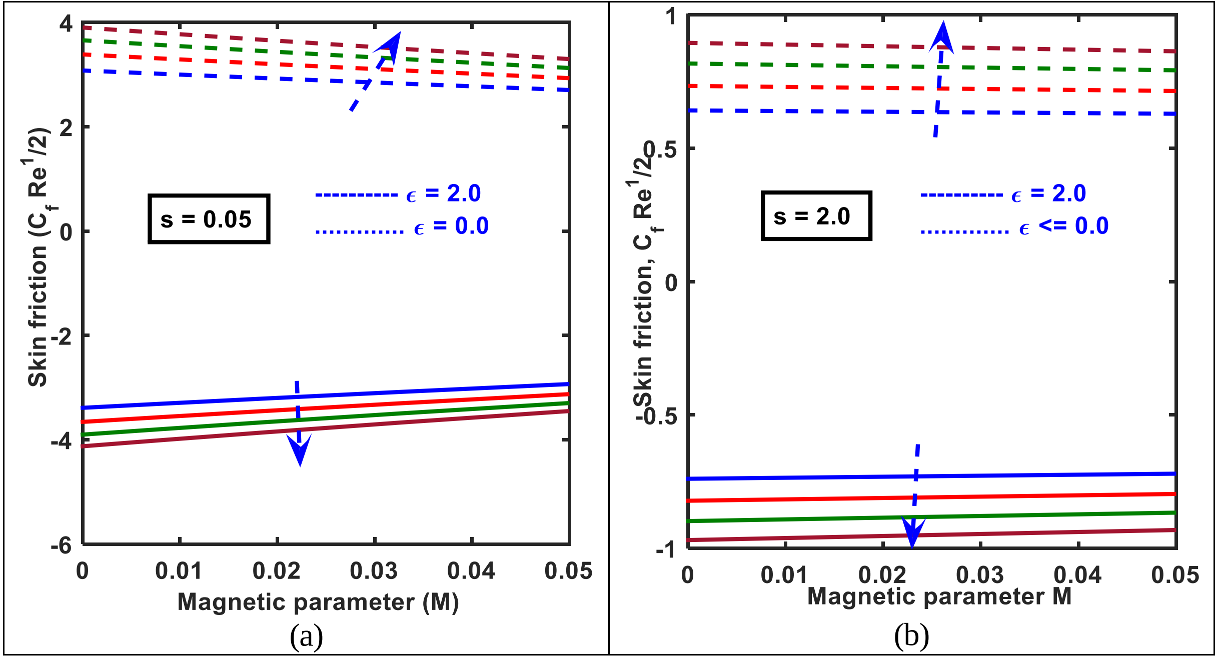

(a) (b)

Therefore, the parameter *M* is directly proportional to skin friction in the case of $\varepsilon < 1$ but inversely proportional when $\varepsilon > 1$. It is observed from Table 1 that, when *M* changes from 1.0 to 10.0 for *s* = 0.05 and ϵ = 0.0, the skin friction decreases 25.5 % whereas for *s* = 0.05 and ϵ = 2.0 the skin friction increases 22.13%. Hence, the skin friction is higher for the non-stretching surface ($\varepsilon = 0$) than the stretching surface ($\varepsilon > 0$).

Figures 4a and 4b show the variation of a velocity profile for the effect of power-law index parameter when the stretching ratio parameter $\varepsilon < 1$ and $\varepsilon > 1$, and the surface thickness parameter *s* = 0.05, *s* = 2.0, respectively.

Figure 4. *Influence of Power-Law Index Parameter (m) on Velocity Profile Taking (a) s = 0.05 and ϵ = 0.0 (Lower Panel), ϵ =1.0 (Separation Line), ϵ = 2.0 (Upper Panel), and (b) s = 2.0 and ϵ = 0.0 (Lower Panel), ϵ =1.0 (Separation Line), ϵ = 2.0 (Upper Panel)*

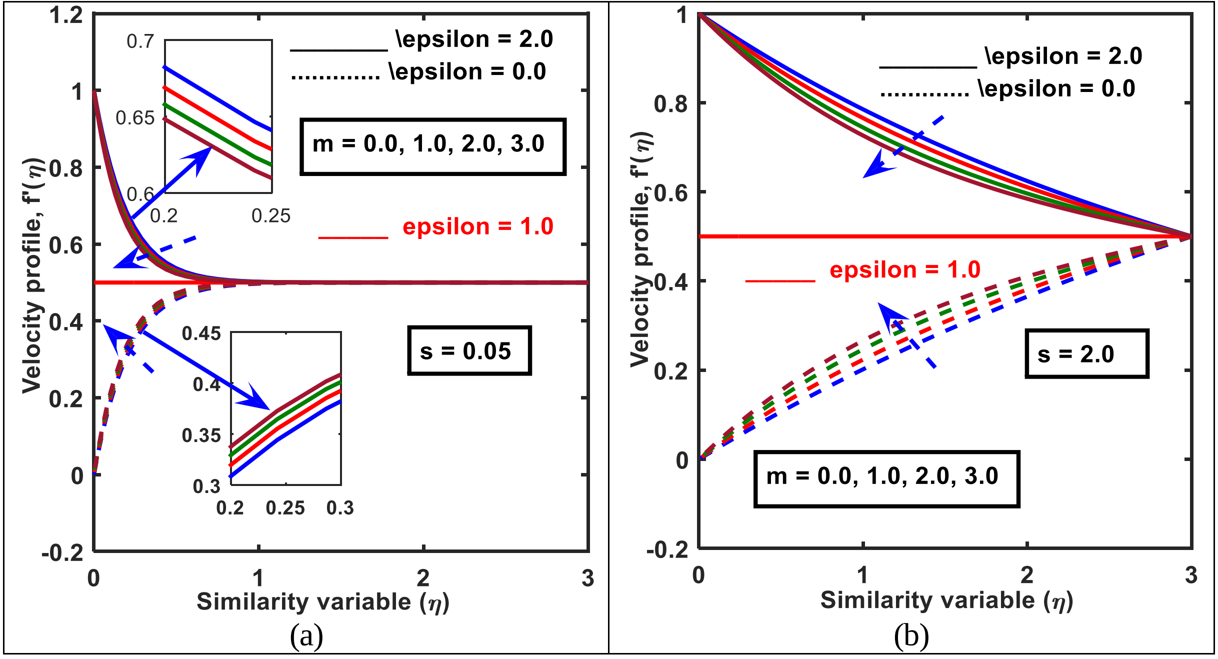

(a) (b)

These plots represent that the velocity profile of the viscous fluid and boundary layer thickness affected insignificantly with an increasing power-law index parameter due to thinner surface (*s* = 0.05) whereas the reverse trend happens in the case of thicker surface (*s* = 2.0). From these figures, it is noticed that the velocity profile and boundary layer thickness squeezes when $\varepsilon > 1$ and the fluid flow form an inverted boundary layer pattern whereas, in the case of $\varepsilon < 1$, the velocity profile expands but boundary layer thickness squeezes the and fluid flow form a certain boundary layer pattern. It is also observed that the velocity profile and boundary layer thickness satisfy the far-field boundary condition in the case of a thinner surface (*s* = 0.05). On the other hand, due to the thicker surface (*s* = 2.0), the velocity profile, and boundary layer thickness are not in parabolic shapes, so this is insignificant with the physical behavior of the boundary layer concept because in this case, the boundary condition does not satisfy. Therefore, the velocity boundary layer thickness is higher in the case of a thicker bullet-shaped object (*s* = 2.0) than a thinner bullet-shaped object (*s* = 0.05).

Figure 5a and 5b display the skin friction coefficient for the effect of power-law index parameter (*m*) by taking the stretching ratio parameter $\varepsilon < 1$ and $\varepsilon > 1$, and the surface thickness parameter *s* = 0.05, *s* = 1.0, respectively. From these figures, it is seen that the skin friction coefficient enhances in the case of $\varepsilon < 1$ but reduces while $\varepsilon > 1$ for both of the thinner and thicker surfaces.

Figure 5. *Effect of Power-Law Index Parameter (m) on Skin Friction Coefficient Taking (a) s = 0.05 and ϵ = 0.0 (Lower Panel), ϵ = 2.0 (Upper Panel), and (b) s = 2.0 and ϵ = 0.0 (Lower Panel), ϵ = 2.0 (Upper Panel)*

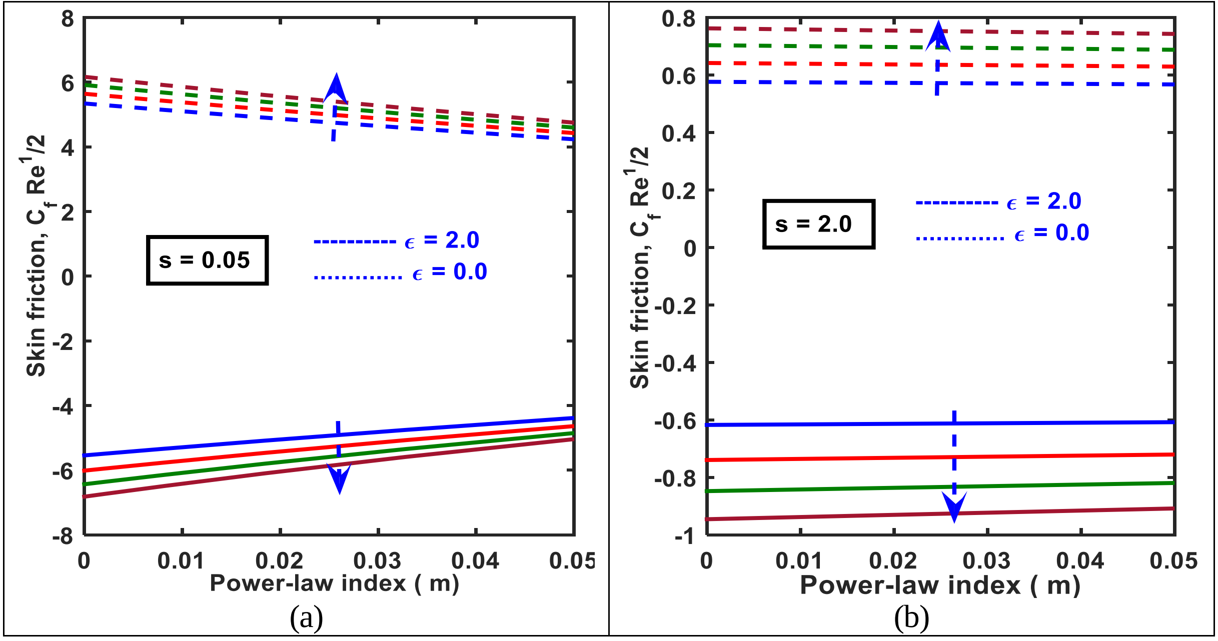

(a) (b)

These graphs also show that the velocity gradient at the surface is a positive when $\varepsilon < 1$ and negative while $\varepsilon > 1$ but zero while ϵ = 1.0 for all values of the controlling parameters. Therefore, the positive values $f''(\eta)$ indicate that the fluid applies a drag force on the bullet-shaped object and the negative value indicates the bullet-shaped object exerts a drag force on the fluid flow. It is observed from Table 1 that, when *m* changes from 0.0 to 2.0 for *s* = 0.05 and ϵ = 0.0, the skin friction decreases 10.73 % whereas for *s* = 0.05 and ϵ = 2.0 the skin friction increases 16.1%.

Figures 6a and 6b illustrate the effects of surface thickness parameter (*s*) $(0.05 \le s \le 2.0)$ on the velocity distribution and skin friction coefficient when the other parameters are fixed by considering the stretching ratio parameter $\varepsilon < 1$ and $\varepsilon > 1$, and the surface thickness parameter *s* = 0.05, *s* = 2.0, respectively. These plots show that the velocity profile of the viscous fluid and boundary layer thickness affected significantly with increasing surface thickness parameters. From Figure 6(a) it is seen that the velocity profile and boundary layer thickness expands when $\varepsilon > 1$ and the fluid flow form an inverted boundary layer pattern but in the case of $\varepsilon < 1$ the velocity profile squeezes but velocity boundary layer thickness increases and the fluid flow forms a definite boundary layer pattern. This happens because the increase in shape and size of the bullet-shaped object enhances the surface area of the object that provides more resistance against the fluid motion as a result the fluid velocity decreases. Therefore, the velocity boundary layer thickness is higher in the case of a thicker bullet-shaped object (*s* = 2.0) than the thinner bullet-shaped object (*s* = 0.05). From Figure 6(b), it is noticed that the skin friction coefficient reduces in the case of $\varepsilon < 1$ but increases while $\varepsilon > 1$ for both of the thinner and thicker surfaces. Hence, the parameter *s* is inversely proportional to $C_f\sqrt{\mathrm{Re}_x}$ in the case of $\varepsilon < 1$ but directly proportional when $\varepsilon > 1$. This graph also shows that the velocity gradient at the surface is a positive when $\varepsilon < 1$ and negative while $\varepsilon > 1$ but zero while ϵ = 1.0 for all values of the controlling parameters. Therefore, the fluid applies a drag force on the bullet-shaped object for the positive values $f''(\eta)$ while the bullet-shaped object exerts a drag force on the fluid flow for the negative values $f''(\eta)$. It is observed from Table 1 that, when *s* changes from 0.05 to 0.3 for ϵ = 0.0, the skin friction increases 76.5 % whereas for ϵ = 2.0 the skin friction decreases 75.2%. Hence, the skin friction is higher for ϵ = 0.0 than ϵ = 2.0.

Figure 6. *Effect of Surface Thickness Parameter (s) on (a) Velocity Profile for ϵ = 0.0 (Lower Panel), 1.0 (Separation Line), 2.0 (Upper Panel), and (b) Skin Friction for ϵ = 0.0 (Lower Panel), 2.0 (Upper Panel)*

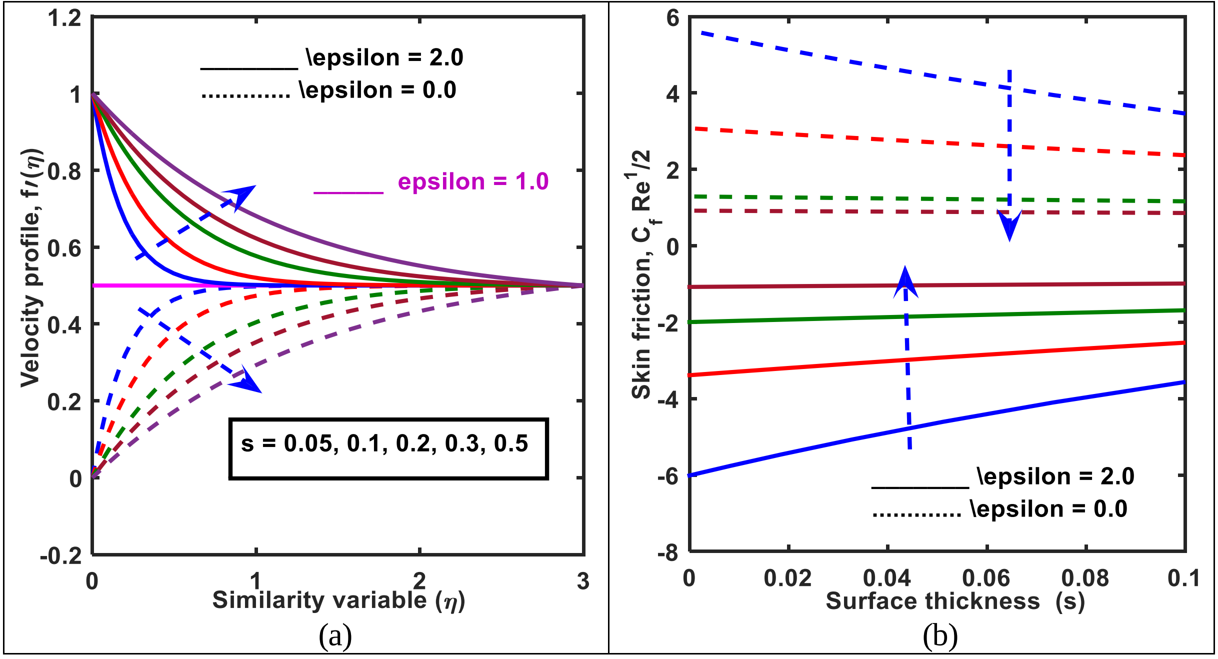

(a) (b)

Figure 7a and 7b illustrate the velocity profile for the increasing effect of stretching ratio parameter $\left(0 \le \varepsilon \le 2.0\right)$ consider the surface thickness parameter *s* = 0.05 and *s* = 2.0, respectively. From these figures, it is noticed that the velocity profile and boundary layer thickness expands when $\varepsilon > 1$ and the fluid flow form an inverted boundary layer pattern but in the case of $\varepsilon < 1$ the fluid flow form a certain boundary layer pattern. It is also observed that the velocity profile and boundary layer thickness satisfy the far-field boundary condition in the case of a thinner surface (*s* = 0.05). On the other hand, while the thicker surface (*s* = 2.0), the velocity profile is not in a parabolic shape, this is insignificant with the physical behavior because in this case, the boundary condition does not satisfy by the velocity profile. Therefore, the velocity boundary layer thickness is higher in the case of the thicker bullet-shaped object (s = 2.0) than the thinner bullet-shaped object (s = 0.05).

Figure 7. *Effect of Stretching Ratio Parameter (ϵ) on Velocity Profile Taking (a) s = 0.05 and ϵ = 0.0 (Lower Panel), ϵ =1.0 (Separation Line), ϵ = 2.0 (Upper Panel), and (b) s = 2.0 and ϵ = 0.0 (Lower Panel), ϵ =1.0 (Separation Line), ϵ = 2.0 (Upper Panel)*

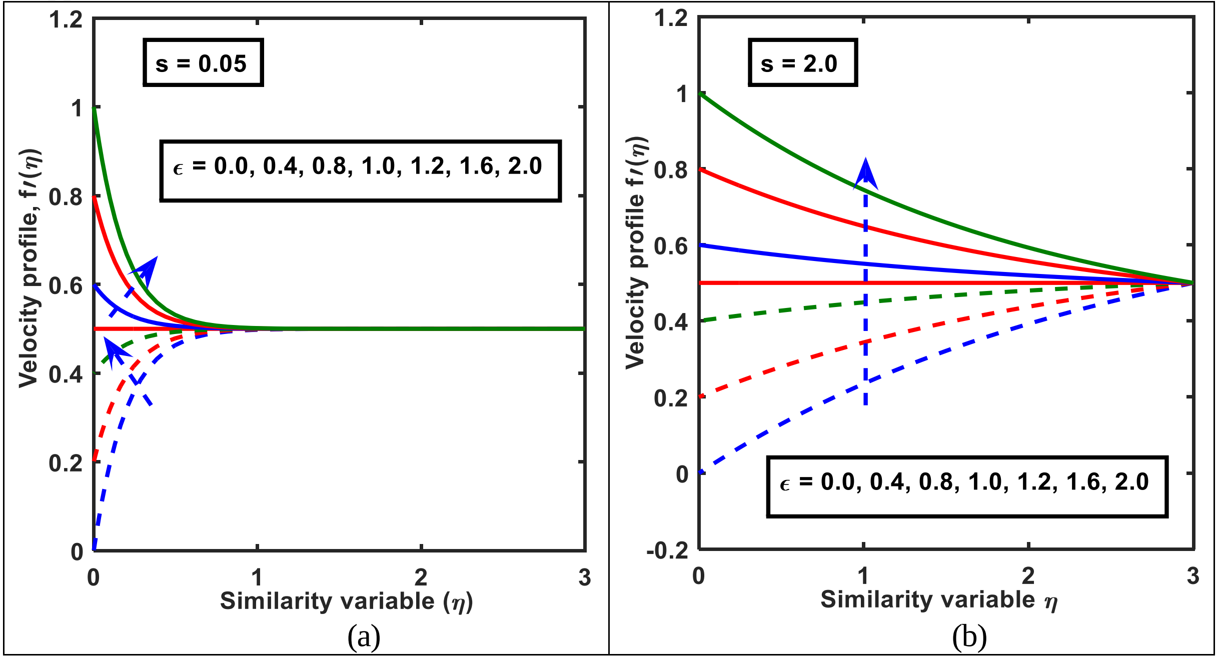

(a) (b)

From these figures, it is observed that the velocity profile and momentum boundary layer thickness is getting expand due to power-law index parameter (m), surface thickness parameter (s), and stretching ratio parameter (ϵ) whereas magnetic parameter (M) has a reverse effect on it in the case of $\varepsilon > 1$ for both of the thicker (s = 2.0) and thinner (s = 0.05) surfaces. On the other hand, in the case of $\varepsilon < 1$ the velocity profile and momentum boundary layer thickness are getting expand due to magnetic parameter (M), power-law index parameter (m), and stretching ratio parameter (ϵ) but squeezes for the surface thickness parameter (s). Again, it is also revealed that in the case of a thicker bullet-shaped object (s = 2.0) the velocity profile does not approach the ambient condition asymptotically but intersects the vertical axis with a steep angle and the boundary layer structure has no definite shape whereas in the case of a thinner bullet-shaped object (s = 0.05) the velocity profile converge the ambient condition asymptotically and the boundary layer structure has a definite shape. It is also noticed that the thinner bullet-shaped object represents a thinner momentum boundary layer than the thicker bullet-shaped object in both static and moving bullet-shaped objects.

Temperature Profiles and Nusselt Number

Figures 8a and 8b depicts the variation of Prandtl number (Pr) $(0.71 \le \Pr \le 10.0)$ on temperature profile when stretching ratio parameter $\varepsilon < 1$ or > 1 and the surface thickness parameter *s* = 0.05, *s* = 2.0, respectively. These plots represent that the temperature profile of the viscous fluid and thermal boundary layer thickness affected significantly with increasing Prandtl number.

Figure 8. *Temperature Profile for Different Values of Prandtl Number when (a) $\epsilon = 0$, s = 0.05, s = 2.0, and (b) $\epsilon = 2.0$, s = 0.05, s = 2.0*

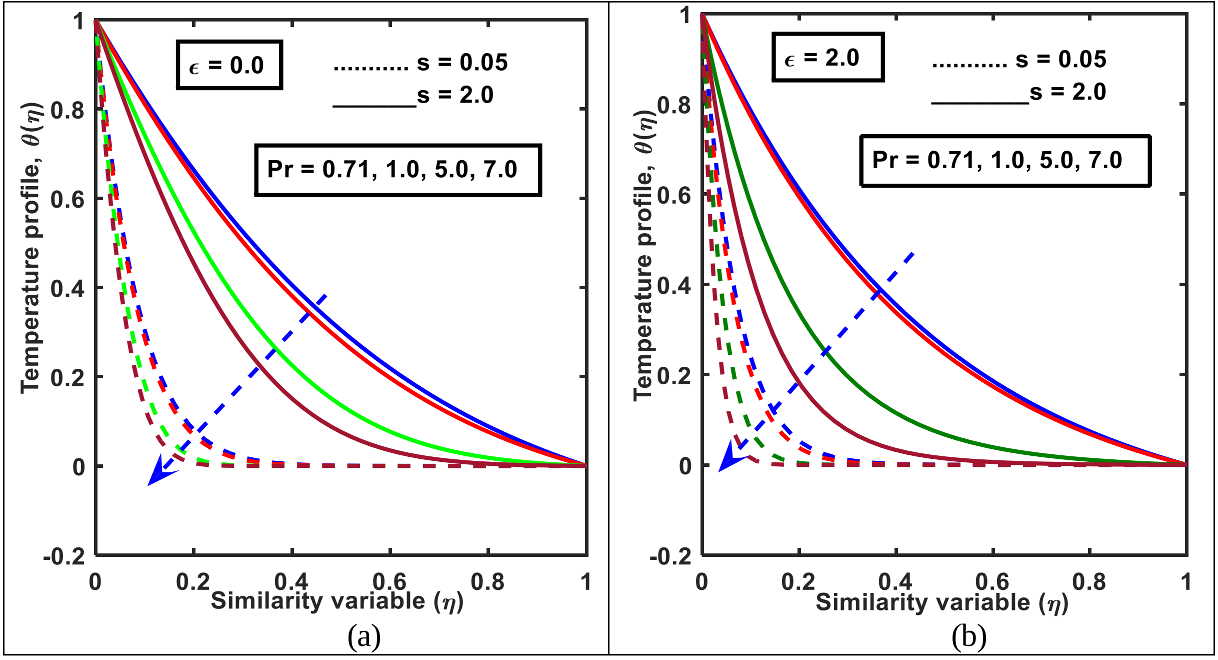

(a) (b)

It is seen from these figures that the variation of surface thickness parameter has a significant effect on fluid temperature in connection with the Prandtl number. From these figures, it is seen that the temperature profile and boundary layer thickness squeezes for both the thicker (*s* = 2.0, and thinner (*s* = 0.05) surfaces of the bullet-shaped object. It is also observed that the thermal boundary layer thickness is higher in the case of the thicker surface (*s* = 2.0) than the thinner surface (*s* = 0.05). This happens because a smaller Prandtl number means heat is quickly diffuse from the heated surface than for higher values of Pr. For increasing values of Prandtl number, the temperature profiles are closing to the solid surface. So, for cooling purposes, the Prandtl number can be used. A smaller surface thickness has a greater decelerating effect than a thicker surface. Therefore, it is noticed that for higher values of surface thickness parameter, the maximum temperature shows in the thermal boundary layer compared to that of lower surface thickness parameter.

Figure 9a and Figure 9b depict the influence of power-law index parameter on viscous fluid temperature for thinner surface (s = 0.05) and thicker surface (s = 2.0) when ϵ = 0.2 and 2.0 respectively. It is noticed from these figures that the variation of the surface thickness parameter has a significant effect on viscous fluid temperature in connection with the power-law index parameter. A lower surface thickness parameter has a greater decelerating effect. For thicker surfaces (s = 2.0) with increasing m, the decelerating effect is more prominent than for thinner surfaces (s = 0.05). Therefore, the thermal boundary layer thickness is higher due to the thicker surface when compared with the thinner surface. Figure 9c and Figure 9d also represent the influence of power-law index parameter on viscous fluid temperature for air (Pr = 0.71) and water (Pr = 7.0) when s = 0.05 and 2.0 respectively.

Figure 9. *Temperature Profile for Different Values of Power-Law Index Parameter (m) when (a) $\epsilon = 0.2$, s = 0.05, s = 2.0, (b) $\epsilon = 2.0$, s = 0.05, s = 2.0 (c) s = 0.2, Pr = 0.71, Pr = 7.0, and (d) s = 2.0, Pr = 0.71, Pr = 7.0*

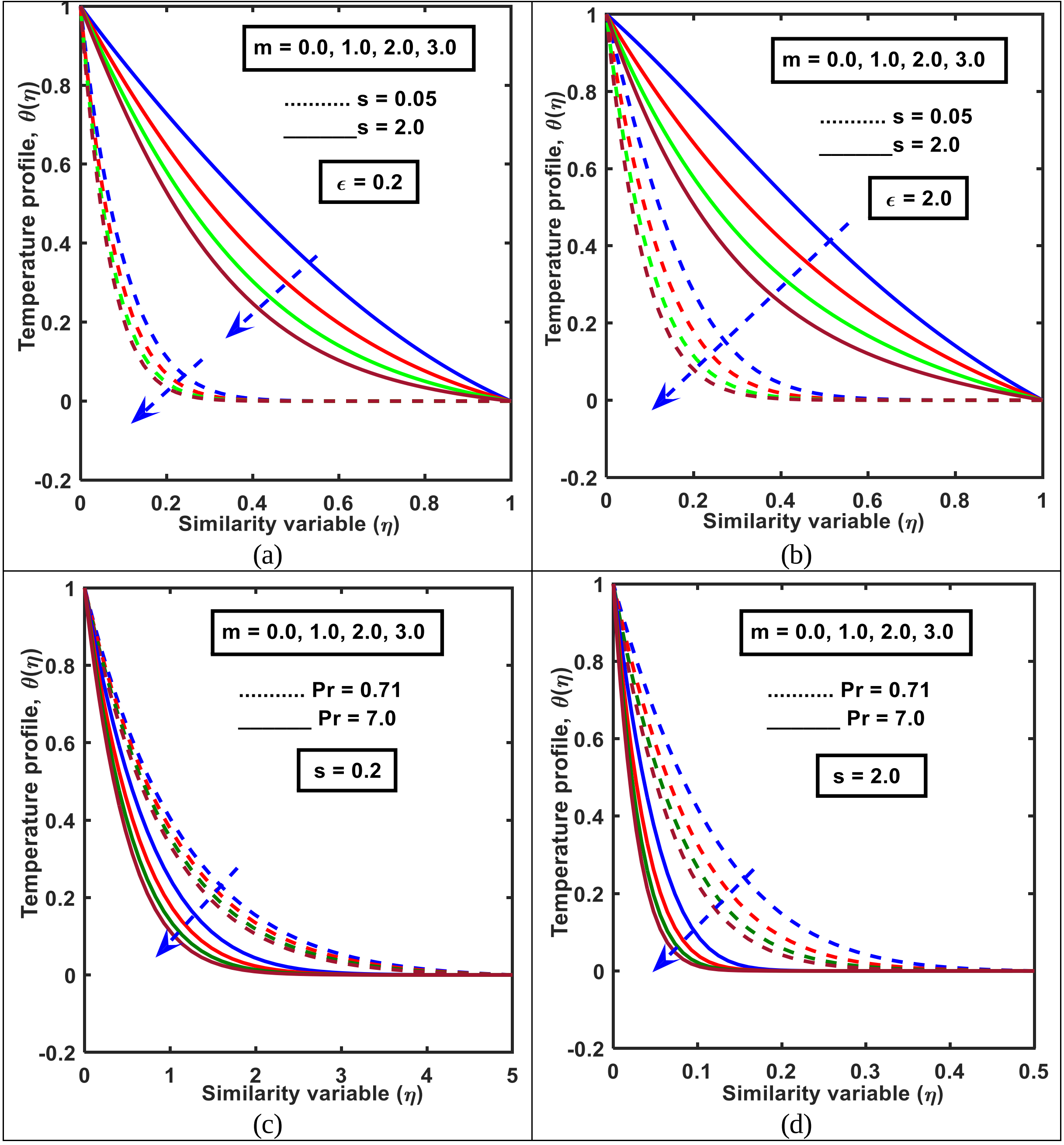

(a) (b)

(c) (d)

It is seen from these figures that the variation of the Prandtl number has a significant effect on viscous fluid temperature in connection with the power-law index parameter.

A higher Prandtl number has a greater decelerating effect. For air (Pr = 0.71) with increasing m, the decelerating effect is more prominent than for water (Pr = 7.0). Therefore, the thermal boundary layer thickness is higher for air when compared with water. From these figures, the temperature distribution and also the thermal boundary layer thickness decrease with the increase of *m* for all mentioned cases. These plots also represent that the temperature profile of the viscous fluid and thermal boundary layer thickness affected significantly with increasing power-law index parameter. Therefore, it is seen that for higher values of surface thickness parameter, the maximum temperature shows in the thermal boundary layer compared to that of lower surface thickness parameter. Again, in the case of air (Pr = 0.71), the highest temperature shows in the thermal boundary layer compared to that of water (Pr = 7.0).

Figure 10a and Figure 10b portray the influence of surface thickness parameter (*s*) on viscous fluid temperature for air (Pr = 0.71) and water (Pr = 7.0) when ϵ = 0.2 and 2.0 respectively. It shows that the temperature profile and thermal boundary layer thickness expand with an increase of surface thickness parameter because the heat transfer rate enhances.

Figure 10. *Temperature Profile for Different Values of Surface Thickness Parameter (s) when (a) ϵ = 0.2, Pr = 0.71, 7.0 and (b) ϵ = 2.0, Pr = 0.71, 7.0*

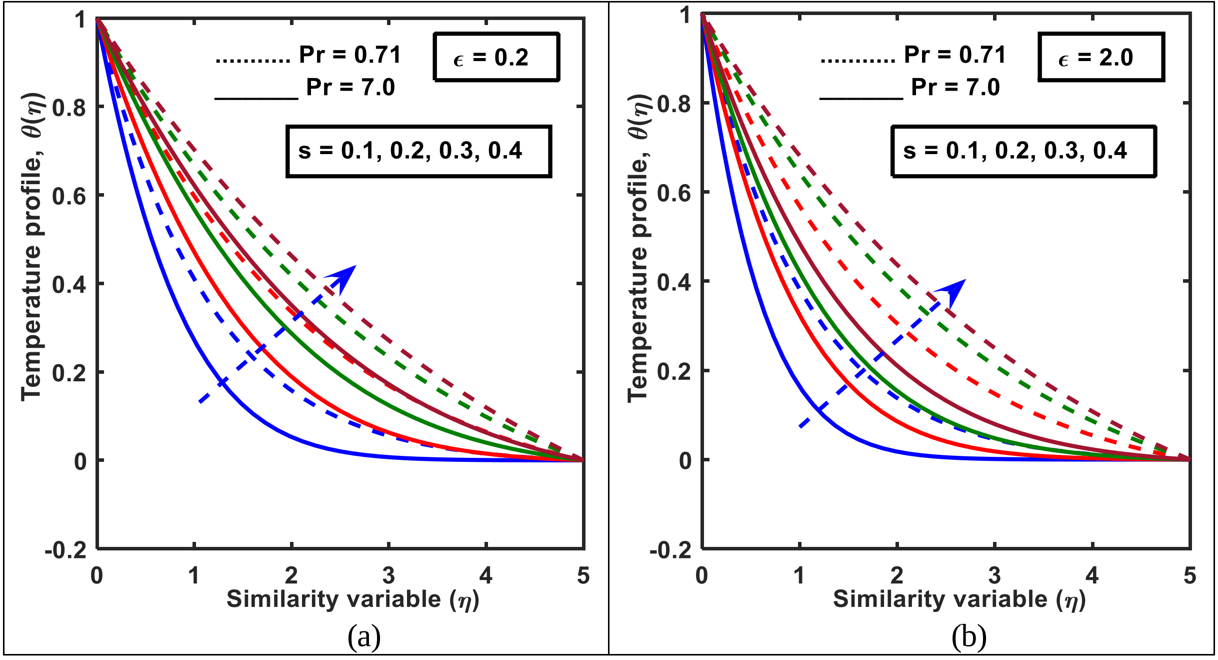

(a) (b)

It is seen from these figures that the variation of the Prandtl number has a significant effect on viscous fluid temperature in connection with the surface thickness parameter. A higher Prandtl number has a greater decelerating effect than a lower Prandtl number. For air (Pr = 0.71) with increasing *s*, the accelerating effect is more prominent than for water (Pr = 7.0). Therefore, the thermal boundary layer thickness is higher for air when compared with water. Again, in the case of air (Pr = 0.71), the highest temperature shows in the thermal boundary layer compared to that of water (Pr = 7.0).

Figure 11a and Figure 11b display the effects of the stretching ratio parameter (ϵ) on viscous fluid temperature for air (Pr = 0.71) and water (Pr = 7.0) when s = 0.05 and 2.0 respectively. It shows that the temperature profile and thermal boundary layer thickness squeeze with an increase of the stretching ratio parameter because the velocity profile increases for the effect of this parameter which tends to pass more fluid from the boundary layer region to the surrounding fluid.

Figure 11. *Temperature Profile for Different Values of Stretching Ratio Parameter (ϵ) when (a) s = 0.2, Pr = 0.71, Pr = 7.0 and (b) s = 2.0, Pr = 0.71, Pr = 7.0*

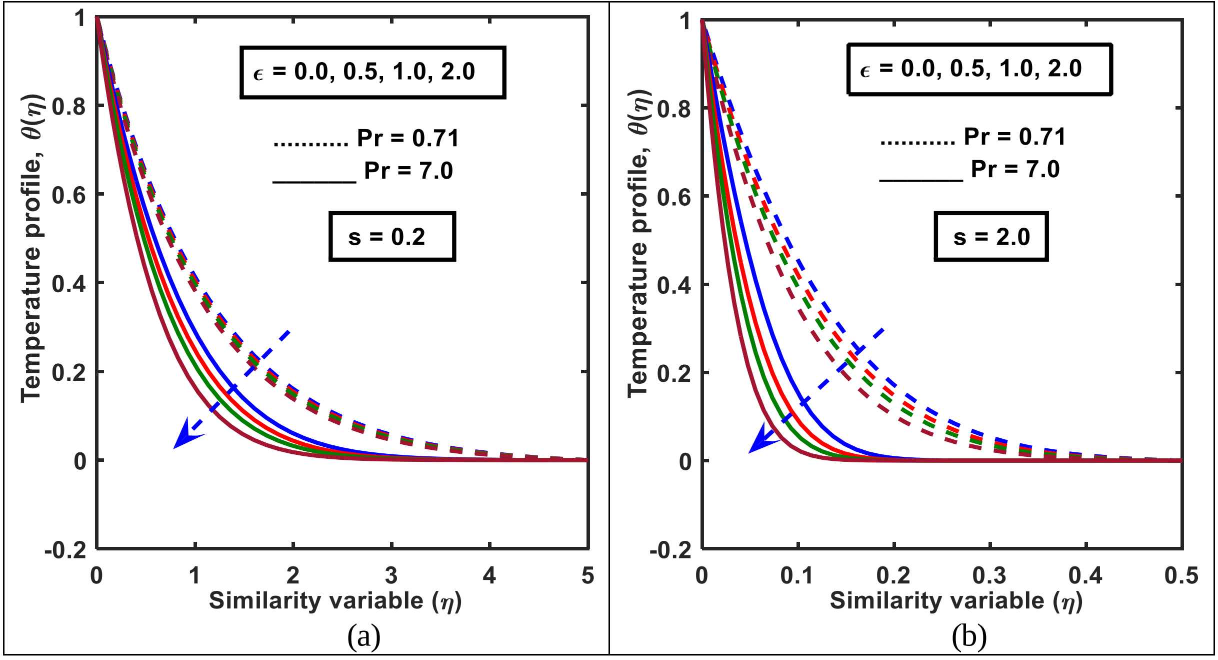

(a) (b)

It is seen from these figures that the variation of the Prandtl number has a significant effect on viscous fluid temperature in connection with the stretching ratio parameter. A higher Prandtl number has a greater decelerating effect. For water (Pr = 7.0) with increasing the stretching ratio parameter, the decelerating effect is more prominent than for air (Pr = 0.71). Again, in the case of air (Pr = 0.71), the highest temperature shows in the thermal boundary layer compared to that of water (Pr = 7.0).

Effect of Heat Generation Parameter (Q) on Temperature Profile and Nusselt Number*

Figures 12a-12f display the effect of heat generation parameter on the temperature profile and Nusselt number when the stretching ratio parameter ϵ = 0.2, ϵ = 2.0, the surface thickness parameter s = 0.05, s = 2.0, and Pr = 0.71, 7.0 respectively. Figure 12a and Figure 12b depict the influence of heat generation parameter on viscous fluid temperature for thinner surface (s = 0.05) and thicker surface (s = 2.0) when $\epsilon = 0.2$ and 2.0 respectively. These plots represent that the temperature profile of the viscous fluid and thermal boundary layer thickness affected significantly with increasing heat generation parameters. It is noticed from these figures that the variation of heat generation parameter has a significant effect on fluid temperature in connection with the surface thickness parameter and the Prandtl number. A lower surface thickness parameter has a lower accelerating effect. For thicker surfaces (s = 2.0) with increasing Q^*, the accelerating effect is more prominent than for thinner surfaces (s = 0.05). Therefore, the thermal boundary layer thickness is higher due to the thicker surface when compared with the thinner surface. Therefore, the temperature profile and boundary layer thickness expand for both of the thicker ($s = 2.0$) and thinner ($s = 0.05$) surfaces of the bullet-shaped object whereas the Nusselt number decreases (Figures 12e and 12f). Figures 12c and 12d also represent the influence of heat generation parameter on viscous fluid temperature for air (Pr = 0.71) and water (Pr = 7.0) when s = 0.05 and 2.0 respectively. It is seen from these figures that the variation of the Prandtl number has a significant effect on viscous fluid temperature in connection with the heat generation parameter. A higher Prandtl number has a greater accelerating effect on the temperature profile. For water (Pr = 0.71) with increasing Q^*, the accelerating effect is more prominent than for air (Pr = 0.71). Therefore, the thermal boundary layer thickness is higher for water when compared with air. However, the temperature attains its minimum for a low value of Prandtl number (Pr = 0.71) and a higher value of Prandtl number (Pr = 7.0) in connection with heat generation parameter shooting up the profiles near the surface of the bullet-shaped object within the region $\eta < 0.4$ and then the profile decreases sharply to meet the boundary condition as well. From these figures, the temperature profile and thermal boundary layer thickness increase with the increase of Q^* for all mentioned cases. Therefore, it is seen that for higher values of surface thickness parameter, the maximum temperature shows in the thermal boundary layer compared to that of lower surface thickness parameter. Again, in the case of water (Pr = 7.0), the highest temperature shows in the thermal boundary layer compared to that of air (Pr = 0.71). It happens because heat sources produce more heat energy near the surface as a result the temperature of the fluid increases.

Figure 12. *Effect of Heat Generation Q* on Temperature Profile and Local Nusselt Number when (a)* $\epsilon = 0.2$, $s = 0.05$, $s = 2.0$ *(b)* $\epsilon = 2.0$, $s = 0.05$, $s = 2.0$ *(c)* $s = 0.05$, $Pr = 0.71$, $Pr = 7.0$ *(d)* $s = 2.0$, $Pr = 0.71$, $Pr = 7.0$ *(e)* $\epsilon = 0.2$, $s = 0.05$, $Pr = 0.71$, *and (f)* $\epsilon = 2.0$, $s = 0.05$, $Pr = 0.71$

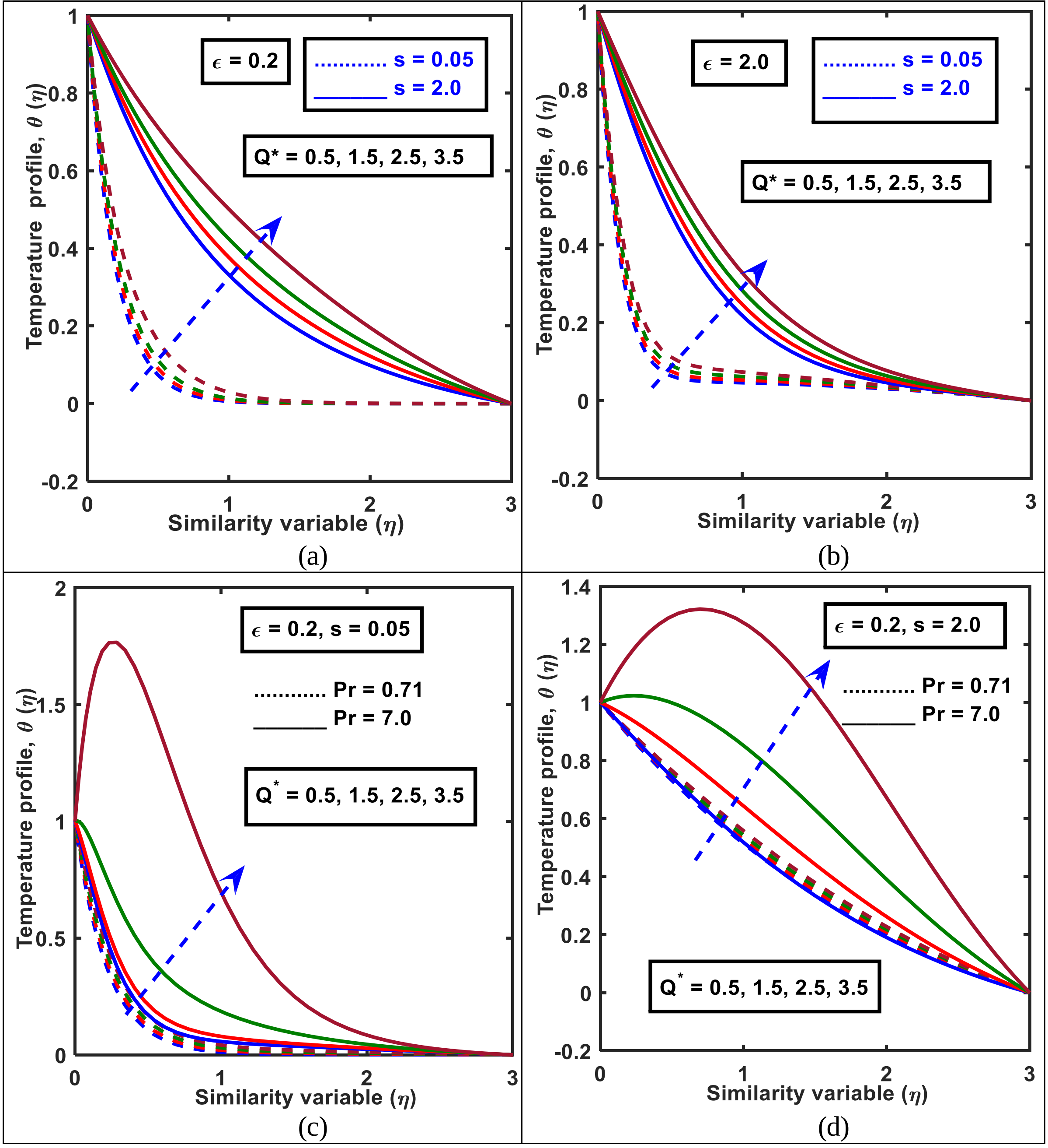

(a) (b)

(c) (d)

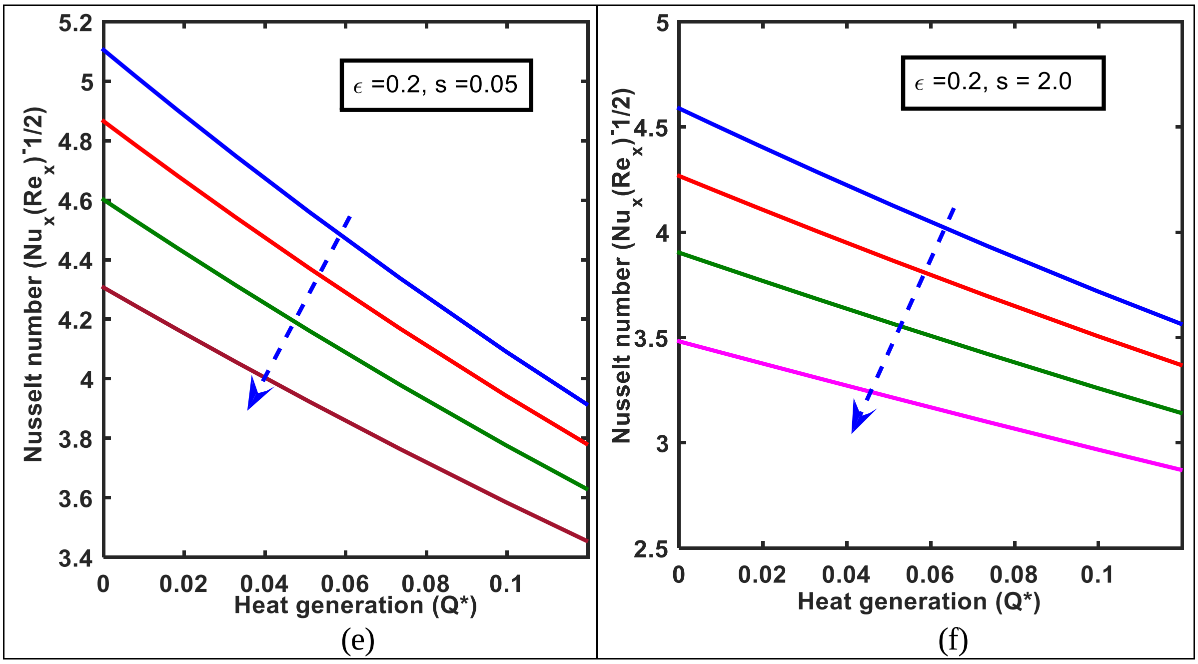

(e) (f)

The graph of temperature profile represents that the fluid temperature within the boundary layer region is getting lower due to Prandtl number, power-law index parameter, and stretching ratio parameter whereas surface thickness parameter has a reverse effect on it throughout the boundary layer region. From these figures, it is also revealed that in the case of a thicker bullet-shaped object (s = 2.0) the temperature profile does not approach the ambient condition asymptotically but intersects the axis with a steep angle and the boundary layer structure has no definite shape whereas in the case of a thinner bullet-shaped object (s = 0.05) the temperature profile converge the ambient condition asymptotically and the boundary layer structure has a definite shape. Here also one can notice that the thinner bullet-shaped object acts as a good cooling conductor compared to the thicker bullet-shaped object for both $\epsilon = 0.0$ and 2.0. It is also mentioned that the thinner bullet-shaped object represents a thinner thermal boundary layer because the heat transfer rate is higher than the thicker bullet-shaped object in both static and moving bullet-shaped objects. Hence it is mentioned that the lower values of the surface thickness parameter have a greater depressing effect on the temperature profile than higher values of the surface thickness parameter. It is also noticed that the thermal boundary layer thickness is higher for air when compared with water.

The variation of the Nusselt number against the effect of the Prandtl number displays in Figures 13a and 13b by taking the stretching ratio parameter $\epsilon = 0.0$ and $\epsilon = 2.0$, and the surface thickness parameter $s = 0.05$, respectively.

Figure 13. *Nusselt Number for Different Values of Prandtl Number when (a) ϵ = 0.0, s = 0.05, and (b) ϵ = 2.0, s = 0.05*

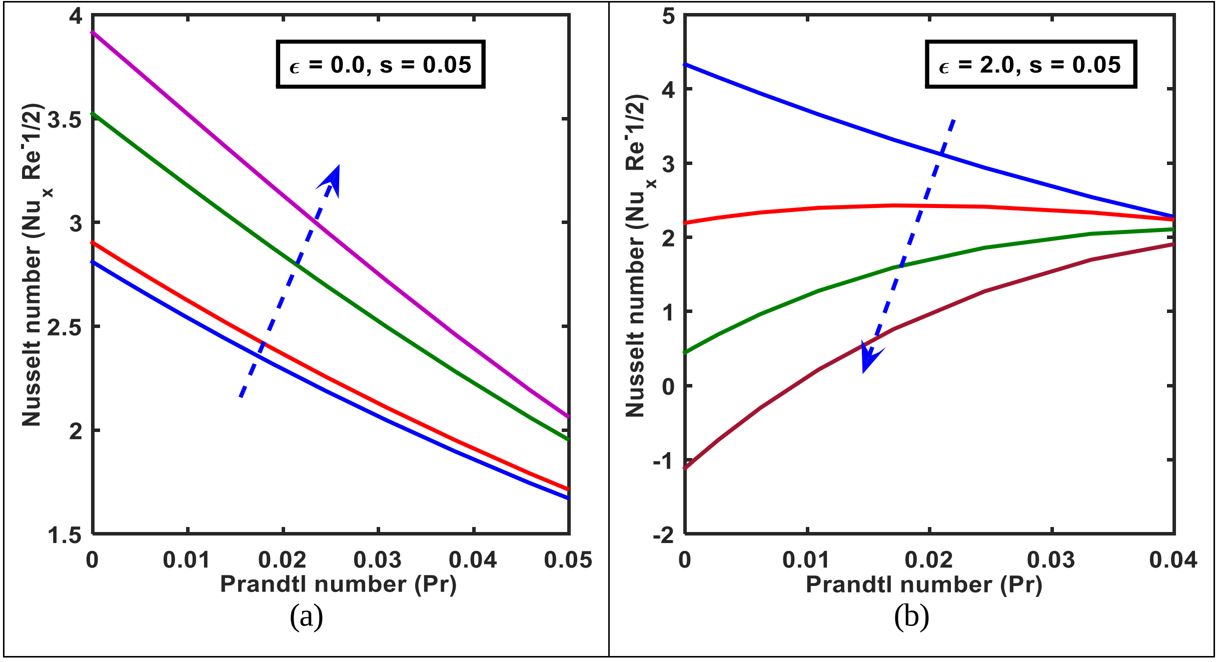

(a) (b)

From these figures, it reveals that, the Nusselt number increase as the Prandtl number increases. It is observed that the Nusselt number is directly proportional to the temperature gradient. The temperature gradient at the surface is always negative for all values of the controlling parameters. Therefore, the Prandtl number is an increasing function of the Nusselt number. It is observed from Table 2 that, when Pr changes from 0.71 to 10.0 for s = 0.05 and ϵ = 0.0, the Nusselt number increases 17.8 % whereas for s = 0.05 and ϵ = 2.0 the corresponding increases 48.8%. Hence, the Nusselt number is higher for the stretching surface (ϵ = 2.0) than the non-stretching surface (ε = 0).

Influence of Power-Law Index Parameter (m) on Nusselt Number

Figures 14a and 14b represent the variation of Nusselt number with respect to power-law index parameter by taking the stretching ratio parameter ϵ = 0.0 and ϵ = 2.0, and the surface thickness parameter s = 0.05, respectively. From these figures, it reveals that as the values of m increases the Nusselt number also increases. Therefore, the power-law index parameter is directly proportional to the Nusselt number.

Figure 14. *Nusselt Number for Different Values of Power-Law Index Parameter (m) when (a) $\epsilon = 0.0$, s = 0.05, and (b) $\epsilon = 0.0$, s = 2.0*

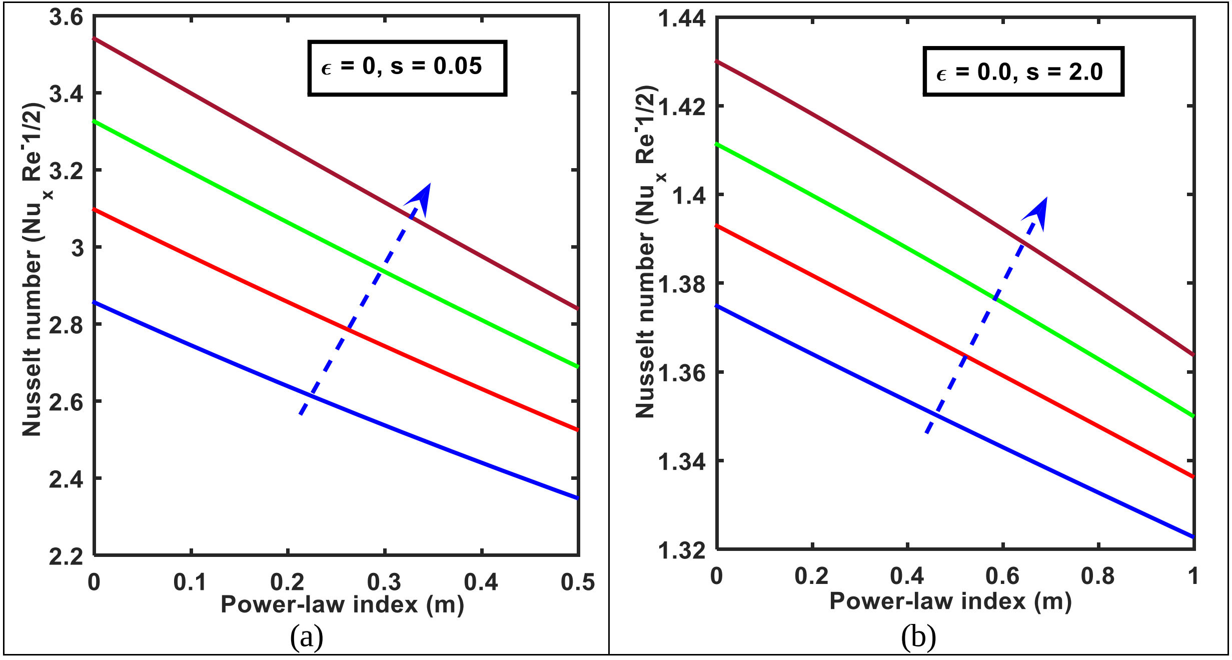

(a) (b)

It is observed from Table 2 that, when *m* changes from 0 to 2 for *s* = 0.05 and $\epsilon = 0.0$, the Nusselt number increases 8.85 % whereas for *s* = 0.05 and $\epsilon = 2.0$ the corresponding increases 23.8%. Hence, the Nusselt number is higher for the stretching surface ($\epsilon = 2.0$) than the non-stretching surface ($\varepsilon = 0$).

Effect of Surface Thickness Parameter (s) on Nusselt Number

Figures 15a and 15b represent the variation of Nusselt number with respect to surface thickness parameter (*s*) also taking the stretching ratio parameter $\epsilon = 0.0$ and $\epsilon = 2.0$, respectively. From these figures, it reveals that as the values of *s* increase the Nusselt number decreases. Therefore, the Nusselt number is a decreasing function of the surface thickness parameter. This implies heat transfer rate is higher in the case of a thinner (*s* = 0.05) bullet-shaped object than the thicker (*s* = 2.0) bullet-shaped object. It is observed from Table 2 that, when *s* changes from 0.05 to 0.3 for $\epsilon = 0.0$, the Nusselt number decreases 85.76 % whereas for $\epsilon = 2.0$ the corresponding decreases 77.4%. Hence, the Nusselt number is higher for $\epsilon = 0.0$ than $\epsilon = 2.0$.

Figure 15. *Nusselt Number for Different Values of Surface Thickness Parameter (s) when (a) ϵ = 0.0, and (b) ϵ = 2.0*

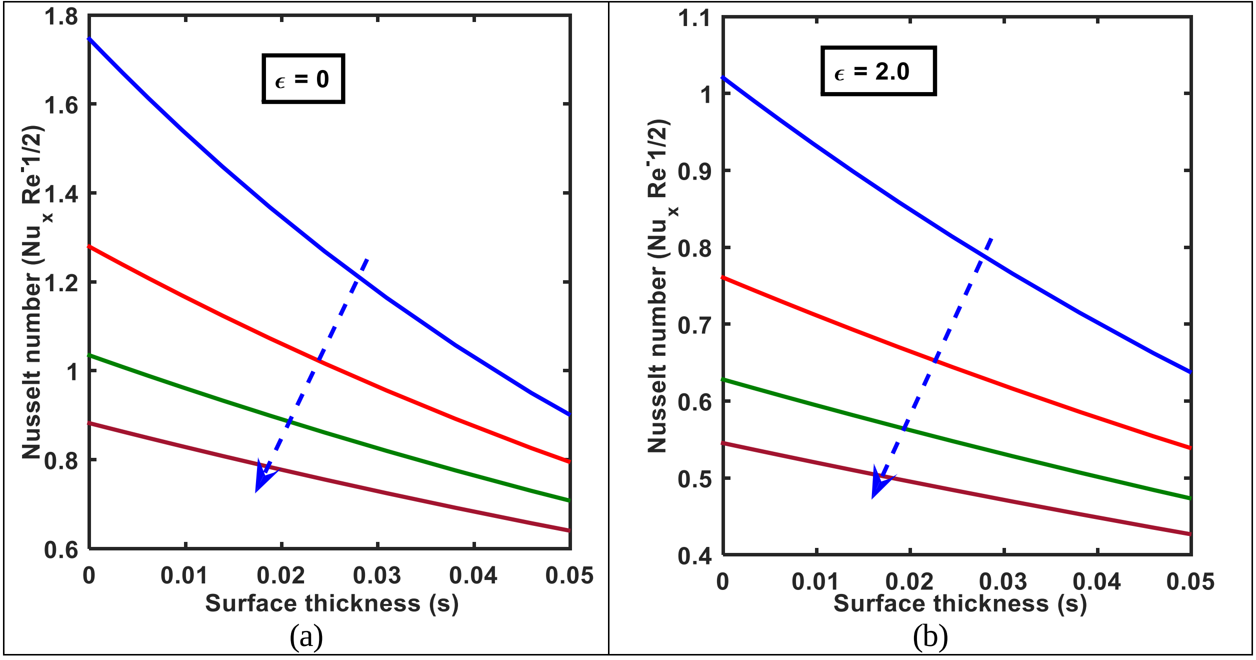

(a) (b)

Table 1 represents the variation in skin friction coefficient for different values of the magnetic parameter (*M*), surface thickness parameter (*s*), Prandtl number (Pr), and power-law index parameter (*m*) for various movements of the bullet-shaped object.

Table 1. *Variation in Skin Friction Coefficient for Distinct Values of M, m, s, and Pr with ϵ = 0.0, 0.2, 2.0, s = 0.05*

Parameters				$-C_f\sqrt{\mathrm{Re}_x}$ $\epsilon = 0.0, s = 0.05$	$-C_f\sqrt{\mathrm{Re}_x}$ $\epsilon = 0.2, s = 0.05$	$\left\|-C_f\sqrt{\mathrm{Re}_x}\right\|_{\epsilon=}$ $2.0, s = 0.05$
M	*m*	*s*	Pr			
1.0	1.0	0.05	1.0	**5.6404**	**4.5437**	**6.0131**
5.0	1.0	0.05	1.0	**6.3441**	**5.1011**	**6.6555**
10.0	1.0	0.05	1.0	**7. 0787**	**5.6847**	**7.3436**
1.0	**0.0**	0.05	1.0	**5.3397**	**4.2886**	**5.5421**
1.0	**1.0**	0.05	1.0	**5.6404**	**4.5437**	**6.0131**
1.0	**2.0**	0.05	1.0	**5.9128**	**4.7745**	**6.4342**
1.0	1.0	**0.05**	1.0	**5.6404**	**4.5437**	**6.0131**
1.0	1.0	**0.20**	1.0	**1.7491**	**1.4322**	**1.9969**
1.0	1.0	**0.3**	1.0	**1.3251**	**1.0771**	**1.4993**
1.0	1.0	0.05	**0.71**	**5.6404**	**4.5437**	**6.0131**
1.0	1.0	0.05	**1.0**	**5.6404**	**4.5437**	**6.0131**
1.0	1.0	0.05	**7.0**	**5.6404**	**4.5437**	**6.0131**

It is observed that the skin friction coefficient is inversely proportional to the velocity gradient, $f''(\eta)$ at the bullet-shaped object. So, the velocity gradient at the surface of the object is negative for all values of mentioned parameters in the case of $\varepsilon > 1$ but positive when $\varepsilon < 1$. The negative values $f''(\eta)$ mean that the bullet-shaped object exerts a drag force on the fluid flow whereas the positive values $f''(\eta)$ mean that the fluid flow exerts a drag force on the bullet-shaped object. From Table 1, it is observed that the magnetic parameter (*M)* and power-law index parameter (*m*) reducing the friction factor coefficient in the case of $\varepsilon < 1$ but boosting the friction factor in the case of $\varepsilon > 1$. On the other hand, the surface thickness parameter reduces the friction factor in both of the mentioned cases. It is interesting to note that friction factor coefficient is less in ϵ = 0.2 case when compared with ϵ = 0.0, ϵ = 2.0 cases. At this point, it is highlighted that for reducing the friction between the particles and surface we have to use ϵ = 0.2 cases. It is evident from this table that the skin friction coefficient is higher in ϵ = 2.0 case when comparing with ϵ = 0.0, ϵ = 0.2 cases. It is also noticed that the Prandtl number (Pr) does not affect the skin friction coefficient.

Table 2 displays the variation in Nusselt number for different values of the magnetic parameter (*M*), surface thickness parameter (*s*), Prandtl number (Pr), and power-law index parameter (*m*) for various movements of the bullet-shaped object. It is observed that the Nusselt number is directly proportional to the heat transfer rate $\theta'(\eta)$ at the bullet-shaped object. The heat transfer rate at the surface of the object $\theta'(\eta)$ is negative for all values of mentioned parameters. From Table 2, it is possible to observe that the heat transfer rate increases for the magnetic parameter (*M*), Prandtl number (Pr), and power-law index parameter (*m*) but decreases for the surface thickness parameter (*s*) for all three cases of stretching ratio parameter (ϵ = 0.0, ϵ = 0.2, ϵ = 2.0) and s = 0.05 respectively. On the other hand, in the case of ϵ = 2.0, and s = 0.05 the heat transfer rate increases for the magnetic parameter (*M*) and surface thickness parameter (*s*) whereas decreases for Prandtl number (Pr), and power-law index parameter (*m*). Therefore, heat transfer rate is high in ϵ = 0.0 case, when compared with ϵ = 0.2, ϵ = 2.0 cases. At this point, it is highlighted that for reducing the heat transfer rate we have to consider the static (ϵ = 0.0) bullet-shaped object.

Table 2. *Variation in Nusselt Number,* $Nu_x\left(\sqrt{\mathrm{Re}_x}\right)^{-1}$ *for Different Values of M, m, s, and Pr with* ϵ *= 0.0, 0.2, 2.0, s = 0.05*

Parameters				$\left\Vert -Nu_x\left(\sqrt{\mathrm{Re}_x}\right)^{-1}\right\Vert$	$\left\Vert -Nu_x\left(\sqrt{\mathrm{Re}_x}\right)^{-1}\right\Vert$	$\left\Vert -Nu_x\left(\sqrt{\mathrm{Re}_x}\right)^{-1}\right\Vert$
M	m	s	Pr	ϵ = 0.0, s = 0.05	ϵ = 0.2, s = 0.05	ϵ = 2.0, s = 0.05
1.0	1.0	0.05	1.0	**10.4671**	**10.6800**	**11.2800**
5.0	1.0	0.05	1.0	**10.4911**	**10.6912**	**11.2611**
10.0	1.0	0.05	1.0	**10.5134**	**10.7019**	**11.2426**
1.0	**0.0**	0.05	1.0	**10.0001**	**10.0001**	**10.0000**
1.0	**1.0**	0.05	1.0	**10.4671**	**10.6800**	**11.2800**
1.0	**2.0**	0.05	1.0	**10.8845**	**11.2824**	**12.3826**
1.0	1.0	**0.05**	1.0	**10.4671**	**10.6800**	**11.2800**
1.0	1.0	**0.20**	1.0	**2.9202**	**3.1327**	**3.4985**
1.0	1.0	**0.30**	1.0	**1.4899**	**2.3417**	**2.5867**
1.0	1.0	0.05	**0.71**	**10.3431**	**10.4981**	**10.9376**
1.0	1.0	0.05	**1.0**	**10.4671**	**10.6800**	**11.2800**
1.0	1.0	0.05	**7.0**	**12.1862**	**13.3201**	**16.2761**

Figures 16a and 16b show the convergence and accuracy of the present problem. Figure 16a depicts the infinity norms with iterations. The error infinity norm decreases with the increasing number of iterations that confirms the convergence of the present method. So, the present method converges after five iterations. Figure 16b represents the residual error norms of less than 10^{-8} and 10^{-14} for $f(\eta)$ and $\theta(\eta)$ against after fourth iterations. It is seen that the residual error decreases with increasing the iterations. This proves the validity of the present method. The errors show that the SQLM is accurate giving errors of less than 10^{-8} within the fourth iteration.

Figure 16. (a) *Error Infinity Norms and (b) Residual Error Infinity Norms for* $f(\eta)$ *and* $\theta(\eta)$

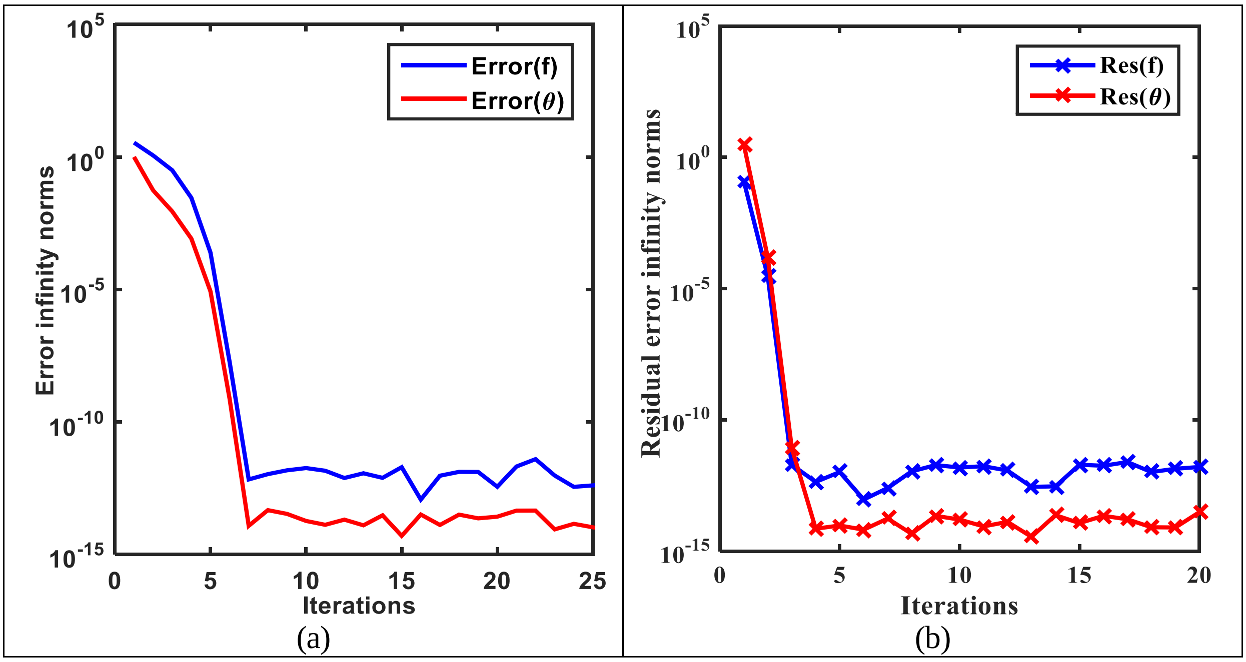

(a) (b)

Correlation Analysis for Velocity Gradient

A positive correlation means higher values of one variable tend to higher values of another variable but the reverse case arises for the negative correlation. The statistically significant values of the parameters are highlighted in the table because the values are greater equal to 0.25. Then we say that a 95% chance of a relationship between the parameters. So, from Table 3 it is observed that the velocity gradient is positively correlated with the magnetic parameter (*M*), and power-law index parameter (*m*) but negatively correlated with the surface thickness parameter (*s*) and stretching ratio parameter (ϵ). Therefore, the fluid velocity and gradient of velocity is an increasing function of the magnetic parameter, and power-law index parameter but *a* decreasing function of the surface thickness parameter and stretching ratio parameter within the boundary layer region.

Table 3. *Correlation Coefficient between the Velocity Gradient* $f''(\eta)$ *and Controlling Parameters by Taking* 1^{st} *Order Coefficient in the Case of* $\epsilon = 0.2$

Parameters	M	s	m	ϵ	$f''(\eta)$
M	1.00				
s	-0.22	1.00			
m	-0.09	-0.08	1.00		
ϵ	0.17	0.15	0.07	1.00	
$f''(0)$	**0.52**	**-0. 43**	**0.21**	**-0.33**	1.00

Correlation Analysis for Temperature Gradient

A positive correlation means higher values of one variable tend to higher values of another variable but the reverse case arises for the positive correlation. The correlations are significant between the variables if the numerical value of 0.25 or above. Then we say that a 95% chance of a relationship between the parameters. So, from Table 4 the correlation is significant for all mentioned parameters except the stretching ratio parameter which is highlighted in the table. The temperature gradient is positively correlated with the parameters Pr, M, m, and ϵ but negatively correlated with the parameter s and Q*.

Table 4. *Correlation Coefficient Between the Temperature Gradient* $\theta'(\eta)$ *and Controlling Parameters by Taking Zero-Order Coefficient*

Correlation Summary							
Parameters	Pr	M	m	s	Q^*	ϵ	$\theta'(\eta)$
Pr	1.00						
M	0.59	1.00					
m	-0.08	-0.13	1.00				
s	-0.14	-0.21	-0.08	1.00			
Q^*	-0.09	-0.06	-0.09	0.00	1..00		
ϵ	0.00	0.00	0.00	0.00	-0.09	1.00	
$\theta'(\eta)$	**0.45**	**0.44**	**0.28**	**-0.66**	-0.15	**0.23**	1.00

From Table 5 it is observed that all the parameters are statistically significant because their P – VALUEs less than 0.05. Hence at least a 95% chance that there is a true relationship between the parameters and the velocity gradient. From the regression model it is observed that if we increase the one-unit value of the magnetic parameter (M) and power – law index parameter (m) then the average decrease of the skin friction coefficient by 0.8. From the table the regression model is

$$f''(\eta) = 0.2M + 1.1m - 0.6s + 1.3\mathrm{Pr} - 0.3\varepsilon$$

Table 5. *Regression Analyses for the Dimensionless Parameters M, m, and s and the Velocity* $f''(\eta)$ *by Taking 2nd Order Coefficient*

Regression Statistics						
Multiple R	0.758					
R Square	0.575					
Adjusted R Square	0.368					
Standard Error	1.368					
Observations	18.00					
	df	SS	MS	F	Significance F	
Regression	5.00	32.946	6.589	3.522	0.034	
Residual	13.00	24.321	1.871			
Total	18.00	57.267				
	Coefficients	Standard Error	t Stat	P-value	Lower 95%	Upper 95%
Intercept	0.00	#N/A	#N/A	#N/A	#N/A	#N/A
M	0.2	0.064	-3.039	**0.009**	-0.335	-0.057
s	-0.6	0.687	-0.866	0.402	-2.080	0.889
m	1.1	0.426	-2.366	**0.034**	-1.929	-0.088
Pr	1.3	0.803	1.569	0.141	-0.475	2.993
ϵ	-0.3	0.427	-0.673	0.513	-1.210	0.636

From Table 6 the regression model is $\theta'(\eta) = 1.841 + 0.19\,\mathrm{Pr} + 0.16M + 0.47m - 1.21s + 0.33\varepsilon - 0.3Q*$. In the regression analysis the variables are significant if P – VALUE less than 0.05 and this is the condition to develop a true relationship between dependent and independent variables. From Table 6 the significant variables are only the surface thickness parameter (s) which is highlighted in the table. From the regression model it is observed that if we increase the one unit value of the Prandtl number (Pr), power – law index parameter m, surface thickness parameter s and stretching ratio (ϵ) and then the average increase of the skin friction coefficient by 0.307, 0.0548, 2.13 and 0.853. Again, if we increase the one-unit value of surface thickness parameter s then the average decreases of the skin friction coefficient by 21.71.

Table 6. *Regression Analyses of the Energy Transfer* $\theta'(\eta)$ *by Taking 0 (Zero) Order Coefficient*

Regression Statistics						
Multiple R	0.841					
R Square	0.708					
Adjusted R Square	0.525					
Standard Error	0.773					
Observations	14.00					
	df	SS	MS	F	Significance F	
Regression	5.00	11.56	2.312	3.873	**0.044**	
Residual	8.00	4.776	0.597			
Total	13.00	16.36				
	Coefficients	Standard Error	t Stat	P-value	Lower 95%	Upper 95%

Intercept	1.841	0.602	3.05	0.016	0.452	3.230
Pr	0.184	0.152	1.21	0.260	-0.166	0.535
M	0.162	0.204	0.79	0.450	-0.309	0.633
m	0.469	0.328	1.43	0.190	-0.287	1.226
s	-1.213	0.432	-2.80	**0.023**	-2.208	-0.217
Q*	-0.30	0.07	-3.96	0.00	-0.45	-0.14
ϵ	0.325	0.273	1.19	0.26	-0.305	0.955

Code Verification

The numerical values $f''(\eta)$ have been compared with the results of Afridi and Qasim (2018) for different values of η to validate the convergence and accuracy of the present method. The results are almost similar to the previous results which are shown in Table 7.

Table 7. *Comparison of Skin Friction* $f''(\eta)$ *for Different Values of* η *with Afridi* (2018) *by Taking M = m = 0 and Pr = 1*

	Afridi	Present results
η	$f''(0)$	$f''(\eta)$
0.001	**62.1637**	**62.1572**
0.01	**8.4924**	**8.4912**
0.10	**1.2888**	**1.2839**
0.15	-	**0.9359**

Conclusions

The effect of various parameters on MHD laminar boundary layer flow of an incompressible, electrically conducting, and viscous Newtonian fluid past a stretching electrically non-conducting bullet-shaped object with heat transfer has been carried out. In sequence, the fluid flow and heat transfer have been investigated in two types of flow geometries such as the thicker surface $(s \geq 2)$ and the thinner surface $(0 < s < 2)$ of the bullet-shaped object.

- The SQLM along with the Chebyshev collocation method provides a more accurate and quicker convergence scheme.
- Velocity profile squeezes for the limit $\varepsilon > 1$ but in the limit, $\varepsilon < 1$ the velocity profile enhances for increasing the shape and size (surface thickness parameter, *s*) of the bullet-shaped object but the boundary layer thickness expands in both cases.
- In the case of the thinner bullet-shaped object, $(0 < s < 2)$ the fluid velocity profile converges asymptotically to the free stream velocity at infinity whereas for a thicker bullet-shaped object $(s \geq 2)$ boundary conditions do not satisfy.

- A thin momentum boundary layer thickness has been found in a thinner bullet-shaped object $\left(0<s<2\right)$ than the thicker bullet-shaped object $\left(s\geq 2\right)$.
- The thinner bullet-shaped object $\left(0<s<2\right)$ represents a thinner thermal boundary layer because the heat transfer rate is higher than the thicker bullet-shaped object $\left(s\geq 2\right)$.
- There is a positive correlation exists of the magnetic parameter (M) and power – law index (m) with velocity gradient and but negative correlation exists for surface thickness parameter (s) whereas there is no correlation for Prandtl number (Pr).
- A strong positive correlation exists with temperature gradient of the parameters such as Prandtl number, power – law index whereas a negative correlation exists of the magnetic, heat generation and surface thickness parameters. Further, a positive weak correlation exists between temperature gradient and stretching ratio parameter.
- The skin friction reduces for the magnetic parameter and power – law index parameter but increases for surface thickness parameter rate and stretching ratio parameter.

References

Abo-Eldahab EM, Salem AM (2004) Hall effects on MHD free convection flow of a non-Newtonian power-law fluid at a stretching surface. *International Communications in Heat and Mass Transfer* 31(3): 343–354.

Afridi IM, Qasim M (2018) Entropy generation and heat transfer in boundary layer flow over a thin needle moving in a parallel stream in the presence of nonlinear Rosseland radiation. *International Journal of Thermal Sciences* 123(Jan): 117–128.

Aftab A, Javed IS, Muhammad S (2018) Dual solutions in a boundary layer flow of a power-law fluid over a moving permeable flat plate with thermal radiation, viscous dissipation and heat generation/absorption. *Fluids* 3(1): 1–6.

Ahmad B, Nieto J, Shahzad N (2001) The Bellman quasi-linearization method for Neumann problems. *Journal of Mathematical Analysis and Applications* 257(2): 356–363.

Ahmad B, Nieto J, Shahzad N (2002) Generalized quasi-linearization method for mixed boundary value problems. *Applied Mathematics and Computation* 133(2–3): 423–429.

Ajala OA, Aselebe LO, Abimbade SF, Ogunsola AW (2019) Effect of magnetic fields on the boundary layer flow of heat transfer with variable viscosity in the presence of thermal radiation. *International Journal of Scientific and Research Publication* 9(5): 13–19.

Ajaykumar M, Srinivasa AH (2020) Variable viscosity effects on unsteady MHD laminar boundary layer flow and heat transfer over a stretching sheet. In *AIP Conference Proceedings*, 2277.

Alam M S, Asiya KM, Rahman MM, Vajravelu K (2016) Effects of variable fluid properties and thermophoresis on unsteady forced convective boundary layer flow along a permeable stretching/shrinking wedge with variable Prandtl and Schmidt numbers. *International Journal of Mechanical Sciences* 105(Jan): 191–205.

Alarifi IM, Ahmed GA, Osman M, Liaquat AL, Ayed MB, Belmabrouk H, et al. (2019) MHD flow and heat transfer over a vertical stretching sheet with heat sink or source effect. *Symmetry* 11(3): 297.

Asaithambi A (1998) A finite-difference method for the solution of the Falkner-Skan equation. *Applied Mathematics and Computation* 92(2–3): 135–141.

Ashwini G, Eswara AT (2012) MHD Falkner-Skan boundary layer flow with internal heat generation or absorption. *International Journal of Mathematical, Computational, Physical, Electrical and Computer Engineering* 6(5): 556–559.

Ashwini G, Eswara AT (2015) Unsteady MHD decelerating flow over a wedge with heat generation/absorption. *International Journal of Mathematics and Computer Science* 1(5): 303–309.

Awaludin IS, Ishak A, Pop I (2018) On the stability of MHD boundary layer flow over a stretching/shrinking wedge. *Scientific Reports* 8(1): 13622.

Bellman R E, Kalaba R E (1965) Quasilinearization and nonlinear boundary value problems. New York, USA: American Elsevier.

Daba M, Devaraj P, Subhashini SV (2015) Mixed convection boundary layer flow over a vertical stretching sheet with convective boundary condition and effect of partial slip. *Frontiers in Heat and Mass Transfer* 6(1): 1–6.

Falana A, Ojewale OA, Adeboje TB (2016) Effect of Brownian motion and thermophoresis on a nonlinearly stretching permeable sheet in a nanofluid. *Advances in Nanoparticles* 5(1): 140–151.

Ibrahim W, Tulu A (2019) Magnetohydrodynamic (MHD) boundary layer flow past a wedge with heat transfer and viscous effects of nanofluid embedded in porous media. *Mathematical Problems in Engineering* 1(Jan): 1–12.

Irfan M, Farooq MA, Mushtaq A, Shamsi ZH (2020) Unsteady MHD bio-nanofluid flow in a porous medium with thermal radiation near a stretching/shrinking sheet. *Mathematical Problems in Engineering* (special issue): 8822999.

Jabeen K, Mushtaq M, Akram R M (2020) Analysis of the MHD bboundary layer flow over a nonlinear sstretching sheet in a porous medium using semianalytical approaches. *Mathematical Problems in Engineering* 5(Feb): 3012854.

Kandasamy R, Mohammad R (2015) Radiative heat transfer on nanofluids flow over a porous convective surface in the presence of magnetic field. *Journal of Applied Mechanical Engineering* 4(4): 1–7.

Kumar P, Krishnan K (2018) Analysis of axisymmetric boundary layers. *Journal of Fluid Mechanics* 849(Jun): 927–941.

Mabood F, Pochai N, Shateyi S (2016) Stagnation point flow of nanofluid over a moving plate with convective boundary condition and magnetohydrodynamics. *Journal of Engineering* (4): 5874864.

Marneni N, Ashraf M, (2015) Mixed convection flow over a permeable stretching wedge in the presence of heat generation/absorption, viscous dissipation, radiation and ohmic heating. *Chemical Engineering Transactions* 45(Oct): 955–960.

Megahed AM, Reddy GM, Abbas W (2021) Modeling of MHD fluid flow over an unsteady stretching sheet with thermal radiation, variable fluid properties and heat flux. *Mathematics and Computers in Simulation* 185(Jan): 583–593.

Mustaqim MJ, Fadzilah MA, Arifin MA, Bachok N (2018) A stability analysis of stagnation-point flow of heat and mass transfer over a shrinking sheet with radiation and slip effects. *International Journal of Advanced Science Engineering and Technology* 6(Mar): 2321–8991.

Muthukumaran C, Bathrinathan K (2020) Mathematical modeling of mixed convection boundary layer flows over a stretching sheet with viscous dissipation in presence of suction and injection. *Symmetry* 12(11): 1754.

Nageeb A, Haroun H, Mondal S, Sibanda P (2017) Effects of thermal radiation of mixed convection in a MHD nanofluid flow over a stretching sheet using a spectral relaxation method. *International Journal of Mathematical and Computational Sciences* 11(2): 1–10.

Salleh SNA, Bachok N, Arifin MN, Ali MF (2019) Numerical analysis of boundary layer flow adjacent to a thin needle in nanofluid with the presence of heat source and chemical reaction. *Symmetry* 11(4): 543.

Shateyi S, Muzara H (2020) On numerical analysis of Carreau–Yasuda nanofluid flow over a non-linearly stretching sheet under viscous dissipation and chemical reaction effects. *Computation* 8(7): 1148.

Athens Journal of Sciences- Volume 8, Issue 4, December 2021 – Pages 309-332

On the Use of a Modified Intersection of Confidence Intervals (MICI$_H$) Kernel Density Estimation Approach

By Efosa Michael Ogbeide[*] & Joseph Erunmwosa Osemwenkhae[±]

Density estimation is an important aspect of statistics. Statistical inference often requires the knowledge of observed data density. A common method of density estimation is the kernel density estimation (KDE). It is a nonparametric estimation approach which requires a kernel function and a window size (smoothing parameter H). It aids density estimation and pattern recognition. So, this work focuses on the use of a modified intersection of confidence intervals (MICI$_H$) approach in estimating density. The Nigerian crime rate data reported to the Police as reported by the National Bureau of Statistics was used to demonstrate this new approach. This approach in the multivariate kernel density estimation is based on the data. The main way to improve density estimation is to obtain a reduced mean squared error (MSE), the errors for this approach was evaluated. Some improvements were seen. The aim is to achieve adaptive kernel density estimation. This was achieved under a sufficiently smoothing technique. This adaptive approach was based on the bandwidths selection. The quality of the estimates obtained of the MICI$_H$ approach when applied, showed some improvements over the existing methods. The MICI$_H$ approach has reduced mean squared error and relative faster rate of convergence compared to some other approaches. The approach of MICI$_H$ has reduced points of discontinuities in the graphical densities the datasets. This will help to correct points of discontinuities and display adaptive density.

Keywords: *approach, bandwidth, estimate, error, kernel density*

Introduction

Data density estimation provides estimates of the probability function from which a set of data is drawn. Density is better estimated from the data. In density estimation, the true density is unknown. One of the popular approaches is the multivariate kernel density estimation. It is a nonparametric estimation approach which requires a kernel function and a bandwidth (window size or smoothing parameter *H*). Researches from Little and Rubin (2002) and Wu et al. (2007) showed that observation with missing data has a density curve with points of discontinuities that can be corrected when the missing data are accounted for in the original data set. This can be done according to Little and Rubin (2002), via good imputation method, which has comparatively lower mean squared error.

When we consider the variable window sizes on the multivariate cluster kernel density estimation (MCKDE) and the intersection of confidence interval (ICI) approaches for estimating densities, we identified points for improvements, so that the methods could be adaptive to the MKDE. In most cases, the above methods

---

[*] Senior Lecturer, Department of Mathematics and Statistics, Ambrose Alli University, Nigeria.
[±] Professor, Department of Mathematics, University of Benin, Nigeria.

could lead to under fitting, an indication that the methods are often less optimal (Bowman and Azzalini 1997, Ogbeide et al. 2016). In this research work, we propose data-driven approaches that require only the knowledge of the use of pilot plots and the bandwidth sizes from the data set with a view to correcting the identified problems, while aiming for lower asymptotic mean integrated squared error (AMISE) and faster rates of convergence in the approaches. The aim of this study is basically on how to fit density to multivariate data sets observations. That is adaptive to the data at hand.

Researches have showed that that the performance of the kernel methods depends largely on the smoothing parameter (window width) but depends very little on the form of the kernel. According to Scott (1992) most times, analyses of the multivariate data are more prevalent in practice than the univariate cases. The crucial problem in the multivariate kernel density estimation (MKDE) is to select the window widths (bandwidth parameters) *H*. The window widths control the smoothness of the fitted density curve. The multivariate kernel density estimator that we are going to study is a direct extension of the univariate estimator. Let $X_1,...,X_n$ denote a d-variate random sample having a density f . We shall use the notation $X_i = (X_{i1},...,X_{in})^T$ to denote the X_i and a generic vector $x \in \Re^d$ has the representation $x = (x_1,...,x_d)^T$. The d-variate random sample $X_1,...,X_n$ drawn from f the kernel estimator evaluated at x is given by;

$$\hat{f}(X,H) = \frac{1}{n}\sum_{i=1}^{n} K_H(x - X_i) \tag{1.1}$$

where *n* is the sample size, and H is a symmetric positive definite *d* x *d* matrix called the window widths, the smoothing parameters or the bandwidth matrix, and $K_H(x) = |H|^{-\frac{1}{2}} K(H^{-\frac{1}{2}}x)$, $|\,.\,|$ stands for the determinant of H and K is d-variate kernel satisfying $\int k(x)dx = 1$, where the integral is over $\Re^d$ unless stated otherwise.

However, in chosing kernel to use, the gaussian kernel $K(u) = \frac{1}{\sqrt{2\pi}} \exp(-\frac{u^2}{2})$ is a popular choice among many kernels (Bowman and Azzalini 1997, Katkovnik and Shmulevich 2002, Yang et al. 2019, Jayasinghe and Jayasinghe 2021). The matrix *H* is a smoothing parameter and specifies the 'width' of the kernel around each sample point X_i. The adaptive (smoothing) methods are nonparametric density estimators that are sensitive to clustering/sparseness of sample values and other peculiarities, particularly at the tails. Here the smoothing parameter *H* varies, hence the "adaptive" techniques.

This work is based on the analysis of a new modified intersection of confidence intervals (MICI_H). This approach is demonstrated using the Nigerian crime rate data reported to the Police as reported by the National Bureau of Statistics. This MICI_H would be compared to some other known approaches.

Literature Review

There are several research works considering the problem of window size selection in kernel density estimation (see Abramson 1982, Silverman 1986, Wand and Jones 1995, Bowman and Azzalini 1997, Katkovnik and Shmulevich 2002, Wu et al. 2007, Zhang and Chan 2011, Ogbeide et al. 2016, Tang et al. 2020). Considering the variable window sizes on the multivariate cluster sampling kernel density estimate (MMCKDE) and the intersection of confidence interval (ICI) rule, points for improvements are identified, so that the methods could be more adaptive. Generally, nonparametric densities are constructed with optimal window widths. There exist some methods of estimating bandwidths in the multivariate kernel density. Some of these methods use a fixed window width. However, the approach that uses varied window widths in the course of density estimation which seems adaptive are few (Wu et al. 2007, Ogbeide et al. 2017). A review of available variable methods showed basically that the cross-validation, the plug-in bandwidths approaches or any subjective method (which are fixed smoothing approaches) (see Duong and Hazelton 2005). There is the cluster and the average cluster approach by Wu and Tsai (2004) and Wu et al. (2007) which are more data sensitive are used. The window width controls the smoothness of the fitted density curve. The true density is unknown.

When we consider the studies on variable window sizes on the average cluster approach and the intersection of confidence interval (ICI) methods applied to MKDE, one is tasked with how sensitive these methods are, and the errors committed using these methods? What are the effects when we extend them to multivariate kernel density? These questions led to the reasons for their modifications. We identified points for improvements, so that the methods could be more adaptive (Ogbeide el al. 2017). Currently, a variety of sophistication of the basic kernel estimator has been proposed, all pointing to the importance of adaptive kernel estimator (see Kathovnik and Shmulevich 2002, Salgado-Ugarte and Perez-Hernandez 2003, Zhang and Chan 2011, Yang et al. 2019, Ogbeide and Osemwenkhae 2019). The “adaptive” nature of the density estimate arises from the varying bandwidth used in the estimation process. If *h,* the bandwidth in (1.1) above, is “fixed” during estimation, we have the fixed kernel density estimation approach, but when it is allowed to vary all though the process of the estimation based on available data, we have the adaptive kernel method. A number of work considering the problem of kernel size selection exist (see Abramson 1982, Silverman 1986, Breiman et al. 1977, Hall 1990, Scott 1992, Wand and Jones 1995, Yang et al. 2019, Cortes and Sanz 2020, Ogbeide and Osemwenkhae 2021).

The most commonly used optimality criterion for selecting a bandwidth matrix is the mean integrated squared error (MISE)

$$MISE(H) = E\{\int [\underset{h}{\hat{f}}(X) - f(X)]^2 dX \qquad (2.1)$$

where $\int$ is a shorthand notation for $\int_{R^n}$ and X is in n Euclidean plane R^n.

According to Horova et al. (2008), this equation (2.1) is in general does not have a closed- form expression, so we result to its asymptotic approximation (AMISE). Hence (2.1) could be factored as

$$AMISE(H) \approx n^{-1}|H|^{-\frac{1}{2}} R(K) + \tfrac{1}{4} m_2(K)^2 (vec^T H)\psi_4 (vec^T H) \qquad (2.2)$$

where

- $R(K) = \int K(X)^2 dX$, with $R(K) = (4\pi)^{-\frac{d}{2}}$ when K is a normal kernel.
- $D^2 f \, is \, d \times d$ Hessian matrix of second order partial derivatives of f .
- $\psi_4 = \int (vecD^2 f(X))(vec^T D^2)dX$
- D is a diagonal matrix with elements $X_{11}, X_{22}, ..., X_{dd}$
- vec is the vector operator which stacks the columns of a matrix into a single vector.

We observed that the quality of the AMISE to the MISE is given according to Horova et al. (2008) by

$$MISE(H) = AMISE(H) + o(n^{-1}|H|^{-\frac{1}{2}} + trH^2) \qquad (2.3)$$

where o indicates the usual o notation. This implies that AMISE is a ‘good’ approximation of the MISE as $n \to \infty$. It has been shown that optimal bandwidth selector H has $H = O(n^{-\frac{2}{(d+4)}})$. According to Duong and Hazelton (2005) substituting this into equation (2.3) yields the optimal $MISE(H)$ order as $O(n^{-\frac{4}{(d+4)}})$. The big O notation is applied element-wise. So when $n \to \infty, MISE \to 0$. This implies the kernel density estimate converges in mean squared error and so also in probability to the true density f . According to Wand and Jones (1995) and Horova et al. (2008), they asserted that it was better to estimate optimal MISE element-wise. They further asserted that the ideal optimal bandwidth selector that is point wise adaptive is given by

$$H_{AMISE} = agr \min_{h \in \mathrm{H}} \widetilde{AMISE}(H) \qquad (2.4)$$

Since this ideal bandwidth selector contains the unknown density function f , that cannot be used directly. So some data density based approaches fixed the choice of bandwidth constant. However, we shall adopt point-wise adaptive bandwidth procedures in estimating densities.

The bandwidths used for the cluster approach by Wu et al. (2007) are optimal for information row/column (one dimensional) bandwidth per time in the multivariate data set. That is, it uses one bandwidth in the row or column during row/column cluster bandwidth selection. It is only row or column adaptive. Our approach is to make bandwidth selection to be data based on the smallest size of the row or column samples selections from the information matrix.

Clearly, in practice, one does not have access to the true density function *f(x)* which is to be estimated. Thus, a number of approaches can be taken for finding the bandwidth that will lead to better density estimation via varying the bandwidths (see Silverman 1986, Wand and Jones 1995, Katkovnik and Shmulevich 2002, Osemwenkhae and Ogbeide 2010). To this end, we modified the ICI approach in estimating density. The quality of the density estimates are assessed by comparing it to the density, obtained under the mean-squared error criterion. The error generated using these approach would be considered.

This work, present a data-driven methods that require the knowledge of pilot plot from optimal fixed window size and the variance of the estimate. This invariably reduces the amount of error at arriving at the "true density". This work is basically concerned with an approach of achieving adaptive multivariate kernel density estimation. The aim of this study includes how to fit kernel density to the Nigerian Crime data reported to the Police from 2002-2006 with missing observations as reported by National Bureau of Statistics (2009) using the available data case (ADC) and mode-related expectation adaptive maximization (MEAM) approaches. See Ogbeide (2018) for details on MEAM imputation approach for dataset when missing observation occurs. Imputation is the way (best possible way) of correcting a dataset with missing observation when it occurs in a given dataset via statistical means in order not to affect the inference from the available dataset.

Methodology

In this section, the proposed method of estimating densities is presented. This method is the modified intersection of confidence intervals (MICI_H) approach. According to Wand and Jones (1995) and Horova et al. (2008), they asserted that it was better to estimate optimal MISE element-wise. They further asserted that the ideal optimal bandwidth selector that is point wise adaptive. This method is a modification of the ICI approach to density estimate. This modified approach adjusts the amount of bandwidths using some idea from the kernel nearest neighbour estimation of the density to the multivariate data. Its smoothing parameter would be a $n \times d$ dimensional matrix obtained from forming relevant number of clusters in an information matrix. The Euclidean distance would be used to form bandwidth.

The MICI_H procedure is basically a minimization of $AMISE(H_i)$ with respect to H, where it is equivalent to the selection of optimal $h_{ij}\ in \{H_1, H_2, ...H_n\}$. Our data driven bandwidth matrix selector $\hat{H}$ is point wise data base selection approach. Its density uses a pilot plot in order to address identified problem(s).

$$\hat{H} = agr \min_{H_{D_j} \in \mathrm{H}} \widetilde{AMISE}(H). \qquad (3.1)$$

Assuming that

$$H = \{H_1 \leq H_2 \leq ....H_n\} \tag{3.2}$$

is a finite collection of window sizes, starting with a smallest $h_{ij} \in H$ and we determine a sequence of confidence intervals given by;

$$\left.\begin{aligned} &D_{ij} = [L_{ij}, U_{ij}], \quad i=1,...,n, j = 1, ..., d \\ &\bar{L}_{ij} = \hat{f}_{H_j}(X_i) - \beta.std\{\hat{f}_{H_j}(X_i)\} \\ &\underline{U}_{ij} = \hat{f}_{H_j}(X_i) + \beta.std\{\hat{f}_{H_j}(X_i)\} \end{aligned}\right\} \tag{3.3}$$

each h_{ij} corresponding to a value in $H_i \in H$. We assume the data at hand is normally distributed. Subjecting the data to normality, we propose $\beta = 1.06$ via normal reference rule.

And

$$H_{opt_i}(X) = [\frac{abs}{v}[\bar{L}_{ij}, \underline{U}_{ij}]] \tag{3.4}$$

where $abs[\bar{L}_{ij}, \underline{U}_{ij}] = \left|\bar{L}_{ij} - \underline{U}_{ij}\right| = \sqrt{\sum_{i=1}^{n}\sum_{j=1}^{d}\left|\bar{L}_{ij} - \underline{U}_{ij}\right|^2}$ (see Gray (1997) for lengths and distances' details).

Subjectively we adopt $v = 2$, considering pilot plots. Where v is a positive real number. The $MICI_H$ procedure is based on consideration of the intersection of the adjusted intervals D_{ij}, $1 \leq i \leq n \;\; and \;\; 1 \leq j \leq d$. We adopt the bandwidth sizes $H_{opt_j}(X)$;

$$H_{opt_i}(X) = [\frac{abs}{2}[\bar{L}_{ij}, \underline{U}_{ij}]] \text{ with } H_{opt_i}(X) \leq H_{opt_{i-1}}(X) \tag{3.5}$$

Consequently, substituting the bandwidths $H_{opt_i}(X)$ from equation (3.5) into the kernel density estimator $\hat{f}_{H_i}(X, H) = \frac{1}{n}\sum_{i=1}^{n} K_H(x - X_i)$ to obtain the density estimates. The algorithm is as follows:

Algorithm 1

```
Step 1    $\bar{L} \Leftarrow -\infty, \underline{U} \Leftarrow \infty$
Step 2    while $(\bar{L} \leq \underline{U})$ and $(i \leq J) do$
Step 3    $\bar{L}_{ij} \Leftarrow \underset{H_i}{\hat{f}}(X_i) - \beta.std\{\underset{H_i}{\hat{f}}(X_i)\}$
Step 4    $\underline{U}_{ij} \Leftarrow \underset{H_i}{\hat{f}}(X_i) + \beta.std\{\underset{H_i}{\hat{f}}(X_i)\}$
Step 5    $\bar{L}_{ij} \Leftarrow \max[\bar{L}, \bar{L}_{ij}], \underline{U}_j \Leftarrow \min[\underline{U}, \underline{U}_{ij}]$
Step 6    $i \Leftarrow i+1$
Step 7    $H_{opt_i}(x) = [\frac{abs}{2}[\bar{L}_{ij}, \underline{U}_{ij}]]$
Step 8    do $i \Leftarrow i+1$
Step 9    $H_{opt_i}(X) \leq H_{opt_{i-1}}(X)$
Step 10   compute $h_{ij}\, in\, H_i \in H$
Step 11   end while $(i = n)$.
```

Application/Results

The data for this study are drawn from the Nigerian National Bureau of Statistics Annual Abstract of Statistics published in the year 2009 on reported crime rate to the Police from 2002-2006 (www.nbs.gov.ng). The Tables of the density, error and convergence rate from the estimated bandwidths for the multivariate cluster sampling kernel density estimation (MCKDE) and the modified multivariate cluster sampling kernel density estimation (MMCKDE) and the MICI$_H$ approaches from the Nigerian crime rate data are presented. Tables 1-3 show the data and the evaluations results calculated from the Nigerian crime rate data as reported to the police.

This result favours the use of the MEAM approach for missing data imputation. This is because, the MEAM have relative lower error propagation and relative faster convergence rates for this dataset (see Ogbeide 2018). An approach with these criteria of lower error propagation and faster convergence rates is preferred according to Little and Rubin (2002). Imputation is applied here obviously because the actual dataset with missing crime cases in the year not available could not be traced as reported. This is so, that we could have 'clean' data to operate and estimate density. Next we estimate the dataset densities from the data.

Table 1. *Evaluated Estimates of Data with Missing Observation in Nigerian Crime Data Reported to the Police from 2002-2006 with Missing Observations as Reported by National Bureau of Statistics Annual Abstract of Statistics, 2009 Using the Available Data Case (ADC) and the Mode-Related Expectation Adaptive Maximization (MEAM) Approaches*

Offence	**Case**	**2002**	**2003**	**2004**	**2005**	**2006**
False Pretence/Cheating	ADC	7913	9508	-	9580	6395
	MEAM	7913	9508	9544	9580	6395
Unlawful Possession	ADC	3790	4142	5358	8772	8666
Receiving stolen property	ADC	1161	1289	2733	3892	7308
Arson	ADC	2005	1499	1289	1268	1010
Perjury	ADC	17	50	4	3	5
Gambling	ADC	199	148	-	631	473
	MEAM	199	148	390	631	473
Breach of trust	ADC	7055	7298	-	7967	5945
	MEAM	7055	7298	7633	7967	5945
Escape from custody	ADC	220	272	-	99	132
	MEAM	220	272	186	99	132
Local acts	ADC	2885	5171	-	3072	2610
	MEAM	2885	5171	4122	3072	2610
Others	ADC	3262	3322	-	891	914
	MEAM	3262	3322	2107	891	914

The densities estimates of the various bandwidths Nigerian minor crime rate data reported to the police from 2002-2006 with missing observations as reported by National Bureau of Statistics annual abstract of Statistics, 2009 with the MEAM imputation using the MCKDE, MMCKDE and MICI_H approaches for false pretence/cheating, unlawful possession, received stolen goods, arson, perjury, gambling, breach of peace, escape from custody, local acts and other crimes from Table 2 shows that the densities sums are closer to unity in the MICI_H than the other approaches. Furthermore, the bandwidth selections errors and the convergence rate from the estimated bandwidths for the multivariate cluster sampling kernel density estimation (MCKDE) and the modified multivariate cluster sampling kernel density estimation (MMCKDE) and the modified intersection of confidence intervals (MICI_H) approaches from the Nigerian crime rate data reported for the false pretence/cheating, unlawful possession, received stolen goods, arson, perjury, gambling, breach of peace, escape from custody, local acts and other crimes from Table 2 shows that the densities sums are closer to unity in the MICI_H than the other approaches The AMISE for MICI_H in false pretence/cheating, unlawful possession, received stolen goods, arson, perjury, gambling, breach of peace, escape from custody, local acts and other crimes were smaller than those of MMCKDE and MCKDE approaches.

Table 2. *Densities Estimates of the Various Bandwidths Nigerian Minor Crime Rate Data Reported to the Police from 2002-2006 with Missing Observations as Reported by National Bureau of Statistics Annual Abstract of Statistics, 2009 with the MEAM Imputation Using the MCKDE, MMCKDE and MICI*$_H$ *Approaches*

Offence	**Case:Densities**	**2002**	**2003**	**2004**	**2005**	**2006**	**Density sum**
False pretence/Cheating	Fixed H	0.1842	0.2214	0.2231	0.2231	0.1411	0.9929
	MCKDE	0.1891	0.2123	0.2237	0.2231	0.1465	0.9947
	MMCKDE	0.1842	0.2189	0.2231	0.2231	0.1489	0.9982
	MICI	0.1831	0.2201	0.2211	0.2278	0.1480	1.000
Unlawful possession	Fixed H	0.1321	0.1352	0.1765	0.2991	0.1566	0.8995
	MCKDE	0.1321	0.1352	0.1765	0.2991	0.211	0.9539
	MMCKDE	0.1233	0.1331	0.1744	0.2577	0.282	0.9705
	MICI	0.1233	0.1348	0.1744	0.2855	0.282	1.000
Receiving	Fixed H	0.0708	0.0787	0.1668	0.2399	0.3941	0.9503
	MCKDE	0.0811	0.0787	0.1668	0.2376	0.4023	0.9665
	MMCKDE	0.0811	0.0768	0.1881	0.2376	0.4147	0.9983
	MICI	0.0708	0.0787	0.1667	0.2376	0.4461	0.9999
Arson	Fixed H	0.2514	0.1576	0.1322	0.1311	0.3195	0.9918
	MCKDE	0.2514	0.1713	0.1314	0.1231	0.3171	0.9943
	MMCKDE	0.2514	0.1713	0.1322	0.1244	0.3192	0.9985
	MICI	0.2412	0.1611	0.1371	0.1413	0.3192	0.9999
Perjury	Fixed H	0.2151	0.6101	0.0503	0.0366	0.0633	0.9754
	MCKDE	0.2198	0.6088	0.0506	0.0379	0.0633	0.9804
	MCKDE	0.2198	0.6198	0.0531	0.0399	0.0633	0.9959
	MICI	0.2156	0.6311	0.0501	0.0401	0.0631	1.0000
Gambling	Fixed H	0.1081	0.0799	0.2001	0.3392	0.257	0.9843
	MCKDE	0.1083	0.0795	0.2116	0.3388	0.257	0.9952
	MMCKDE	0.1083	0.0801	0.2116	0.3428	0.257	0.9998
	MICI	0.1081	0.0804	0.2116	0.3428	0.257	0.9999
Breach of Peace	Fixed H	0.1965	0.2033	0.2102	0.2219	0.1656	0.9975
	MCKDE	0.1968	0.2001	0.2102	0.2219	0.1656	0.9946
	MMCKDE	0.1968	0.2033	0.2122	0.2219	0.1656	0.9998
	MICI	0.1965	0.2033	0.2126	0.2219	0.1656	0.9999
Escape from custody	Fixed H	0.2422	0.2887	0.2041	0.1089	0.1453	0.9892
	MCKDE	0.2476	0.2887	0.2041	0.1089	0.1453	0.9946
	MMCKDE	0.2476	0.2939	0.2041	0.1089	0.1453	0.9998
	MICI	0.2422	0.2994	0.2041	0.1089	0.1453	0.9999
Local Acts	Fixed H	0.1615	0.2833	0.2289	0.1701	0.1461	0.9899
	MCKDE	0.1615	0.2833	0.2298	0.1701	0.1461	0.9908
	MMCKDE	0.1615	0.2882	0.2308	0.172	0.1461	0.9986
	MICI	0.1615	0.2895	0.2308	0.172	0.1461	0.9999
Others	Fixed H	0.3108	0.2998	0.2007	0.0823	0.0871	0.9807
	MCKDE	0.3108	0.2998	0.2007	0.0849	0.0871	0.9833
	MMCKDE	0.3108	0.3123	0.2007	0.0849	0.0871	0.9958
	MICI	0.3108	0.3165	0.2007	0.0849	0.0871	1.0000

The h^* (which is the error in relation to the fixed optimal bandwidth value), $AMISE^*$ and the convergence rates of methods are given below. Table 3 shows that there are reduced relative errors in the h^* (which is the error in relation to the fixed optimal bandwidth value) and $AMISE^*$ in the proposed methods. The presented MICI$_H$ have faster convergence rates compared to the other versions. That is, the MICI$_H$ has lower error propagation and faster convergence rates when used to estimates the Nigerian crime rate data reported to the police. This is when compared to the fixed optimal H, MCKDE and the MMCKDE approaches. Generally, the AMISE shows the difference between the "true density" and the estimated density. The AMISE for $MICI_H$ is smaller than that of MMCKDE and MCKDE approaches.

Table 3. *Bandwidth Selections Errors and the Convergence Rate from the Estimated Bandwidths for the Multivariate Cluster Sampling Kernel Density Estimation (MCKDE) and the Modified Multivariate Cluster Sampling Kernel Density Estimation (MMCKDE) and the* $MICI_H$ *Approaches from the Nigerian Crime Rate Data Reported*

Item(s)	**Approach**	**Mean**	**Convergence Rate**	**Variance**	**δ**	**h^***	**$AMISE^*$**
False pretence/ Cheating	MCKDE	24.4540	1.0907	459.1561	21.4279	10.3869	2.1828×10^{-1}
	MMCKDE	17.4540	1.6860	116.7849	10.8067	5.2384	1.2624×10^{-1}
	$MICI_H$	20.1530	1.4255	36.4999	6.0425	2.9828	7.9280×10^{-2}
Unlawful possession	MCKDE	27.3920	1.0000	559.0200	23.6436	11.4609	2.3616×10^{-1}
	MMCKDE	24.3020	1.1991	179.3006	13.3903	6.4907	1.4985×10^{-1}
	$MICI_H$	17.6293	1.7740	37.6934	6.1334	2.9730	8.0243×10^{-2}
Receiving stolen Property	MCKDE	33.1460	1.1215	489.4700	22.1239	10.7242	2.2394×10^{-1}
	MMCKDE	30.5800	1.1625	310.8864	17.6319	8.5468	1.8676×10^{-1}
	$MICI_H$	30.2394	1.1814	109.9777	10.4870	5.0834	1.2324×10^{-1}
Arson	MCKDE	4.3780	1.0285	10.3800	3.2218	1.5617	4.7943×10^{-2}
	MMCKDE	3.4910	1.3502	1.3664	1.1689	0.5661	2.1304×10^{-2}
	$MICI_H$	3.5853	1.4018	0.1190	0.3449	0.1678	8.0242×10^{-3}
Perjury	MCKDE	0.3340	1.0000	0.1400	0.3741	0.1813	8.5632×10^{-3}
	MMCKDE	0.2380	1.5881	0.0343	0.1852	0.0897	4.8793×10^{-3}
	$MICI_H$	0.2474	1.5176	0.0177	0.1330	0.0644	3.743×10^{-3}
Gambling	MCKDE	3.0290	0.5795	1.1800	1.0862	0.5265	2.0089×10^{-2}
	MMCKDE	3.0209	0.5829	1.0419	1.0207	0.4947	1.9114×10^{-2}
	$MICI_H$	1.5088	1.7087	0.1698	0.4120	0.1997	9.2505×10^{-3}
Breach of Peace	MCKDE	14.7749	1.1058	164.1300	12.8113	6.2101	1.4465×10^{-1}
	MMCKDE	12.0539	1.4273	72.6648	8.5243	4.1320	1.0441×10^{-1}
	$MICI_H$	10.9229	1.6005	28.8064	5.371	2.6016	7.2117×10^{-2}
Escape from custody	MCKDE	1.1721	1.1206	0.1000	0.3162	0.1532	7.4854×10^{-3}
	MMCKDE	1.1602	1.1379	0.0432	0.2078	0.1007	5.5851×10^{-3}
	$MICI_H$	0.7484	1.9233	0.5404	0.2324	0.1126	5.3501×10^{-3}
Local acts	MCKDE	22.5310	1.0000	134.0300	11.5771	5.6118	1.3339×10^{-1}
	MMCKDE	18.6925	1.3152	28.3639	5.3447	2.5907	7.1876×10^{-2}
	$MICI_H$	15.3892	1.6653	28.3639	5.3257	2.5815	7.1671×10^{-2}
Others	MCKDE	14.7482	0.7516	78.3682	8.8525	4.2911	1.0762×10^{-1}
	MMCKDE	10.7482	1.2189	62.2800	7.8919	3.8254	9.8171×10^{-2}
	$MICI_H$	10.6617	1.2665	33.3262	5.7728	2.7982	7.6446×10^{-2}

The estimated bandwidth selection errors and the convergence rates from the Nigerian crime rate data set with missing observations, via the various methods favour the use of the $MICI_H$ approach over the other approaches. This is because its bandwidth errors are smaller as well as having higher convergence rate. The MMCKDE has some improvement over the MCKDE approach. These can be seen in Tables 2-3. Generally, the AMISE shows the difference between the "true density" and the estimated density. The AMISE for $MICI_H$ is smaller than that of MMCKDE and MCKDE approaches. Graphical densities displays are presented next.

False Pretence/Cheating

Figure 1a. *Graphical Density Estimates for False Pretence/Cheating Using the Fixed H Approach*

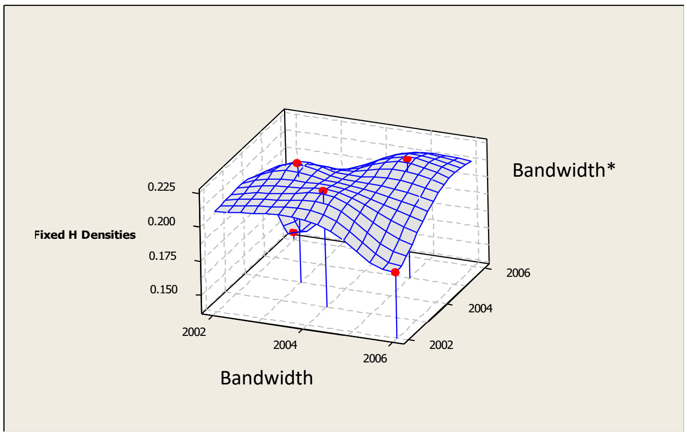

Figure 1b. *Graphical Density Estimates for False Pretence/Cheating Using the MCKDE Approach*

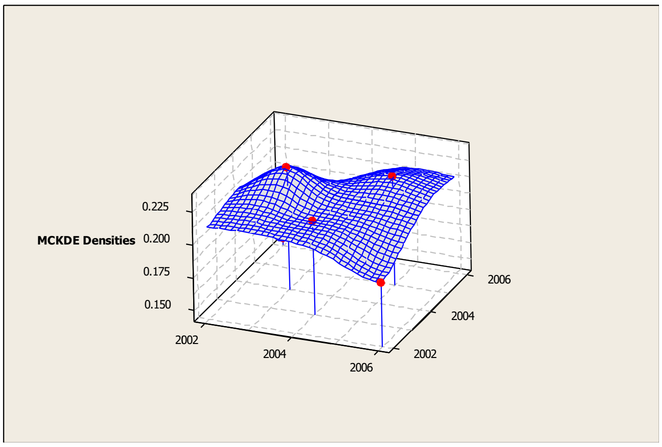

Figure 1c. *Graphical Density Estimates for False Pretence/Cheating Using the MMCKDE Approach*

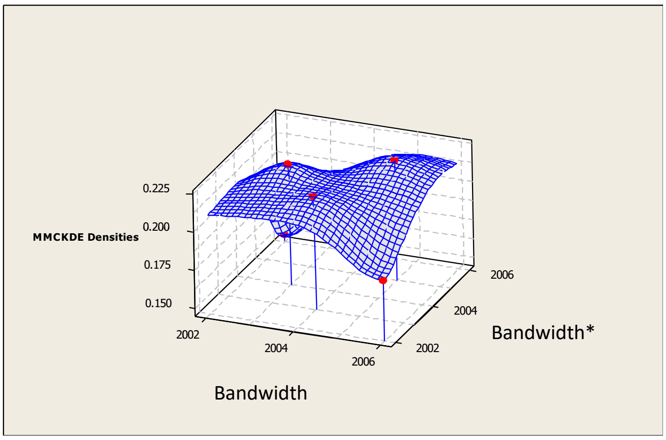

Figure 1d. *Graphical Density Estimates for False Pretence/Cheating Using the MICI$_H$ Approach*

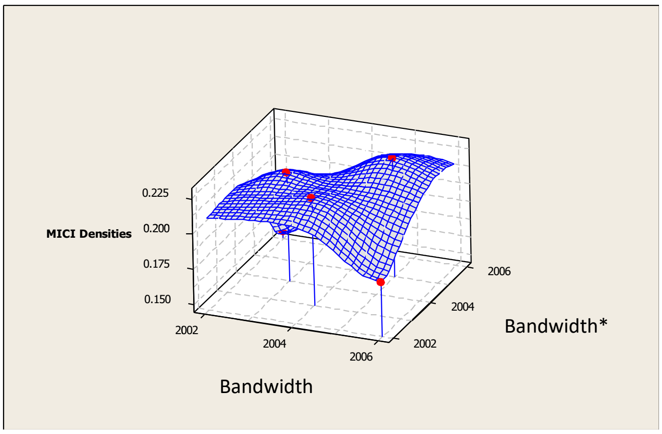

Unlawful Possession

Figure 2a. *Graphical Density Estimates for Unlawful Possession Using the Fixed H Approach*

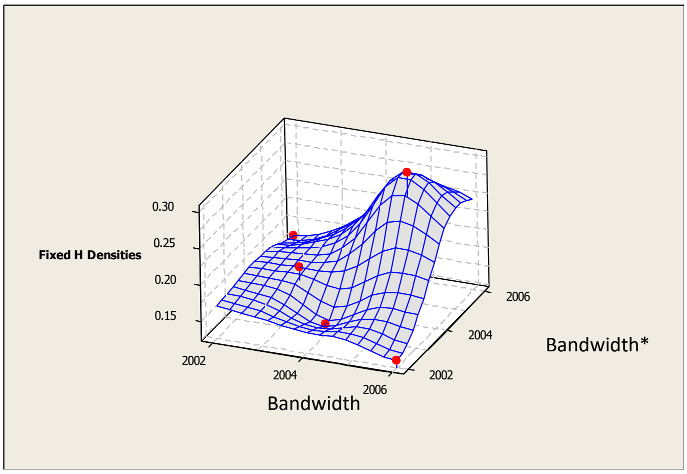

Figure 2b. *Graphical Density Estimates for Unlawful Possession Using the MCKDE Approach*

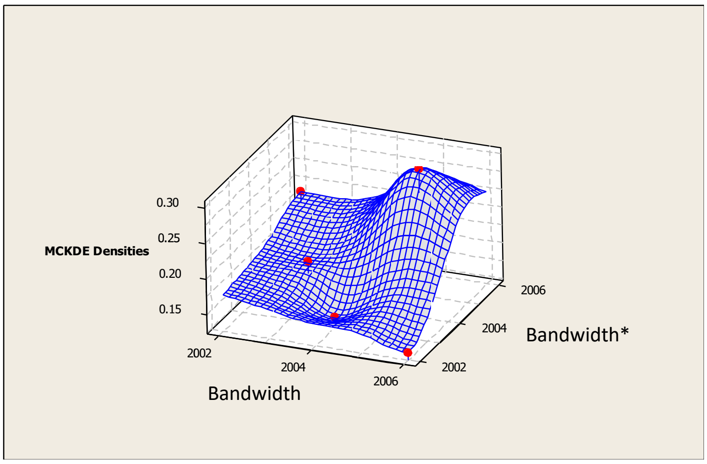

Figure 2c. *Density Graphical Density Estimates for Unlawful Possession Using the MMCKDE Approach*

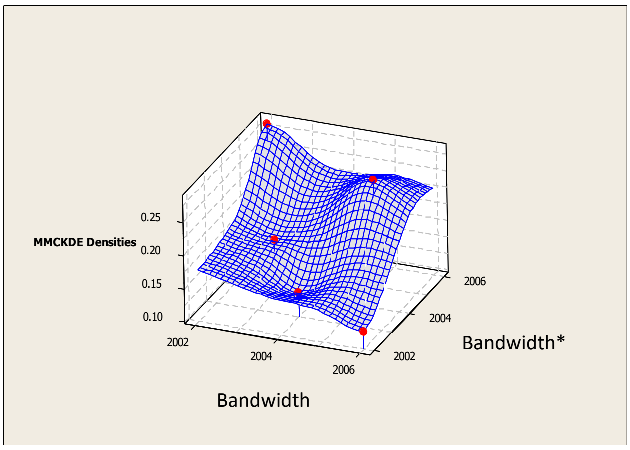

Figure 2d. *Graphical Density Estimates for Unlawful Possession Using the MICI$_H$ Approach*

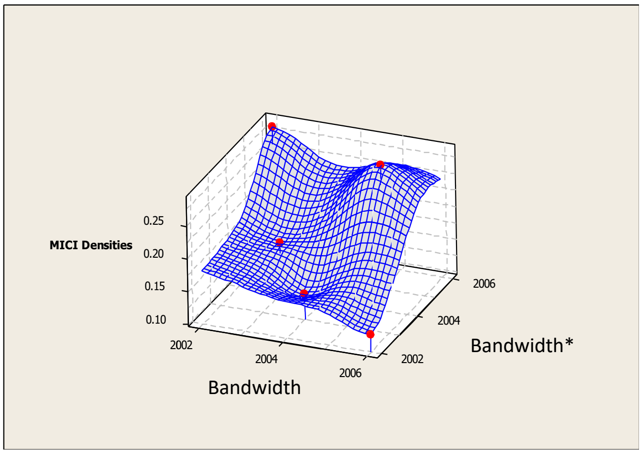

Receiving Stolen Properties

Figure 3a. *Graphical Density Estimates for Receiving Stolen Property Using the Fixed H Approach*

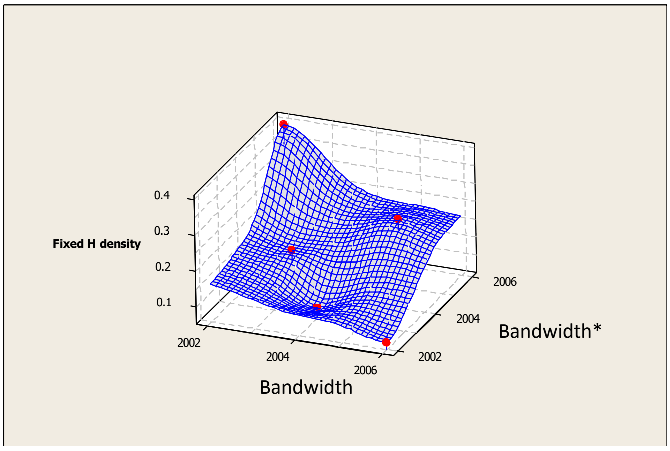

Figure 3b. *Graphical Density Estimates for Receiving Stolen Property Using the MCKDE Approach*

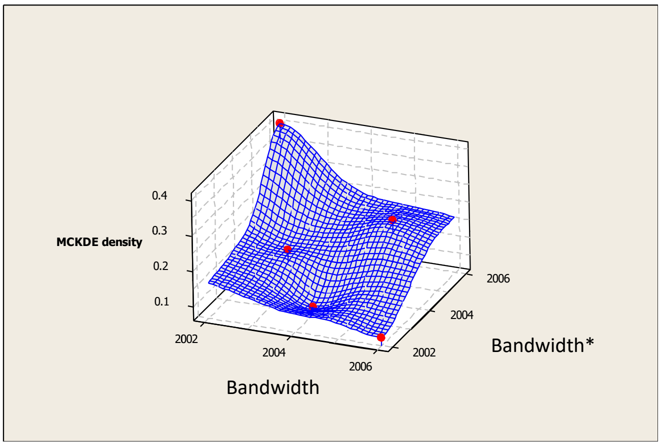

Figure 3c. *Graphical Density Estimates for Receiving Stolen Property Using the MMCKDE Approach*

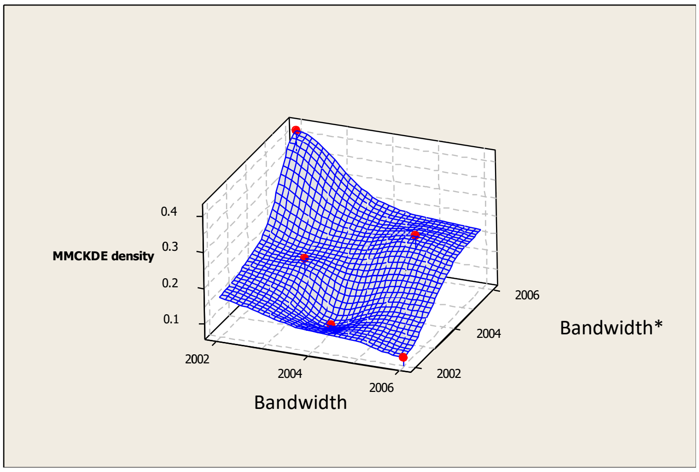

Figure 3d. *Graphical Density Estimates Receiving Stolen Property Using the MICI*$_H$ *Approach*

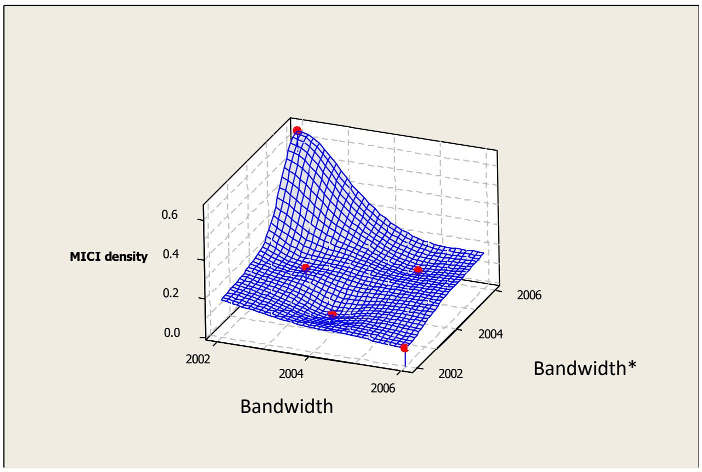

Arson

Figure 4a. *Graphical Density Estimates for Arson Using the Fixed H Approach*

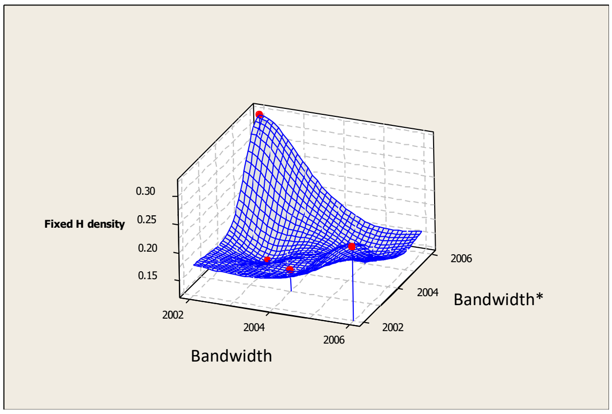

Figure 4b. *Graphical Density Estimates for Arson Using the MCKDE Approach*

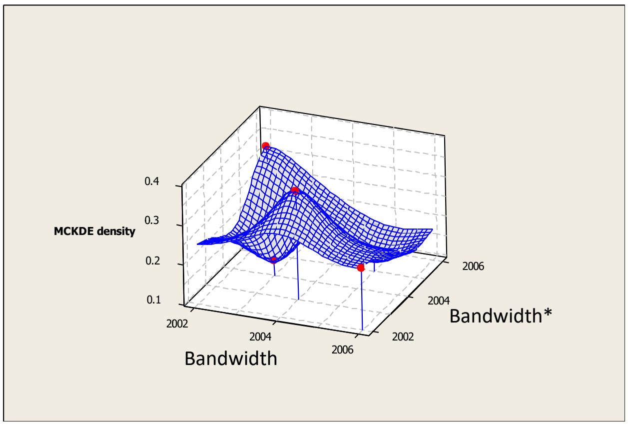

Figure 4c. *Graphical Density Estimates for Arson Using the MMCKDE Approach*

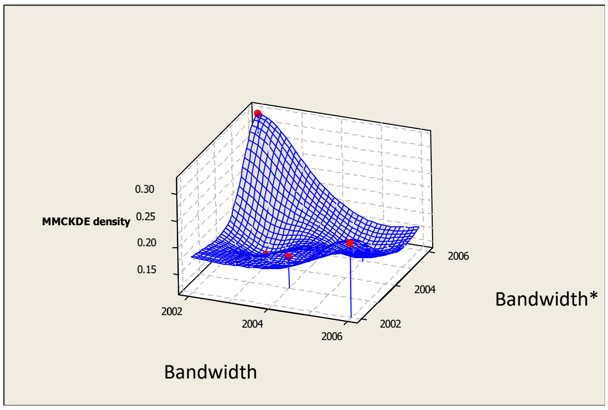

Figure 4d. *Graphical Density Estimates for Arson Using the* $\textit{MICI}_H$ *Approach*

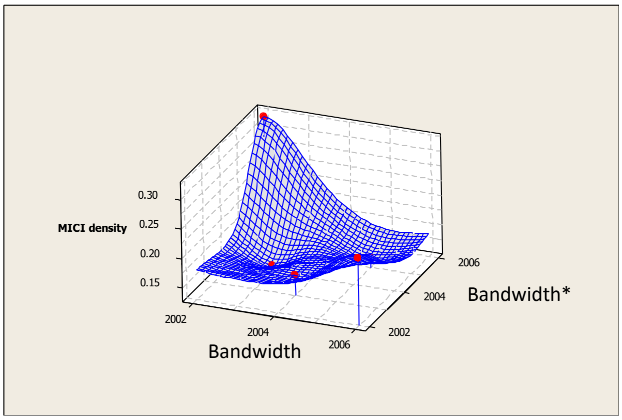

Perjury

Figure 5a. *Graphical Density Estimates for Perjury Using the Fixed H Approach*

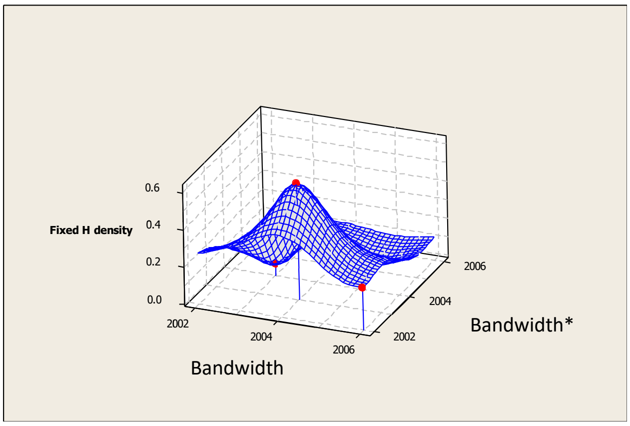

Figure 5b. *Graphical Density Estimates for Perjury Using the MCKDE Approach*

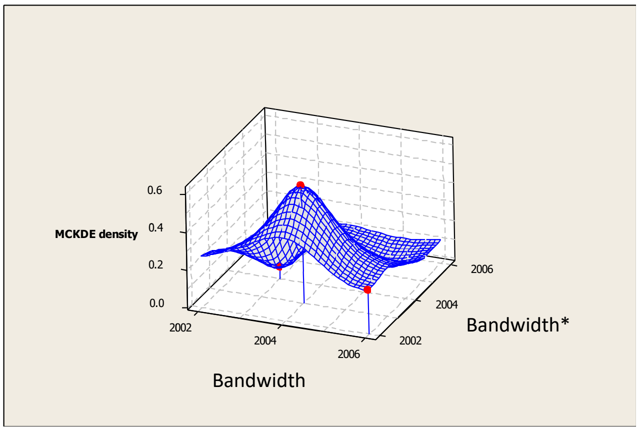

Figure 5c. *Graphical Density Estimates for Perjury Using the MMCKDE Approach*

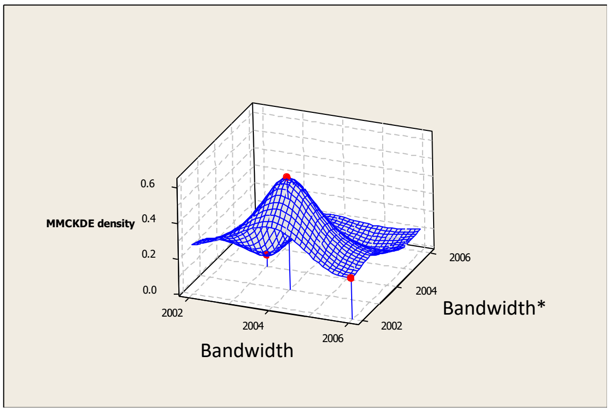

Figure 5d. *Graphical Density Estimates for Perjury Using the MICI$_H$ Approach*

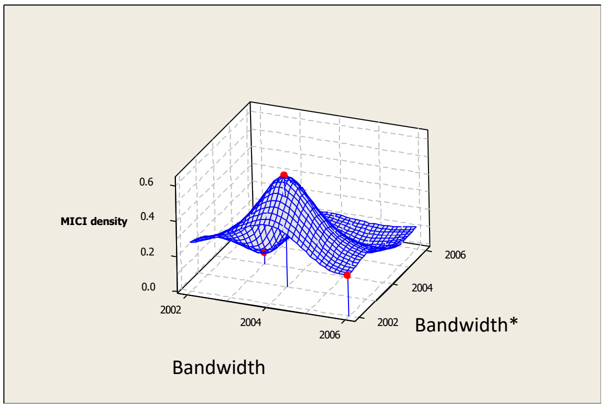

Gambling

Figure 6a. *Graphical Density Estimates for Gambling Using the Fixed H Approach*

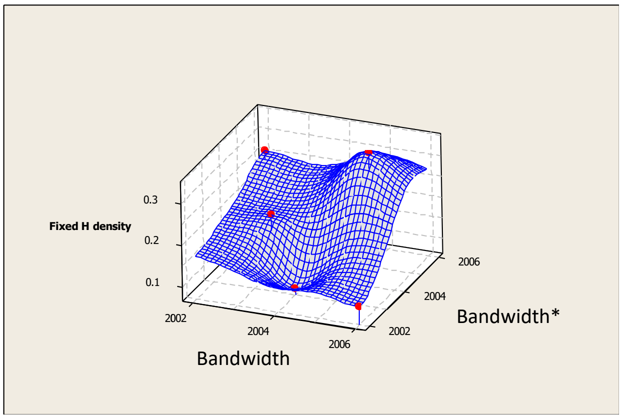

Figure 6b. *Graphical Density Estimates for Gambling Using the MCKDE Approach*

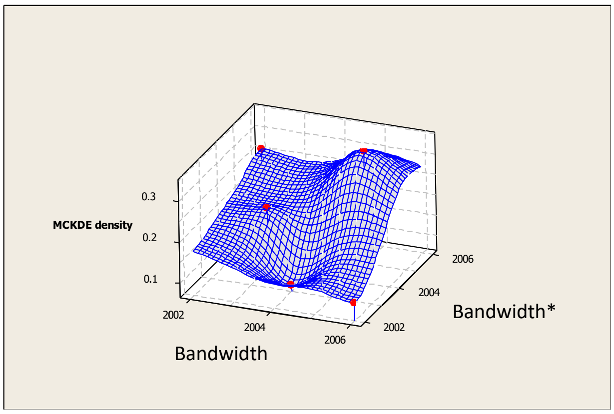

Figure 6c. *Graphical Density Estimates for Gambling Using the MMCKDE Approach*

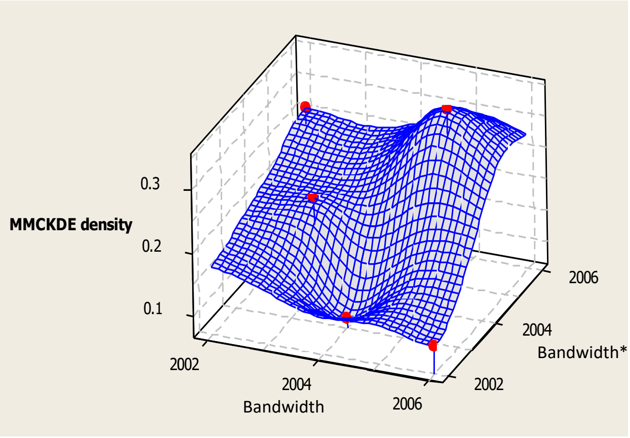

Figure 6d. *Graphical Density Estimates for Gambling Using the MIC$_H$ Approach*

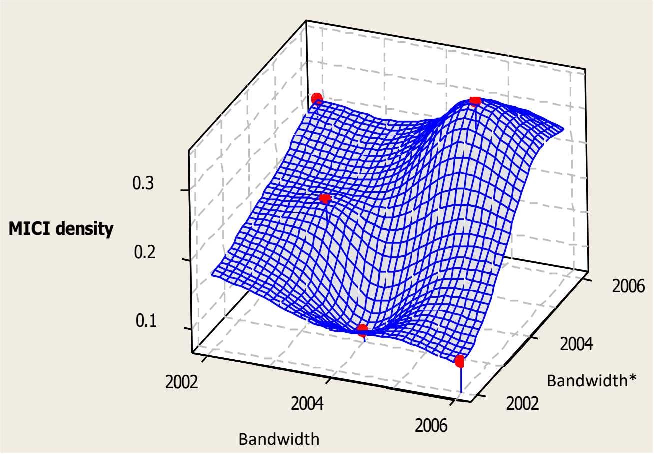

Breach of Peace

Figure 7a. *Graphical Density Estimates for Breach of Peace Using the MCKDE Approach*

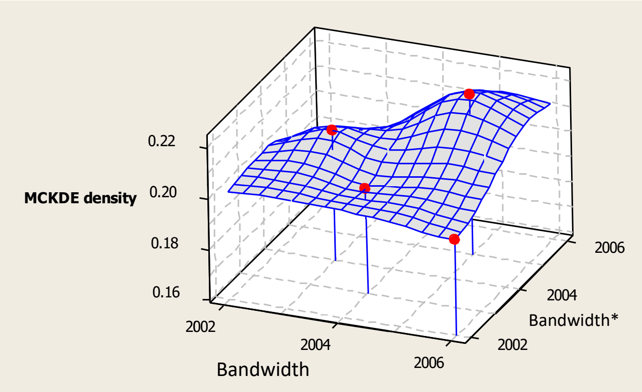

Figure 7b. *Graphical Density Estimates for Breach of Peace Using the Fixed H Approach*

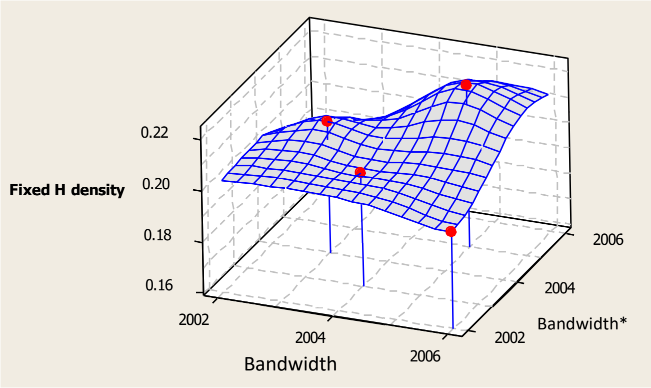

Figure 7c. *Graphical Density Estimates for Breach of Peace Using the MMCKDE Approach*

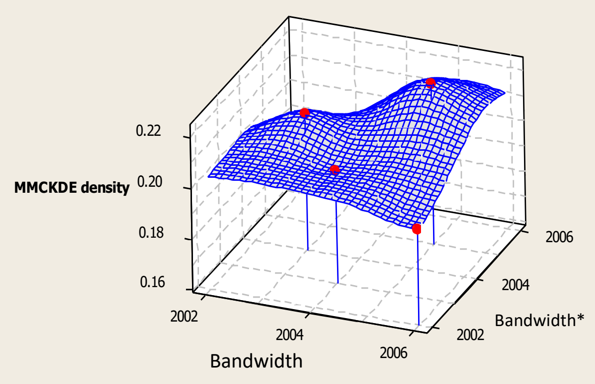

Figure 7d. *Graphical Density Estimates for Breach of Peace Using the MICI$_H$ Approach*

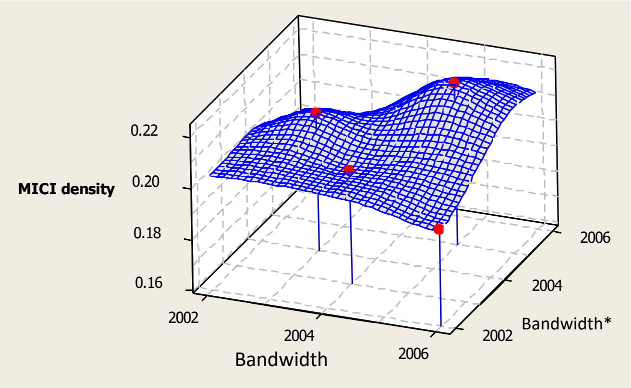

Escape from Custody

Figure 8a. *Graphical Density Estimates for Escape from Custody Using the fixed H Approach*

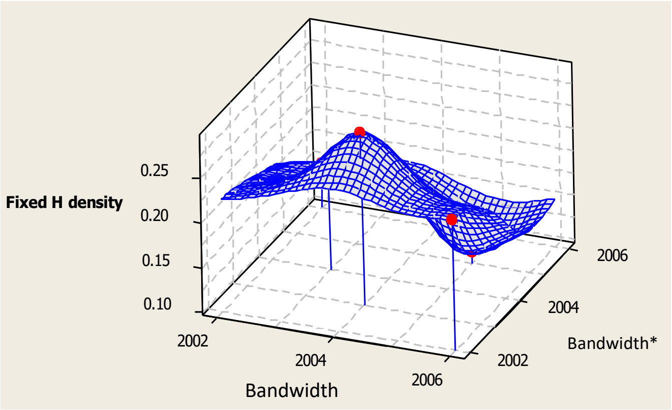

Figure 8b. *Graphical Density Estimates for Escape from Custody Using the MCKDE Approach*

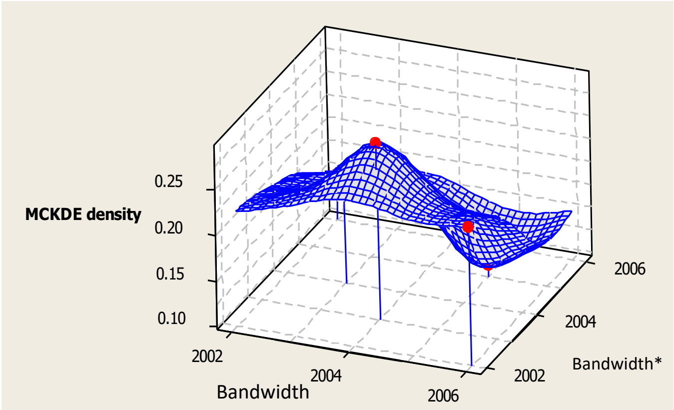

Figure 8c. *Graphical Density Estimates for Escape from Custody Using the MMCKDE Approach*

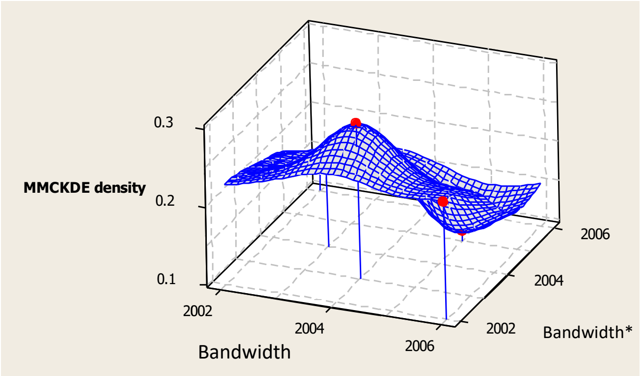

Figure 8d. *Graphical Density Estimates for Escape from Custody Using the $MICI_H$ Approach*

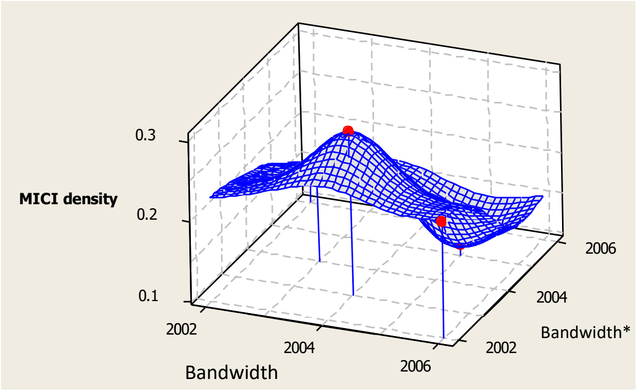

Local Acts Crime

Figure 9a. *Graphical Density Estimates for Local Acts Crime Using the fixed H Approach*

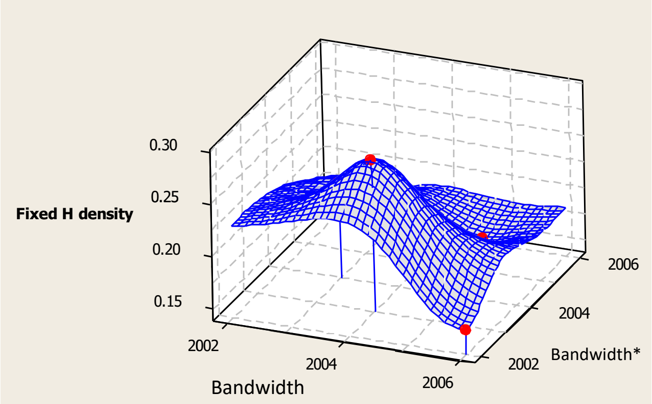

Figure 9b. *Graphical Density Estimates for Local Acts Crime Using the MCKDE Approach*

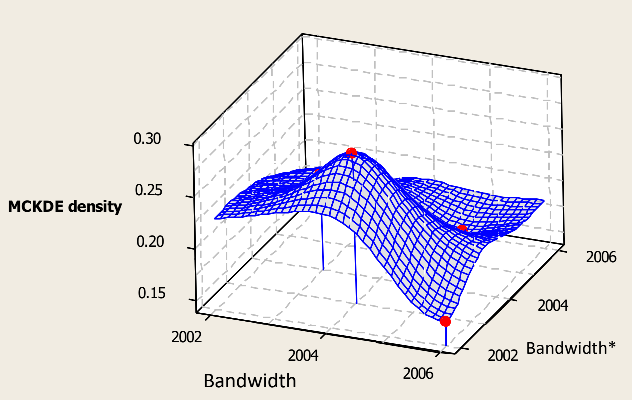

Figure 9c. *Graphical Density Estimates for Local Acts Crime Using the MMCKDE Approach*

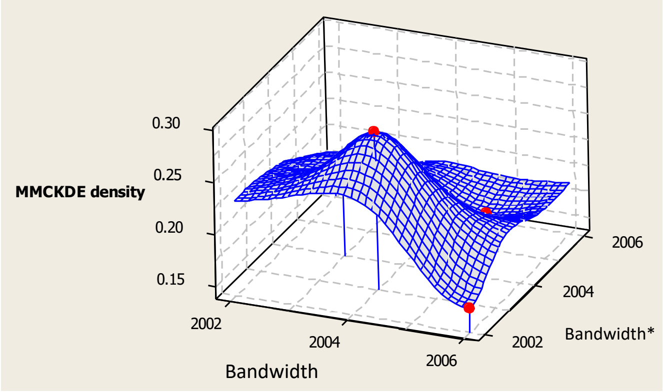

Figure 9d. *Graphical Density Estimates for Local Acts Crime Using the MICI$_H$ Approach*

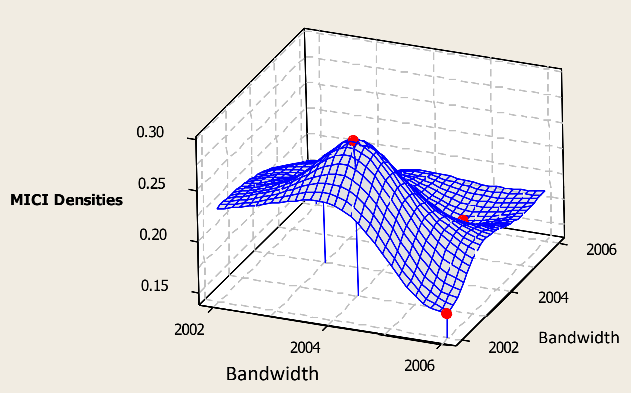

Other Crimes

Figure 10a. *Graphical Density Estimates for Other Crimes Using the Fixed H Approach*

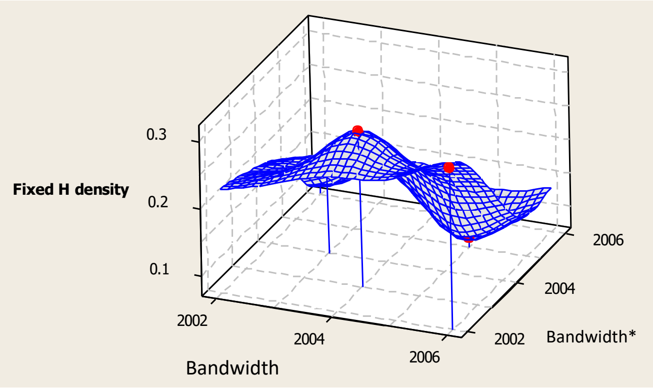

Figure 10b. *Graphical Density Estimates for Other Crimes Using the MCKDE Approach*

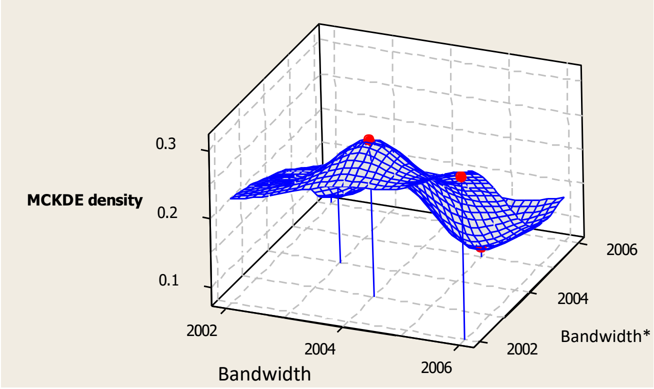

Figure 10c. *Graphical Density Estimates for Other Crimes Using the MMCKDE Approach*

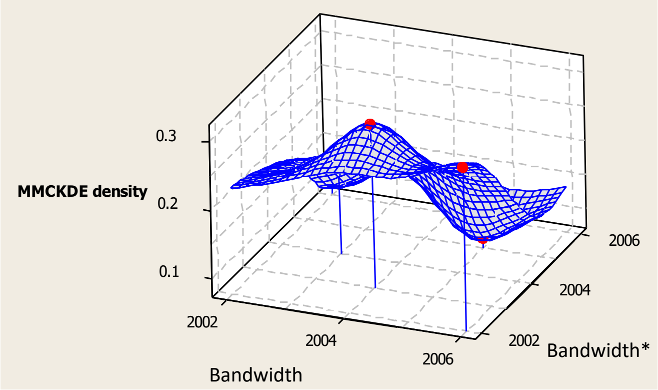

Figure 10d. *Graphical Density Estimates for Other Crimes Using the MICI$_H$ Approach*

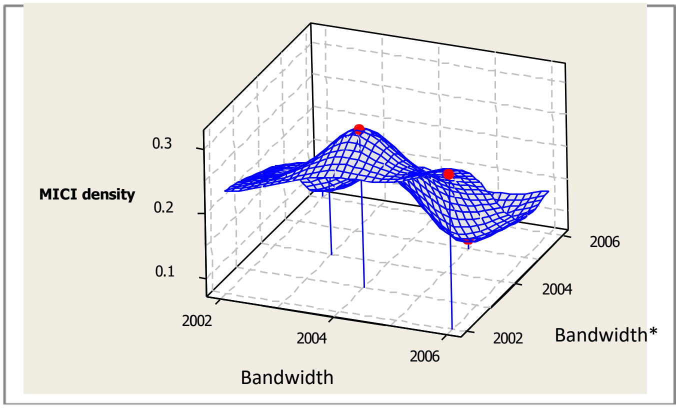

The various approaches have identifiable differences from Figures 1a-10d, using the fixed H, MCKDE, MMCKDE and MICI$_H$ for the dataset in Nigerian crime rate data reported by the Nigerian National Bureau of Statistics. There are visible signs of discontinuities in the fixed H and the MCKDE graphical densities estimates of the data sets. These are seen in Figures 1a-10d as well as in Tables 2-3. The proposed approach of MICI$_H$ has reduced points of discontinuities in the graphical densities of the datasets compared to the fixed H, MCKDE, MMCKDE approaches. This MICI$_H$ approach helps to correct points of discontinuities and display adaptive density. The density from the fixed H bandwidth could serves as a pilot guide. The density from the fixed H bandwidth is by no means as adaptive as the variable bandwidths approaches.

Figure 11. *Density for False Pretence/Cheating Using the Fixed H, MCKDE, MMCKDE and MICI*$_H$ *Approaches*

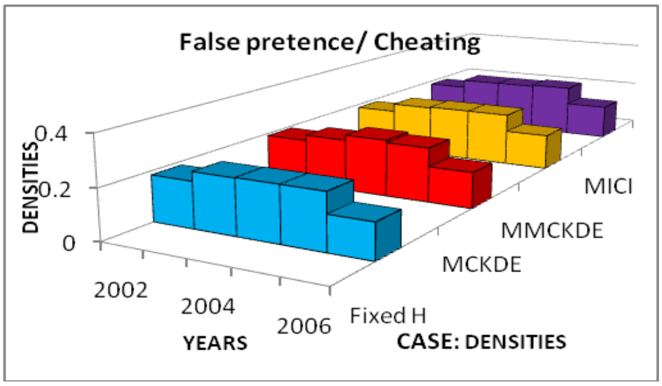

Figure 12. *Density for Unlawful Possession Using the Fixed H, MCKDE, MMCKDE and MIC*$_H$ *Approaches*

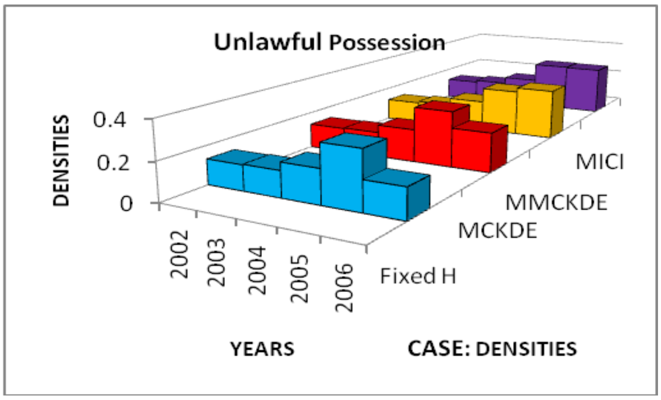

Figure 13. *Density for Receiving Stolen Property Using the Fixed H, MCKDE, MMCKDE and MIC*$_H$ *Approaches*

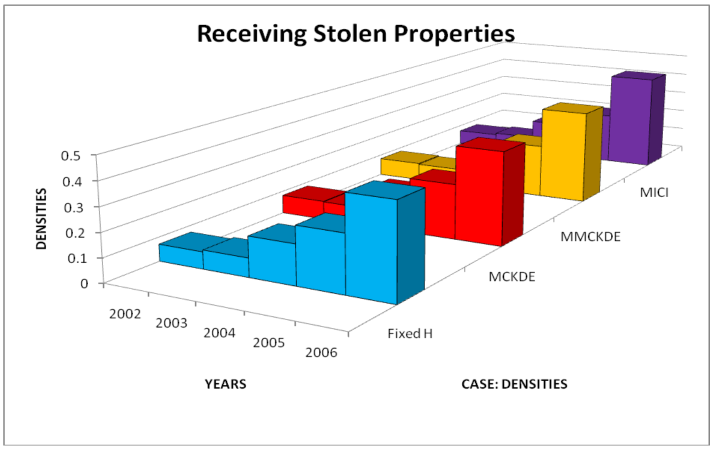

Figure 14. *Density for Arson Using the Fixed H, MCKDE, MMCKDE and MIC*$_H$ *Approaches*

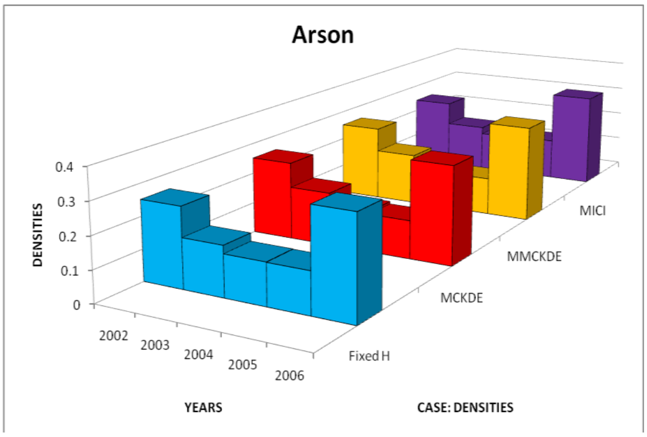

Figure 15. *Density for Perjury Using the Fixed H, MCKDE, MMCKDE and MICI*$_H$ *Approaches*

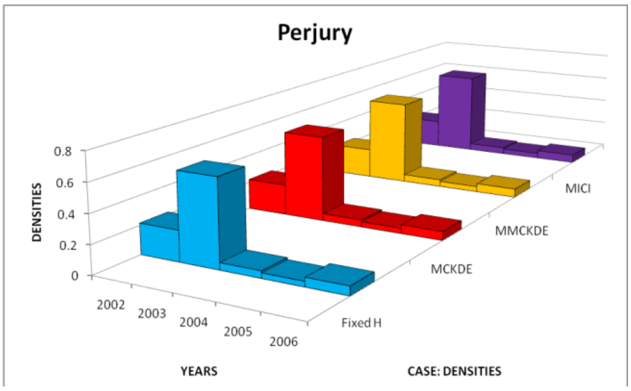

Figure 16. *Density for Gambling Using the Fixed H, MCKDE, MMCKDE and MICI*$_H$ *Approaches*

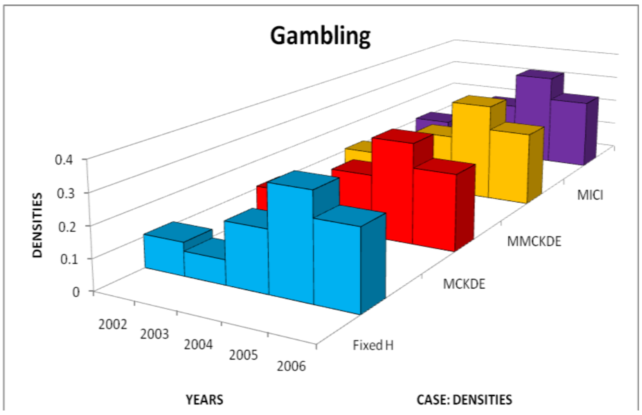

Figure 17. *Density for Breach of Peace Using the Fixed H, MCKDE, MMCKDE and MICI Approaches*

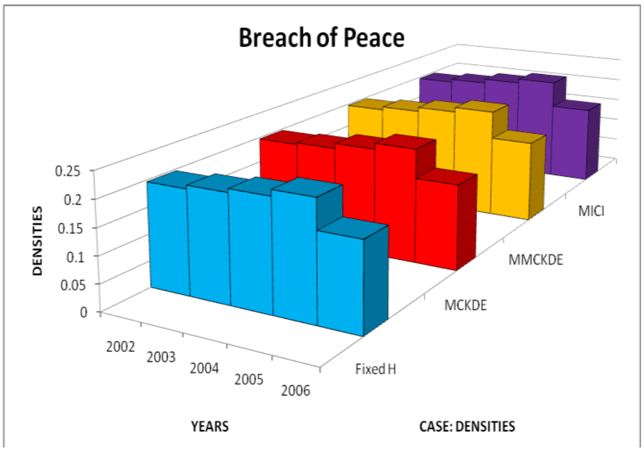

Figure 18. *Density for Escape from Custody Using the Fixed H, MCKDE, MMCKDE and MICI$_H$ Approaches*

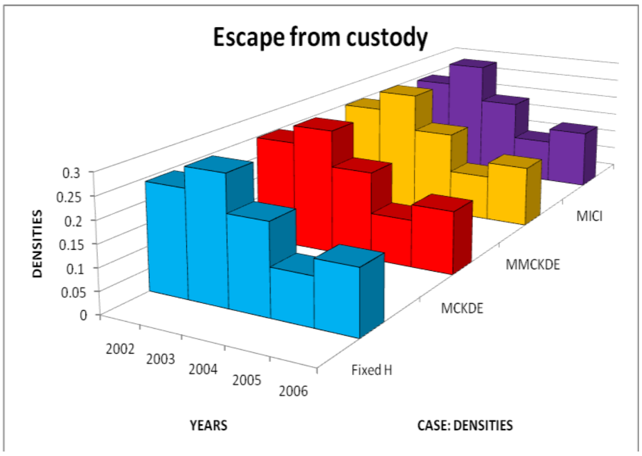

Figure 19. *Density for Local Acts Using the Fixed H, MCKDE, MMCKDE and MICI$_H$ Approaches*

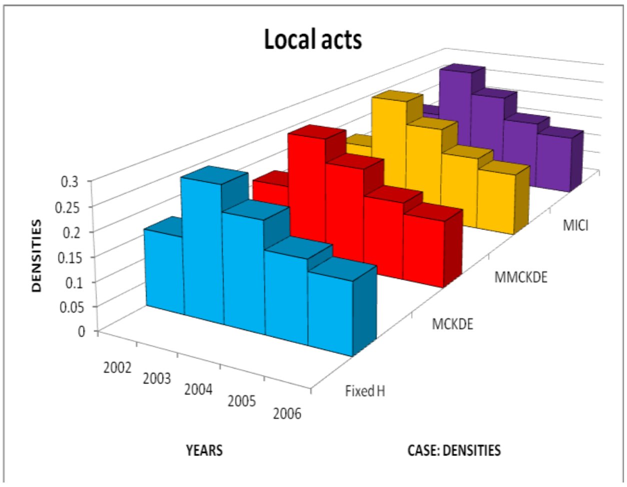

Figure 20. *Density for Other Crimes Using the Fixed H, MCKDE, MMCKDE and MICI$_H$ Approaches*

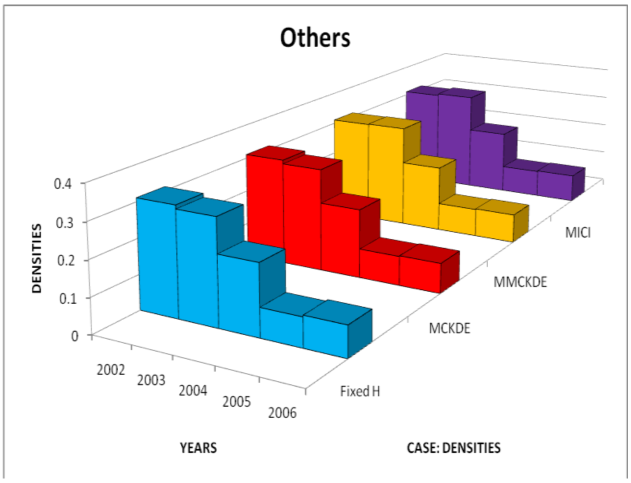

The various approaches have identifiable differences from Figures 11-20, using the fixed H, MCKDE, MMCKDE and MICI$_H$ for the Nigerian crime rate data reported.

The MICI$_H$ scheme produces better density estimation when compared to the fixed bandwidths H, MCKDE and MMCKDE approaches seeing the figures. This is a good approach because it is data sensitive and does not unfit or over fit the density curves as the case may be. This contributes significantly to the density estimates by showing more hidden features of the density. This approach provides and uses full bandwidths matrix from the data for the multivariate kernel density estimation. This approach has additional procedures in the choice and application of the smoothing parameters (bandwidths H) to multivariate density estimation. MICI$_H$ generate full bandwidths matrices. The cost of these steps brings about the adaptive density to be constructed. A study for less time efficient approach should be the aim of further research that vary the bandwidths selection based on the data in kernel density estimation.

The MICI$_H$ approach in estimating density is presented. The quality of the density estimates was assessed; comparing it with the densities obtained using the mean-squared error criterion showed some improvements. The crime data distribution/density is always needed for crime prevention and comparative analysis from time to time. The MICI$_H$ will be of practical help in discovery of the real dataset density.

Conclusions

This work presents a modified intersection of confidence intervals (MICI$_H$) approach to estimate density. It is a nonparametric statistics approach. It can used to estimate and fit density for a dataset, particularly for large size data. The Nigerian crime rate data reported to the Police was used to demonstrate the approach. This approach in the multivariate density estimation is based on the data. The quality of the estimates obtained of the MICI$_H$ approach showed some improvements over the existing methods. The MICI$_H$ approach has reduced mean squared error and relative faster rate of convergence compared to some other approaches. The approach of MICI$_H$ has reduced points of discontinuities in the graphical densities the datasets. They help to correct points of discontinuities and display adaptive density compared to the fixed H, MCKDE and MMCKDE approaches.

References

Abramson IS (1982) Arbitrariness of the pilot estimate in adaptive kernel methods. *Journal of Multivariate Analysis* 12(4): 562–567.

Bowman AW, Azzalini A (1997) Applied smoothing techniques for data analysis. Oxford: Clarendon Press.

Breiman L, Meisel W, Purcell E (1977) Variable kernel estimates of multivariate density. *Technometrics* 19(2): 135–144.

Cortes J-CL, Sanz JM (2020) Improving kernel methods for density estimation in random differential equations problems. *Mathematical and Computational Application* 25(2): 33.

Duong T, Hazelton ML (2005) Convergence rates for unconditional bandwidth matrix selector for multivariate kernel density estimation. *Journal of Multivariate Analysis* 93(2): 417–433.

Gray A (1997) *The intuitive idea of distance on surfaces in 'modern differential geometry of curves and surfaces with mathematica'*. 2nd Edition. Boca Ration, FL: CRC Press.

Hall P (1990) On the bias of variable bandwidth curve estimators. *Biometrika* 77(3): 529–536.

Horova I, Kolacek J, Zelinka J, Vopatova K (2008) *Bandwidth choice for kernel density estimates*. Yokohama, Japan: IASC.

Jayasinghe DY, Jayasinghe CL (2021) An investigation into adult human height distributions using kernel density estimation. *Sankhya B: The Indian Journal of Statistics* (Feb): 1–27.

Katkovnik V, Shmulevich I (2002) Kernel density estimation with adaptive varying window size. *Pattern Recognition Letters* 23(14): 1641–1076.

Little RJA, Rubin DB (2002) *Statistical analysis with missing data*. 2nd Edition. New Jersey, USA: Wiley and Sons Publisher.

National Bureau of Statistics (2009) *Annual abstract of statistics*. Abuja: Federal Republic of Nigeria.

Ogbeide EM (2018) A new iterative imputation method based on adaptive expectation maximization. *Science Tech Journal* 3(1): 133–142.

Ogbeide EM, Osemwenkhae EJ (2019) Some improvements in nonparametric multivariate kernel density estimation. *Athens Journal of Science*s 6(4): 287–308.

Ogbeide EM, Osemwenkhae EJ (2021) Density estimation using a modified multivariate cluster sampling approach. *Benin Journal of Statistics* 4: 8–17.

Ogbeide EM, Osemwenkhae JE, Oyegue FO (2016) On a modified multivariate cluster sampling kernel approach to multivariate density estimation. *Journal of Nigerian Association of Mathematical Physics* 34(Jan): 123–132.

Ogbeide EM, Osemwenkhae JE, Oyegue FO (2017) A modified intersection of confidence intervals (MICI) approach in the multivariate data density estimation. *Journal of Nigeria Statistical Association* 29(Sep): 47–57.

Osemwenkhae JE, Ogbeide EM (2010): Adaptive Kernel density estimation: a review. *Nigerian Annals of Natural Sciences* 10(1): 88–96.

Salgado-Ugarte IH, Perez-Hernandez MA (2003) Exploring the use of variable bandwidth kernel density estimators. *The Stata Journal* 3(2): 133–147.

Scott DW (1992) *Multivariate density estimation*. New York: John Wiley.

Silverman BW (1986) *Density estimation for statistics and data analysis*. London: Chapman and Hall.

Tang K, Wan X, Liao Q (2020) Deep density estimation via invertible block-triangular mapping. *Theoretical and Applied Mechanics Letters* 10(3): 143–148.

Wand MP, Jones MC (1995) *Kernel smoothing*. London: Chapman and Hall/CRC.

Wu TJ, Tsai MH (2004) Root *n* bandwidths selectors in multivariate kernel density estimation. *Probability Theory and Related Fields* 129(Apr): 537–558.

Wu TJ, Chen CF, Chen HY (2007) A variable bandwidths selectors in multivariate kernel density estimation. *Statistics & Probability Letters* 77(4): 462–467.

Yang N, Huang Y, Hou D, Liu S, Ye D, Dong B, et al. (2019) Adaptive nonparametric kernel density estimation approach for joint probability density function modelling of multiple wind farms. *Energies* 12(7): 1346.

Zhang ZG, Chan SC (2011) On kernel selection of multivariate local polynomial modelling and its application to image smoothing and Reconstruction. *Journal of Signal Process System* 64(3): 361–374.